# Optothermal Manipulation of Phospholipid Membranes with Gold Nanoparticles
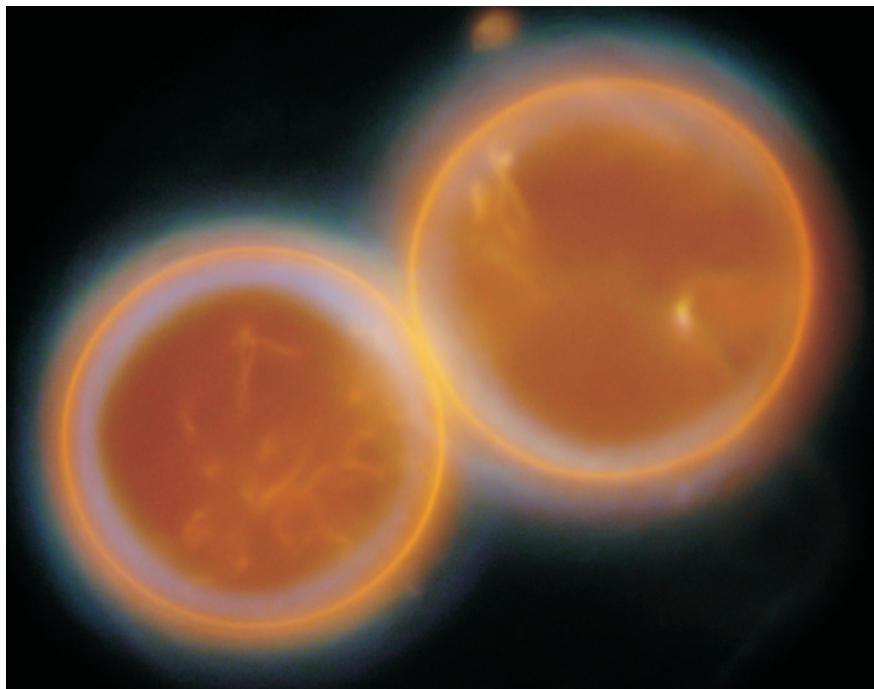
Dissertation
submitted to the Physics Department
of the Ludwig-Maximilians-Universität München

by

Alexander Skyrme Urban

of

Cambridge, United Kingdom

München, October 4th, 2010

First reviewer: Prof. Dr. Jochen Feldmann
Second reviewer: Prof. Dr. Don C. Lamb
Additional members of the examination: Prof. Dr. Joachim O. Rädler (chairman)
Prof. Dr. Ulrich Gerland

Date of the oral examination: November 12th, 2010

Scientific publications of results presented in this work

- T.K. Sau, A.S. Urban, S.K. Dondapati, M. Fedoruk, M.R. Horton, A.L. Rogach, F.D. Stefani, J.O. Rädler and J. Feldmann
  Controlling loading and optical properties of gold nanoparticles on liposome membranes
  Colloids and Surface A 342, 92-96 (2009)

- A.S. Urban, M. Fedoruk, M.R. Horton, J.O. Rädler, F.D. Stefani and J. Feldmann
  Controlled nanometric phase transitions of phospholipid membranes by plasmonic heating of single gold nanoparticles
  Nano Letters 9 (8), 2903-2908 (2009)

- A.S. Urban, A.A. Lutich, F.D. Stefani and J. Feldmann
  Laser printing single gold nanoparticles
  Nano Letters 10 (12), 4794–4798 (2010)

- A.S. Urban, T. Pfeiffer, A.A. Lutich, and J. Feldmann
  Single step photoporation of phospholipid membranes with gold nanoparticles
  in preparation (2010)

Additional publications

- R. Hauschild, H. Lange, A. Urban, H. Kalt and C. Klingshirn
  The influence of waveguide modes on stimulated emission from ZnO nanorods
  physica status solidi c 3 (10), 3557-3560 (2006)

- J. Fallert, R. Hauschild, A. Urban, H. Priller, H. Kalt and C. Klingshirn
  Processes of Stimulated Emission in ZnO
  AIP Conference Proceedings 893, 163-164 (2007)

- J. Fallert, R. Hauschild, F. Stelzl, A. Urban, M. Wissinger, H.J. Zho, C. Klingshirn and H. Kalt
  Surface-state related luminescence in ZnO nanocrystals
  Journal of Applied Physics 101 (7), 073506 (2007)

- H.J. Ba, J. Rodriguez-Fernandez, F.D. Stefani and J. Feldmann
  Immobilization of gold nanoparticles on living cell membranes upon controlled lipid binding
  Nano Letters 10 (8), 3006-3012 (2010)

- S.K. Dondapati, A.S. Urban, M. Fedoruk, A. Schwemmer, J. Feldmann and T.A. Klar
  Nanoscopic Potassium Sensor Based on Single Plasmonic Nanoparticles Covered by Lipid Membranes
  in preparation (2010)

Contributions to conferences and workshops

- A.S. Urban
  Physical Aspects of Drug-Delivery
  Workshop "Nano for Lifescience", Riezlern, Austria, June 2007

- A.S. Urban, M. Horton, S. Dondapati, T.K. Sau, T.A. Klar, J. Rädler and J. Feldmann
  Local Heating of Phospholipid Bilayers with Gold Nanoparticles
  The 52nd Annual Meeting of the Biophysical Society, Long Beach, California, February 2008

- A.S. Urban, M. Horton, S. Dondapati, T.K. Sau, T.A. Klar, J. Rädler and J. Feldmann
  Local Heating of Phospholipid Bilayers with Gold Nanoparticles
  DPG Frühjahrstagung des Arbeitskreises Festkörperphysik, Berlin, March 2008

- A.S. Urban, M. Fedoruk, F.D. Stefani and J. Feldmann
  Nanometric Local Heating of Phospholipid Membranes Functionalized with Gold Nanoparticles
  The 53rd Annual Meeting of the Biophysical Society, Boston, Massachusetts, March 2009

- A.S. Urban, M. Fedoruk, S. Wimmer, F.D. Stefani and J. Feldmann
  Nanometric phase transitions on phospholipid membranes using plasmonic heating of single gold nanoparticles
  SPIE Optics + Photonics - NanoScience and Engineering, San Diego, California, August 2009

- A.S. Urban
  Plasmonic Heating of Gold Nanoparticles in Biological Systems
  Workshop "New Concepts in Nanophotonics", Garmisch-Partenkirchen, November 2009

- A.S. Urban, M. Fedoruk, F.D. Stefani and J. Feldmann
  Nanometric phase transitions on phospholipid membranes using plasmonic heating of single gold nanoparticles
  The 54th Annual Meeting of the Biophysical Society, San Francisco, California, February 2010

Table of Contents

Kurzfassung

Die Plasmonresonanz von Goldnanopartikeln verleiht ihnen eine Reihe bedeutender Eigenschaften. So sind sie einerseits, bedingt durch den hohen Absorptionsquerschnitt, effiziente optothermische Energiewandler und andererseits trotz ihrer geringen Größe über den hohen Streuquerschnitt gut in Dunkelfeldmikroskopen zu erkennen. Diese Eigenschaften werden in dieser Arbeit zum einen ausgenutzt, um die Goldnanopartikel als optothermische Nanowerkzeuge für die Untersuchung und Manipulation von Phospholipidmembranen zu verwenden. Zum anderen werden Goldpartikel mittels der optischen Kräfte, die ein Laser auf sie ausübt, mit nanometrischer Präzision auf Substrate gedruckt.

Phospholipide sind der größte Bestandteil von biologischen Zellmembranen, welche die Zellen von ihrer Umgebung abgrenzen und in denen viele wichtige Prozesse stattfinden. Vesikel, bestehend aus einer Phospholipidmembran, dienten in den letzten Jahrzehnten vermehrt als Zellmodelle. Um an Vesikeln Untersuchungen durchführen zu können, mussten die Goldnanopartikel erst an die Membranen gebunden werden. Durch einen Ligandentausch mit Lipidmolekülen auf der Goldoberfläche konnten wir eine stabile Bindung zu den Vesikeln durch einfaches Mischen einer Vesikel- mit einer Goldlösung erzeugen. Als weitere Möglichkeit für eine Bindung ließen wir Goldnanopartikel direkt auf der Vesikelmembran wachsen. Durch Variieren der Goldionenkonzentration und durch Einbringen von geladenen Lipiden konnten Partikelgröße, -form und -dichte gezielt beeinflusst werden. Aus den optischen Eigenschaften dieser Goldvesikel konnten wir ein Modell für das Wachstum erstellen. Die mit dieser Methode hergestellten Vesikel eignen sich nicht nur als Untersuchungsobjekte für Membranstudien, sondern sie bieten sich auch für den Transport von Medikamenten in das Zellinnere an.

In weiteren Experimenten wurden Goldnanopartikel an Phospholipidvesikel gebunden und mit einer zur Absorption resonanten Wellenlänge optothermisch geheizt. Bei Leistungsdichten oberhalb von $300\,\mathrm{kW/cm^2}$ wurden Vesikel gezielt durch das Aufheizen der Goldnanopartikel zerstört. Bei niedrigeren Leistungsdichten war es mit einzelnen, an Vesikel in der Gelphase gebundenen Goldnanopartikeln möglich, einen reversiblen Phasenübergang der Vesikelmembran in die flüssige Phase zu induzieren. Dieser konnte durch eine erhöhte Diffusion der Goldnanopartikel in der Membran nachgewiesen und charakterisiert werden. Die Diffusion konnte außerdem zur Untersuchung von Membrandynamiken im Nanometerbereich genutzt werden. Dies wurde am Beispiel einer Messung der Ausbreitungsgeschwindigkeit der flüssigen Phase durch die Gelphase gezeigt. Mit solch kontrollierten Phasenübergängen und geeigneten Veränderungen der Eigenschaften des Laserstrahls konnten die Goldnanopartikel mit einer im Nanometerbereich liegenden Präzision an vorbestimmte Orte auf der Vesikelmembran geführt werden. Im Weiteren wurde eine Möglichkeit zur optischen Injektion von Goldnanopartikeln in Phospholipidvesikel untersucht, welche einen weiteren möglichen Ansatz zum gezielten Medikamententransport darstellt.

Darüber hinaus wurde eine neuartige Methode entwickelt, um einzelne Goldnanopartikel mit einer Präzision von einigen Nanometern auf einer Substratoberfläche zu platzieren. Diese Methode bedient sich der durch einen Laser ausgeübten optischen Kräfte um die Nanopartikel aus der Lösung einzufangen, sie zur gewünschten Position zu führen und die elektrostatische Abstoßung zu überwinden, sodass die Goldnanopartikel durch Van-der-Waals Kräfte fest mit der Substratoberfläche verbunden werden. Die Wal einer optimalen Leistungsdichte und die Wellenlänge des Lasers ergibt sich aus einem Kompromiss zwischen Druckpräzision und Druckgeschwindigkeit. Diese Methode ist sehr präzise, schnell und vielseitig und dürfte bei der Herstellung von Nanostrukturen auf Oberflächen in Zukunft eine größere Rolle spielen.

1 Introduction

Gold nanoparticles have been used by man for over 2000 years. The first known usage stems from ancient Indian medicine, where gold nanoparticles, around $60\,\mathrm{nm}$ in diameter were a part of a medicinal substance used to treat various diseases[1]. The Romans used gold nanoparticles hundreds of years later to create ornamental stained polychromatic glass[2]. It took however over 1500 years to realize gold nanoparticles were the actual source of these desired effects, when Michael Faraday observed that colloidal gold solutions have properties differing from bulk gold[3].

The interest in gold nanoparticles arises from their unique physical properties, which enable their use for many diverse applications. Of fundamental importance is the production of gold nanoparticles with finely controlled sizes and shapes. Much research has gone into this area in the last 40 years, resulting in reliable, high-yielding techniques for the synthesis of diverse gold nanoparticles. Examples include nanospheres, ranging between $5\,\mathrm{nm}$ and $250\,\mathrm{nm}$ in size[4,5], nanorods with well defined aspect ratios[6], nanoshells[7] and nanostars[8]. This achievement is extremely important, as many optical and electronic properties are size- and shape-dependent[9]. One of the most important characteristics of noble metallic nanoparticles is their *plasmon resonance frequency*, which typically lies in the visible range. The underlying collective oscillation of electrons, the cause of many of the initially observed effects, manifests itself in absorption and scattering cross sections that can exceed the geometrical cross section of the nanoparticles manifold. The enhanced scattering cross section has been exploited, e.g. for enhancing light-trapping in solar cells[10,11] as well as for single molecule tracking of biological components in cellular membranes[12,13]. The plasmon resonance depends on the dielectric properties of the surrounding medium and this fact has been used to create highly sensitive detectors for organic and biomolecules[14,15]. Optically excited gold nanoparticles

are surrounded by strong electric fields, enabling them to be used for Raman spectroscopy measurements on single molecules[16], for enhancing fluorescence of molecules[17] and, when arranged in the correct geometry, even for shaping a molecule's emission spectrum[18]. The absorption cross section has also been found to play an important role in a number of quite diverse uses. Because gold nanoparticles show negligible fluorescence[19] almost all of the absorbed light is converted into heat. This process is very fast, occurring on the scale of nanoseconds and results in high temperature increases[20,21]. These have been used in cancer therapy treatment, where absorbing gold nanoparticles photothermally destroy cancer cells through generating high temperatures or initiating microbubble formation[22–24]. More moderate temperature increases have been used for microsecond DNA-analysis[25] and for enhancing gene delivery efficacy[26]. Gold nanoparticles have the additional and highly attractive feature of surfaces than can easily be modified. This enables them to be coated with appropriate molecules to enhance binding to various structures[27] or to bring specific functional groups onto the surfaces of nanoparticles[28].

One area of research that has evolved only recently is the assembly of plasmonic nanostructures out of single nanoparticles[29]. While conventional lithographical techniques are slowly reaching the limit of what feature dimensions they can produce, the need has arisen to manufacture devices with smaller feature dimensions of only a few tens of nanometers. Techniques have been newly developed for single nanoparticle patterning, which, however, often involve multiple steps of chemical patterning of substrates and rarely result in a precision comparable to the size of single nanoparticles.

Gold nanoparticles have been used to study many properties of cellular membranes in recent years, e.g. lipid diffusion and raft formation[30]. Often, however, the complexity of cells makes an effective analysis of certain parameters difficult, if not impossible. For this reason *giant unilamellar vesicles* (*GUVs*) have been often used. These have dimensions comparable to cells and their membrane composition can be easily controlled and modified depending on the desired study[31,32]. Current techniques are able to produce these artificial cells in large quantities, consisting

predominantly of *phospholipids*, with highly controlled sizes and membrane contents[33]. Many properties of phospholipid membranes are temperature dependent, e.g. bending rigidity, lipid diffusion and phase organization. Up-to-date research has characterized these properties by macroscopically heating solutions containing GUVs and measuring the reaction of ensembles down to single GUVs. However, heating of smaller, nanosized membrane regions has so far not been accomplished, although this would be required for studying and manipulating thermally activated molecular processes, involving, for example temperature reactive proteins[34] or lateral sorting and signaling[35].

In this thesis I will present research I have conducted on gold nanoparticles, exploiting their optical properties, the optical forces acting on them and the thermal energy produced by them upon laser illumination. There were two aims in doing these experiments. The main aim was to use gold nanoparticles for the investigation and manipulation of phospholipid membranes and processes occurring therein. During this work, we characterized the optical forces exerted by a laser beam on a gold nanoparticle and developed the second aim of exploiting this effect in order to create patterned nanostructures made of single gold nanoparticles.

In Chapter 2 the theoretical concepts necessary for understanding the experiments and their results are presented. The chapter begins with a description of the most fundamental component of the experiments, gold nanoparticles. Their optical and thermal properties are discussed and optical excitation is described in detail. Following this part is a brief discussion of optical forces exerted by a laser beam on particles residing inside the beam. The following section illustrates the Derjaguin-Landau-Verwey-Overbeek theory, a basic theory for understanding the stability of colloidal solutions. These two sections are essential for understanding the experiments on patterned nanostructures (Chapter 4). The last part of the chapter deals with biological membranes, their main components and characteristics; this is the basis for understanding the experiments dealing with phospholipid membranes (Chapter 5).

Chapter 3 is structured in two parts, beginning with an overview of the setups used in the experiments and their modes of operation, the most important setup being the dark field microscope. The second part deals with the preparation of samples for the experiments. Here, I describe the chamber we designed for the growth of giant unilamellar vesicles and the modifications of the growth procedures we developed. Furthermore, we were the first to develop a surface modification of gold nanoparticles designed to enable their binding to phospholipid membranes.

In Chapter 4 I first describe the initial experiments observing the printing phenomenon and establish a model explaining the processes. This part was actually conducted after the set of experiments described in Chapter 5, in which the optical forces exerted on a gold nanoparticle by a laser were encountered. These observations led to the idea of trying to establish a new way to pattern substrates with single nanoparticles. These studies are presented first, because they involve a detailed study of the optical forces in a Gaussian laser beam, which also play a major role in the experiments conducted on gold nanoparticles on phospholipid membranes in Chapter 5. Thus in Chapter 4 I first investigate the precision of the printing method and factors determining it. Then I discuss in detail the versatility of the method and describe other, more complex patterning processes, which this method enables. Some of these ideas have already been investigated experimentally, while others are still in the design stage.

The second experimental chapter (Chapter 5) then focuses on gold nanoparticles on phospholipid membranes. The idea is to use the gold nanoparticles not only as tools for detection and sensing, but to exploit their optothermal properties to enable manipulation of the membrane and of processes occurring therein. The first part of this chapter deals with the binding processes of gold nanoparticles to phospholipid membranes. As part of these studies, a new method of growing gold nanoparticles directly onto giant unilamellar vesicles was developed. After that I describe how optically heated gold nanoparticles can induce reversible gel-fluid phase transitions in membranes. This method can also be used to investigate membrane dynamics and to direct the gold nanoparticles to specific locations on the membrane. Having demonstrated this we investigate the optical injection of gold nanoparticles into the vesicles, a principle study relevant for targeted drug-delivery.

2 Fundamentals

In this chapter the fundamental theoretical background necessary to understand this thesis is presented. First the optical and thermal properties of gold nanoparticles are discussed. The interaction between these nanoparticles and light is described on the basis of the dielectric function, $\varepsilon(\omega)$. Here it is shown how the metallic nanoparticles' properties can be exploited to make particles visible down to a size of 20 nm and how they can be used to efficiently convert light into heat. This section is followed by two short sections on the optical forces acting on particles exposed to light and on a theory of colloidal dispersions. These two sections are vital for the chapter on laser printing of metallic nanoparticles (chapter 4). The last section describes the structure and main characteristics of biological membranes in detail, focusing on phospholipids as the prime component. An important structure into which phospholipids can assemble are vesicles. These mainly spherical structures have been recognized not only as objects for study, but also as ideal systems for transport and drug-delivery[32,36]. Because they do not contain many components commonly found in cellular membranes, studies of certain membrane characteristics and processes are much simpler and more efficient when conducted on phospholipid vesicles instead of entire cells. Vesicles and many of their characteristics are explained in detail in this chapter. These structures are the basis for the work on the interaction of gold nanoparticles and phospholipid membranes (chapter 5).

2.1 Optical and Thermal Properties of Gold Nanoparticles

The Romans were known for their many inventions and were in fact among the first to use metallic nanoparticles, although unknowingly[37]. The *Lycurgus Cup*, depicting the Greek king Lycurgus being dragged to the underworld, is one of the first examples of how gold nanoparticles, typically $5-60$ nm in size, can be used to colour glass in an extraordinary way (Figure 2.1). In ordinary daylight the cup has a predominantly green color; however it appears red when illuminated from the inside. This amazing effect results from the characteristic properties of metallic nanoparticles and the way they interact with light.
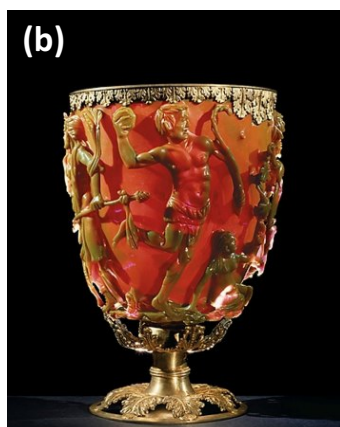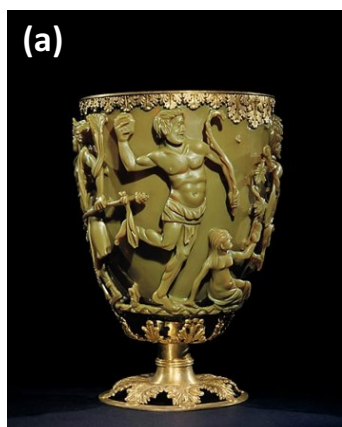
Figure 2.1 | The Lycurgus Cup is an excellent example of the optical properties of gold. (a) When illuminated from the outside, the gold nanoparticles inside the glass cup scatter the light, making the cup appear green. (b) However, when a light is placed inside the cup, the absorption of the gold nanoparticles changes the cup's apparent color to red.

2.1.1 Optical Properties

The noble metals copper (Cu), silver (Ag) and gold (Au) are all elements belonging to the 11th group of the periodic table. The electron configurations of these elements are exceptions to the *Madelung rule*, which describes the filling order of the atomic subshells. All of these elements have completely filled d-subshells (respectively 3d, 4d and 5d); their core electrons are in the so called inert gas configuration. Their metallic properties result from the lone valence electron in the half-filled s-subshells (4s, 5s and 6s respectively). The band structure of gold displays five comparatively flat d-bands, lying $1-3$ eV below the *Fermi energy*, E_F, in which the ten d-electrons are located (Figure 2.2). The lone s-electron forms an sp-hybridised band, which is

filled up to E_F. Electrons in this band can move quasi-free due to the near parabolic form of the band. This band structure defines the characteristic properties of these metals, such as their thermal and electrical conductivity.
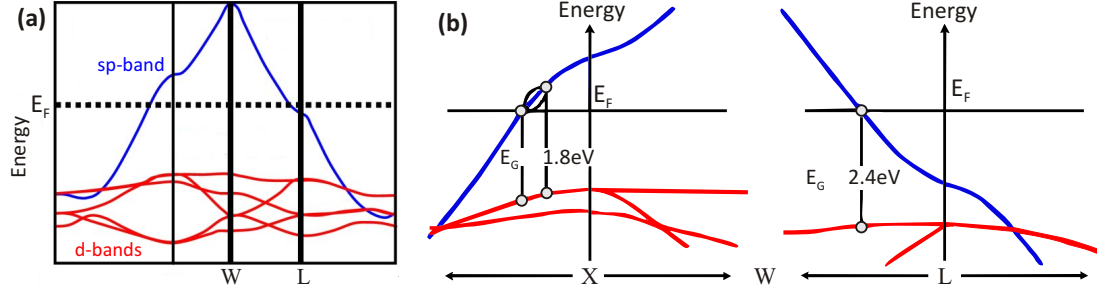
Figure 2.2 | The band structure of gold. (a) The sp-band has a nearly parabolic form leading to quasi-free electrons. (b) Interband transitions in gold occur near the X- and L- points in the first Brillouin zone. (Taken from [38,39])

2.1.1.1 Dielectric Properties of Gold

The electrons in this band can be seen as free electrons because of the near-parabolic sp-band of gold. An accurate description is given by the *Drude-Sommerfield theory*[40]. This model depicts the electrons as a gas of independent,quasi-free point-shaped particles that are accelerated by an external electric field and slowed down after a mean free time, $\tau = \Gamma^{-1}$, through collisions with metal ions (for gold[41]: $\tau = 30\,\text{fs}$ at $273\,\text{K}$). Scattering processes are the reason that the electrons are called *quasi-free* and not *free*. The Drude-Sommerfield model determines the response function or *dielectric function*, $\varepsilon(\omega)$, of a macroscopic metal by calculating the behavior of a single conduction electron and multiplying this behavior by the number of electrons present. This is only valid when assuming the independence of the single electrons, as stated above. The equation of motion for an electron of mass, m_e, and charge, e, in an external electric field $\vec{E} = \vec{E}_0 e^{-i\omega t}$ is given by:

$$m_e \frac{\partial^2 \vec{r}}{\partial t^2} + m_e \Gamma \frac{\partial \vec{r}}{\partial t} = e\vec{E}_0 e^{-i\omega t} \tag{2.1}$$

with the damping constant, Γ. This differential equation is valid for a model system without eigenfrequencies for $\omega > 0$ and only takes into account the effect on

the conduction band electrons. In order to incorporate bound electrons, a linear restoring force, determining the eigenfrequency of the oscillating electrons, would have to be added to the equation. Solving equation 2.1 leads to the dipole moment of a single electron, $\vec{p} = e\vec{r}_0$, and the polarization, $\vec{P} = n\vec{p}$, with the number of electrons per unit volume, n . The dielectric function, $\varepsilon(\omega) = \varepsilon_1(\omega) + i\varepsilon_2(\omega)$, is related to the polarization via the definition $\varepsilon = 1 + P/(\varepsilon_0 E)$ and to the complex refractive index via $n + ik = \sqrt{\varepsilon}$. This leads to the dielectric function of a system of n free electrons per unit volume:

$$\varepsilon(\omega) = 1 - \frac{\omega_p^2}{\omega^2 + i\Gamma\omega} = 1 - \frac{\omega_p^2}{\omega^2 + \Gamma^2} + i\frac{\omega_p^2 \Gamma}{\omega(\omega^2 + \Gamma^2)} \tag{2.2}$$

which is only determined by the *plasma frequency*, $\omega_p = \sqrt{ne^2/\varepsilon_0 m^*}$, and the relaxation constant, Γ. This can be determined from the electron mean free path, l by $\Gamma = v_F/l$, where v_F is the *Fermi velocity*. If the damping is much smaller than the frequency, the real and imaginary parts of the dielectric function can be written as:

$$\varepsilon_1(\omega) \approx 1 - \frac{\omega_p^2}{\omega^2}, \quad \varepsilon_2(\omega) \approx 1 - \frac{\omega_p^2}{\omega^3}\Gamma. \tag{2.3}$$

This equation shows that for $\varepsilon_1(\omega) = 0$ the frequency, ω, equals the plasma frequency, ω_p. The dielectric function, $\varepsilon(\omega)$, is commonly expressed in terms of the electric susceptibility, χ. Then equation 2.2 becomes:

$$\varepsilon(\omega) = 1 + \chi_{\text{DS}}(\omega) \tag{2.4}$$

where χ_{DS} is the free-electron Drude-Sommerfield susceptibility. Electrons in a real metallic lattice are only quasi-free due to the lattice periodicity. The coupling of the free electrons to the ion core is taken into consideration by replacing the electron mass, m_e, with an effective electron mass, m^*, effectively altering ω_p.

Not only the conduction band electrons but also electrons from deeper levels contribute to the dielectric function. Direct excitations of electrons from the 5d-band to vacant states above E_F in the 6sp-band can take place near the X- and L- points

in the first Brillouin zone (Figure 2.2a). These optical excitations exist both in gold nanoparticles as well as in bulk gold and begin at the inter-band gap $E = 1.7\,\text{eV}$[39,42] (Figure 2.2b). However, the oscillator strength of this transition near the X-point is so low that in measurements of the optical density of gold colloidal solutions this transition can not be seen. Instead, the transition near the L-Point with $E = 2.38\,\text{eV}$ becomes visible as a constantly increasing background, independent of nanoparticle size (Figure 2.3). This effect leads to an additional term in the susceptibility and equation 2.2 becomes:
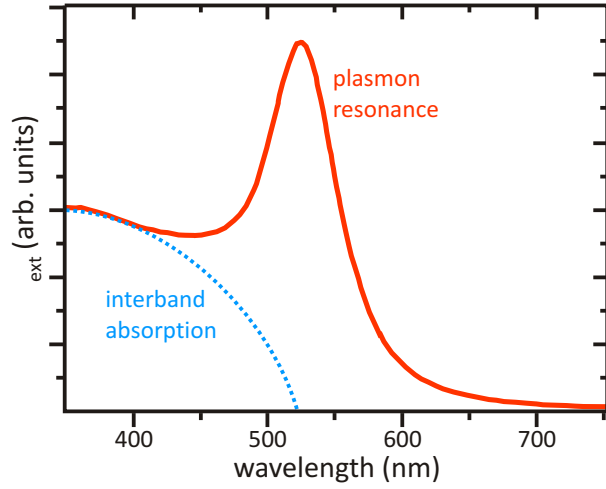
Figure 2.3 | Extinction spectrum of a colloidal suspension of $40\,\text{nm}$ **gold nanoparticles.** The plasmon resonance is centered at $528\,\text{nm}$. The contribution of intraband excitations is clearly seen for wavelengths below $520\,\text{nm}$.

$$\varepsilon(\omega) = 1 + \chi_{\text{DS}} + \chi_{\text{IB}} \qquad (2.5)$$

with the interband susceptibility, $\chi_{\text{IB}} = \chi_{\text{IB, 1}} + i\chi_{\text{IB, 2}}$. The imaginary part describes the direct energy dissipation and is thus only large for frequencies at which interband transitions occur. The real part however is also important for smaller frequencies[40].

The dielectric functions of nanoparticles with a diameter that is larger than approximately $10\,\text{nm}$ are size-independent and become like those of bulk-gold. Smaller nanoparticles are considerably smaller than the electron mean free path, $l = v_F \tau = 42\,\text{nm}$. In these, the electrons cannot cover this distance without scattering at the nanoparticle surface. This reduced mean free path has been confirmed experimentally[43,44] and causes the homogeneous linewidth of the plasmon resonance to greatly increase for these nanoparticles. As stated before, bound electrons (e.g. the d-band electrons) have not been accounted for yet as the Drude-

Sommerfield model only considers free-electrons[45]. Modeling these electrons is extremely difficult[46]. Normally, instead of using corrected values for the dielectric function, experimental ones are used. The main source for these values comes from the work of Johnson and Christie, who measured the optical properties of bulk gold in 1972[47]. In all calculations conducted within this thesis these values were used. This is valid, because all of the nanoparticles used were larger than $10\,\text{nm}$.

Due to the energy dissipation of electromagnetic waves impinging on a metal surface, these only have a limited penetration depth which can be calculated from the optical functions. Assuming a plane wave incident in the z-direction and expressing the wave vector, $\vec{k}$, as $\left|\vec{k}\right| = (\omega/c)(n + ik)$, the electric field within the metal can be expressed as:

$$\vec{E}(\vec{r}, t) = \vec{E}_0(\vec{r}, t)e^{i\omega(zn/c - t)}e^{-z/d} \tag{2.6}$$

with the attenuation of the field determined by the *skin depth*, $d = \frac{c}{\omega k} = \frac{\lambda}{2\pi k}$, and the optical function, $n + ik = \sqrt{\varepsilon_1 + i\varepsilon_2}$. The skin depth is wavelength dependent and assumes values for gold between $31\,\text{nm}$ at $620\,\text{nm}$ incident wavelength and $37\,\text{nm}$ at $413\,\text{nm}$.

2.1.1.2 Electrodynamic Calculations of Spherical Particles (Mie Theory)

In order to calculate the response of a metal nanoparticle to an external electromagnetic field, one must solve Maxwell's equations. Fortunately, an analytical solution already exists. Danish physicist Ludvik Lorenz first published this in 1890, however only in Danish. Later, Gustav Mie "rediscovered" it in 1908, wherefore it is generally known as *Mie-Theory*. The theory is valid for all nanoparticle sizes and optical wavelengths in contrast to Rayleigh's scattering theory, which is limited to nanoparticles much smaller than the wavelength of the incident radiation. In fact, Rayleigh scattering is a first-order approximation of Mie-Theory.

In his solution of the Maxwell equations, Mie describes the interaction between a plane wave and uncharged homogeneous particles. This allows the precise calculation of the electromagnetic fields within and surrounding the particle. The

spherically symmetrical geometry suggests a multipole expansion of the fields. The resulting surface harmonics enable the calculation of the extinction, scattering and absorption cross-sections of the particles:

$$\sigma_{ext} = \frac{2\pi}{|k|^2} \sum_{n=1}^{\infty} (2n+1)\text{Re}[a_n + b_n] \tag{2.7}$$

$$\sigma_{sca} = \frac{2\pi}{|k|^2} \sum_{n=1}^{\infty} (2n+1)[|a_n|^2 + |b_n|^2] \tag{2.8}$$

$$\sigma_{abs} = \sigma_{ext} - \sigma_{sca} \tag{2.9}$$

with the Mie-coefficients from the multipole expansion, a_n and b_n, the multipole order, n, ($n = 1$ corresponds to the dipole mode) and the wave vector of the incident electromagnetic wave, $\vec{k}$. "Re" signifies that only the real part of the bracket is taken. The Mie-coefficients are:

$$a_n = \frac{m\,\psi_n\,(mx)\,\psi_n^{'}(x) - \psi_n(x)\psi_n^{'}(mx)}{m\,\psi_n(mx)\eta_n^{'}(x) - \eta_n(x)\psi_n^{'}(mx)} \tag{2.10}$$

$$b_n = \frac{\psi_n(mx)\psi_n^{'}(x) - m\,\psi_n(x)\psi_n^{'}(mx)}{\psi_n(mx)\eta_n^{'}(x) - m\,\eta_n(x)\psi_n^{'}(mx)} \tag{2.11}$$

with the Riccarti-Bessel functions, ψ_n and η_n , the ratio of the complex refractive indices of the particle and the surrounding medium, $m = n_{part}/n_{medium} = \sqrt{\epsilon_r}$, and the ratio of the particle radius, r, to the wavelength of the scattered light, λ, being $x = 2\pi r/\lambda$. In this work, calculations of the cross sections of gold nanoparticles were carried out with the program MQMie[48]. With this program it is also possible to account for core-shell particles or uncharged surface ligand molecules.

2.1.1.3 Electrostatic and Quasi-Static Modeling

Mie theory is excellent for calculating scattering and absorption by spheres because it is an exact theory. However, calculating the exact results for geometries more complex than spheres can be extremely time consuming and is not always necessary. Furthermore, Mie theory is not always the best choice when one wants to acquire some intuitive feeling for how a sphere of a given size and optical properties absorbs

and scatters light. This is facilitated by applying electrostatics. Here the electric-magnetic field imposing on the metal nanoparticles is both spatially and temporally constant. Considering the boundary-conditions that the tangential components of the electric and magnetic fields must be continuous at the particle surface[49], one obtains the electric field inside the nanoparticle:

$$E_i = E_0 \frac{3\varepsilon_m}{\varepsilon + 2\varepsilon_m} \tag{2.12}$$

with the dielectric constant of the surrounding medium, ε_m. The internal field directly supplies the static polarizability of the sphere, $\alpha = p/\varepsilon_m E_0$:

$$\alpha = 4\pi\varepsilon_0 R^3 \frac{\varepsilon - \varepsilon_m}{\varepsilon + 2\varepsilon_m} \tag{2.13}$$

This electrostatic approach can be extended even further to the *quasi-static regime* in which the electromagnetic field is still spatially constant but now has a time dependence ($\vec{E} \rightarrow \vec{E}(t)$). To account for this, ε and ε_m in equations 2.12 and 2.13 must be replaced by their frequency dependent functions, $\varepsilon(\omega)$ and $\varepsilon_m(\omega)$; excitations induced by the magnetic field are neglected. Resonances then occur for both the internal electric field and the polarizability, when the denominator becomes minimal:

$$[\varepsilon_1(\omega) + 2\varepsilon_m]^2 + [\varepsilon_2(\omega)]^2 \rightarrow minimal \tag{2.14}$$

Thus a negative ε_1 is necessary, or in the special case of a small $\varepsilon_2 << 1$, or a small frequency dependency $\partial\varepsilon_2/\partial\omega$, the resonance condition becomes:

$$\varepsilon_1 = -2\varepsilon_m \tag{2.15}$$

This then leads to the position of the resonance using the approximative equation 2.3 for free-electron metals and $\varepsilon_m = 1$:

$$\omega_1 = \frac{\omega_p}{\sqrt{3}} \tag{2.16}$$

What has been done here in basic terms is to use a simple oscillator model to calculate the *Drude eigenfrequency* for free electron nanoparticles. In this model

the free electrons from the sp-band are displaced by an incoming electric field, E_{in}, (Figure 2.4). The Coulomb interaction between the displaced electrons and the

positive charges left behind by the stationary atomic cores serves as a restoring force with the surface polarization supplying the majority of this force. The electrons oscillate collectively and the oscillation is allocated with a bosonic quasiparticle, the *surface plasmon*. Its frequency, ω_1, was derived in equation 2.16. This theory can easily be extended to metal spheroids or ellipsoids, in which case the eigenfrequency, ω_1, depends on the spatial orientation, resulting in a seperate eigenfrequency for each independent spatial direction.
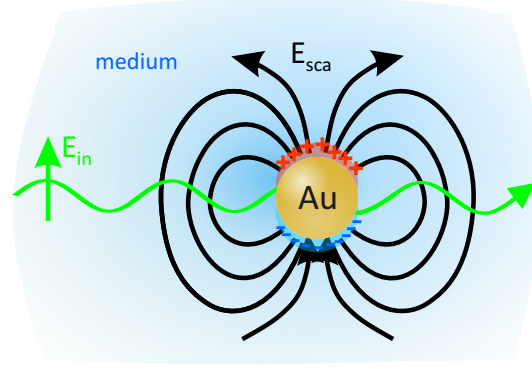
Figure 2.4 | Formation of a surface plasmon in a gold nanoparticle. An electromagnetic wave penetrates the nanoparticle completely and induces the conduction band electrons to oscillate. This induced Hertzdipole produces radiation.

The resonance wavelengths or frequencies of plasma resonances of metal nanoparticles can be easily analyzed in the quasi-static regime. As stated previously, this is only valid for very small nanoparticles ($2r \ll \lambda$). In this case, phase retardation and effects of higher multipoles are neglected and the Mie formula is drastically simplified. Using $k = \omega/c$ as the lowest order term, equation 2.7 becomes[40,50]:

$$\sigma_{ext}(\omega) = 9\frac{\omega}{c}\varepsilon_m^{3/2}V_{np}\frac{\varepsilon_2}{(\varepsilon_1(\omega) + 2\varepsilon_m)^2 + (\varepsilon_2(\omega))^2} \qquad (2.17)$$

with the nanoparticle volume, $V_{np} = 4/3\pi r^3$, the dielectric function of the medium ,ε_m, and the complex dielectric function of the nanoparticle, $\varepsilon_{np}(\omega) = \varepsilon_1(\omega) + i\varepsilon_2(\omega)$. This extinction cross section describes only dipolar absorption. The scattering cross section (equation 2.8), proportional to R^6 and higher multipolar contributions ($\sigma_{ext,quadrupol} \propto R^5$, $\sigma_{sca,quadrupol} \propto R^{10}$) are highly suppressed at $2r << \lambda$. The resonance condition $\varepsilon_1(\omega) = -2\varepsilon_m$ is well met by alkali metals, but not by free electron metals such as gold. Here, where $\omega >> \Gamma$, the shape and position of the

resonance can be estimated by inserting equation 2.3 into equation 2.17. This results in an extinction coefficient of:

$$\sigma_{ext}(\omega) = \sigma_0 \frac{1}{(\omega - \omega_1)^2 + (\Gamma/2)^2} \qquad (2.18)$$

The shape of the extinction is thus Lorentzian in the vicinity of the resonance, whose position can be calculated directly from the plasma frequency:

$$\omega_1 = \frac{\omega_p}{\sqrt{1 + 2\varepsilon_m}} \qquad (2.19)$$

2.1.1.4 Damping Mechanisms of the Surface Plasmon

The damping in the system is due to scattering of the electrons at other electrons, phonons, lattice defects, the particle surface, etc. such that the damping constant, Γ, results from the average of the collision frequencies of the electrons. For independent collision processes, i, the *Matheisen rule* applies and Γ is the result of the summation of all collisional frequencies:

$$\Gamma = \tau^{-1} = \sum_i \tau_i^{-1} = \tau_{e-e}^{-1} + \tau_{e-phonon}^{-1} + \tau_{impurities}^{-1} + ... \qquad (2.20)$$

Experimentally, Γ is determined by measuring the macroscopically available electrical conductivity, ρ_{el}, and inserting this into $\Gamma = \rho_{el} n e^2 / m^*$.

As stated before, the collective oscillation of the sp-electrons can be described as a bosonic quasiparticle, the plasmon. An excited plasmon can decay through a multitude of channels. These are divided into two main groups, radiative and non-radiative decay processes (Figure 2.5). The radiative decay occurs via emission of photons, which can be seen in the far-field as scattered light. This is described in the classical picture of a Hertz dipole via the periodical acceleration of electrons away from their equilibrium positions. This leads to the emission of energy via radiation by the nanoparticle. According to the Abraham-Lorentz equations of motion, which are extensions of the Drude-Sommerfield theory, the radiative decay

rate in a nanoparticle, R_{rad}, is size-dependent[51]:

$$R_{rad} \propto V \propto r^3 \tag{2.21}$$

Thus, the probability that the plasmon decays radiatively is directly proportional to the nanoparticle volume, i.e. to the cube of the nanoparticle radius. The plasmon resonance becomes very clear in the scattering spectrum of gold nanoparticles. Even $40\,\mathrm{nm}$ nanoparticles can be seen easily in a dark field microscope[52,53].
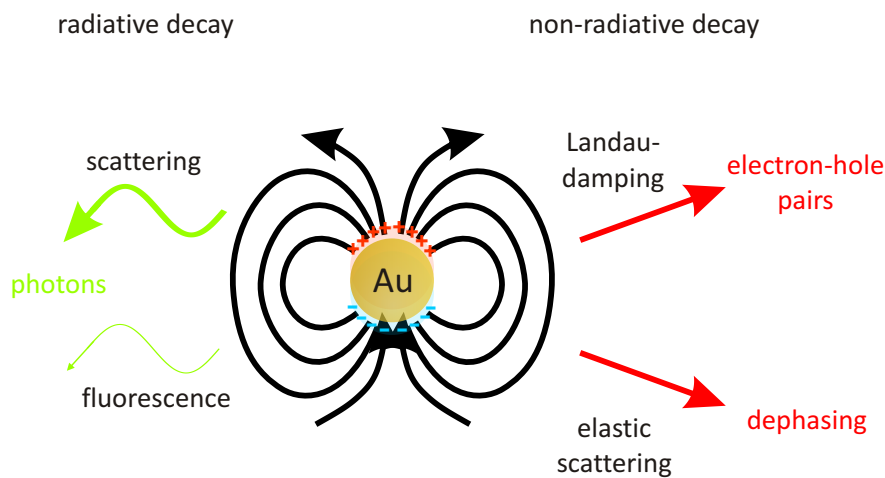
Figure 2.5 | Surface plasmons can decay either via radiative (left) or non-radiative processes (right). The fluorescence emission of gold is negligible, however[19].

The non-radiative decay of the surface plasmon leads to the nanoparticle absorbing the incident light, which is converted efficiently into heat. This process is essential for the work done here and will be described in more detail in section 2.1.2. The most important damping mechanism for the optothermal properties of gold nanoparticles is Landau damping. Here the plasmon decays non-radiatively by creating electron-hole pairs. One must distinguish between excitation of electron-hole pairs inside the sp-band (*intraband* excitation) and the excitation of electrons from the energetically deeper d-band into the sp-band (*interband* excitation). A further decay channel is the elastic scattering of the oscillating electrons. These can scatter from each other, from phonons, lattice defects, impurities or from the particle surface and thus come out of synchrony with each other. This leads to a dephasing of the electrons.

2.1.1.5 Factors Determining Position and Shape of the Plasmon Resonance

Figure 2.6 shows calculated extinction, scattering and absorption cross sections for an $80\,\text{nm}$ gold nanoparticle in water ($\varepsilon_m = 1.33^2 = 1.77$). For gold nanoparticles of this size, both scattering and absorption contribute considerably to the extinction cross section. Also, the spectral positions of the two resonance maxima are shifted slightly, with absorption having its maximum at $543\,\text{nm}$ and scattering at $559\,\text{nm}$.

The spectral position of the plasmon resonance is determined by several factors. An internal shielding of the Coulomb attraction between the atomic cores and the conduction band electrons by the polarized d-electrons in the valence band can occur, leading to a red-shift of the resonance[54]. Another important factor is the surrounding medium. The Coulomb-field of the plasmon dipole lies partially outside the nanoparticle in the surrounding medium. This can lead to a decrease in the field and a reduction of the restoring force, depending on the polarizability of the

Figure 2.6 | Mie Theory results. Calculated extinction (black), scattering (green) and absorption (red) cross sections for an $80\,\text{nm}$ gold nanoparticle in water

surrounding medium. The higher the refractive index of the surrounding medium and thus the dielectric constant, the stronger the external shielding and the resulting shift of the plasmon resonance to longer wavelengths[40]. The shift of the plasmon resonance is so dramatic that this is often used as a biomolecular nanosensor[14,55].

For larger nanoparticles another effect also shifts the plasmon resonance to longer wavelengths. If the field of the incoming electromagnetic wave varies, then the electrons cannot be deflected simultaneously. The phase shift of the driving wave inside the nanoparticle plays an increasing role because the field is no longer homogeneous throughout the nanoparticle. Thus the electrons on the front and back

of the nanoparticles oscillate with different phases. This *retardation effect* leads both to a red-shift as well as to a widening of the plasmon resonance, which both increase with increasing nanoparticle size. Consequently, the wavelength of the extinction maximum shifts from 521 nm for 20 nm gold nanoparticles to 571 nm for 100 nm gold nanoparticles (Figure 2.7a and Figure 2.7b).
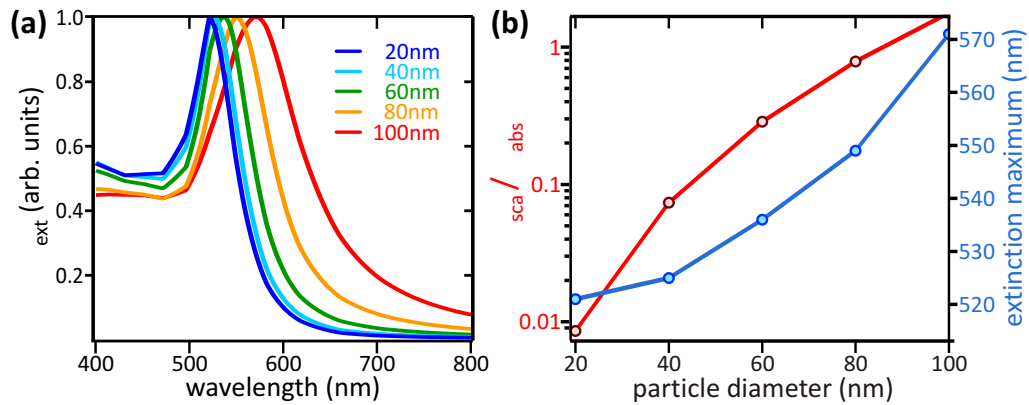
Figure 2.7 | Size dependence of the plasmon resonance. (a) Extinction cross sections for nanoparticles between 20 nm and 100 nm in diameter. The considerable red-shift is mainly due to the retardation effect. (b) Ratio of scattering and absorption cross sections for nanoparticles between 20 nm and 100 nm in diameter. Whereas for 20 nm nanoparticles absorption completely dominates, scattering becomes more important with larger nanoparticle size.

As stated in section 2.1.1.3, the dipolar absorption increases $\propto R^3$, whereas the dipolar scattering increases $\propto R^6$. Thus, for small nanoparticles the extinction cross section is dominated by absorption (Figure 2.7b). For nanoparticles of 20 nm diameter the absorption cross section is two orders of magnitude larger than the scattering cross section. This ratio changes considerably for larger nanoparticles, so that for gold nanoparticles with a diameter of 100 nm the scattering cross section is already twice as large as the absorption cross section. Smaller nanoparticles are more efficient at absorbing light and thus converting it into heat, as will be discussed in section 2.1.2. On the other hand, larger nanoparticles scatter light more efficiently and can thus be made visible more easily.

2.1.2 Thermal Properties

2.1.2.1 Optical Heating of Gold Nanoparticles

As described in the last section, gold nanoparticles are highly efficient in converting optical energy into thermal energy. This has two main reasons, both of which are due to intrinsic properties of gold nanoparticles. Firstly and most importantly, gold nanoparticles have a very strong coupling with visible light due to the plasmon resonance. The absorption cross section of a gold nanoparticle is much larger than the geometric cross section, especially for smaller nanoparticles. This means that even though the gold nanoparticle's geometric cross section is exposed to the light the nanoparticle collects light from a much larger area. The absorption efficiency, $\eta_{abs} = \sigma_{abs}/\sigma_{geo}$, is linearly proportional to the nanoparticle size for nanoparticles up to $60\,\mathrm{nm}$[56] and reaches a maximum at $70\,\mathrm{nm}$ (Figure 2.8). The second important reason is that light that has already been absorbed is not emitted as photoluminescence or only negligibly so[19].
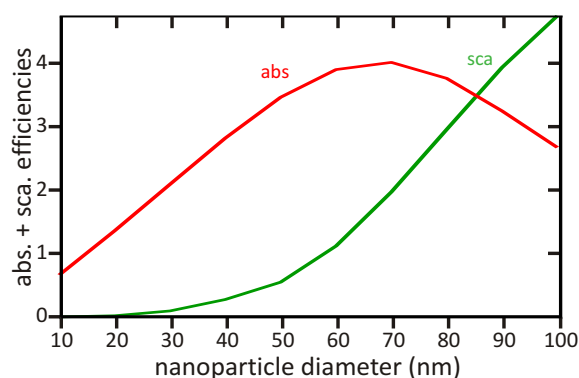
Figure 2.8 | Absorption η_{abs} and scattering η_{sca} efficiencies of gold nanoparticles depending on nanoparticle size. While nanoparticles $< 60\,\mathrm{nm}$ are highly efficient at absorbing light, larger nanoparticles scatter light much more efficiently. $70\,\mathrm{nm}$ particles are the most efficient optothermal energy converters.

To understand the internal processes that happen extremely fast after excitation of a gold nanoparticle, many experiments with fs-excitation have been carried out. These were conducted first on thin gold films[57,58], and later on gold nanoparticles[59–61].

Figure 2.9 shows a scheme of the internal processes occurring upon fs-laser illumination. An ultra-short laser pulse (shorter than the electron-phonon interaction time) induces the conduction band electrons to oscillate, creating surface plasmons. In under $20\,\mathrm{fs}$ the electrons dephase[62]. This is due to two processes: creation of

electron-hole pairs and by radiation damping, i.e. the decay of surface plasmons into photons. The later process is important for nanoparticles with a radius above $10\,\mathrm{nm}$. This process does not lead to a heating of the nanoparticle, since the entire energy is emitted as photons. The first process is mainly due to electron-electron scattering and for nanoparticles smaller than $10\,\mathrm{nm}$ in diameter also due to electron-surface scattering[52]. Part of the electrons are thus excited above the *Fermi-level*. These incoherently excited electrons are no longer in thermal equilibrium with the
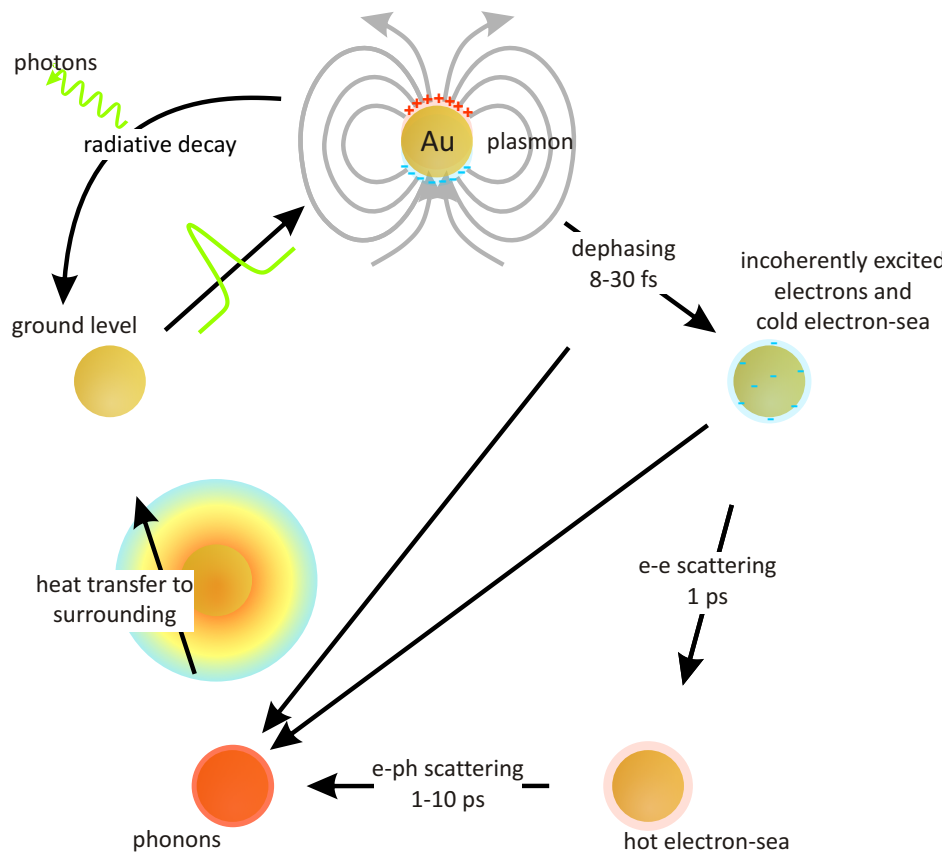
Figure 2.9 | Internal processes in gold nanoparticles upon fs-laser excitation. The particle itself heats up within $10\,\mathrm{ps}$, and after that transfers its thermal energy to its surroundings.

remaining cold electron sea. There is a clear deviation from the normal Fermi-distribution. The excited electrons thermalize through two processes, by scattering elastically among each other and at the same time by scattering with phonons. The first process happens on a time scale of under $1\,\mathrm{ps}$[63,64], while the second one occurs within $1-10\,\mathrm{ps}$. Electron-electron scattering produces a hot-electron sea

with the electrons reaching thermal equilibrium. The electron-sea, which can now be ascribed a temperature, can reach several thousands of degrees Celsius. Even though part of the energy from the excited electrons is transfered to the ionic core lattice through electron-photon scattering processes, the electron sea is still much hotter than the cold ionic core lattice. This is because a hot electron-sea interacts poorly with a cold ionic-lattice due to an average energy transfer of only $7\,\mathrm{meV}$ per electron-phonon scattering process[65]. The thermal disequilibrium is leveled out within the next $10\,\mathrm{ps}$[57,58,61] through further electron-photon interactions. The result is a homogeneously heated gold nanoparticle. Up until this time the interaction between the gold nanoparticle and its surrounding is negligible. After reaching thermal equilibrium with itself, however, the gold nanoparticle transfers the heat to its surrounding and, depending on gold nanoparticle size, in under $1\,\mathrm{ns}$ the gold nanoparticle returns once more to its ground state in thermal equilibrium with its environment[66]. These internal processes are the same for both gold nanoparticles and also bulk gold. Temperatures in gold nanoparticles can reach several hundred degrees while the heating is confined to an area of the order of several hundred nanometers outside the nanoparticle[67].

2.1.2.2 Heat Transfer to Gold Nanoparticle Surroundings

As described in the last section, gold nanoparticles can be optically heated by illumination near the plasmon resonance. To understand how the temperature is transfered to the nanoparticle surrounding one must look at the heat transfer equation[21]:

$$\rho(\vec{r})c(\vec{r})\frac{\partial T(\vec{r},t)}{\partial t} = \nabla\kappa(\vec{r})\nabla T(\vec{r},t) + Q(\vec{r},t) \tag{2.22}$$

Here, $\vec{r}$ and t are the spatial coordinate and time respectively, $T(\vec{r},t)$ is the local temperature and $Q(\vec{r},t)$ is the local heat intensity from the energy source pumping energy into the system. Three material parameters also factor into the equation: the material density, $\rho(\vec{r})$, the specific heat, $c(\vec{r})$, and the thermal conductivity, $\kappa(\vec{r})$, of the material. The energy source is of course the light dissipation in the gold nanoparticles and is given by:

$$Q(\vec{r},t) = \left\langle \vec{j}(\vec{r},t) \cdot \vec{E}(\vec{r},t) \right\rangle_t \tag{2.23}$$

with the current density, $\vec{j}(\vec{r}, t)$, and the electric field of the system, $\vec{E}(\vec{r}, t)$. The electric field is given by measuring the light intensity of the system and inserting this and the dielectric constant of the matrix, ε_0, into:

$$I(t) = I_0 = c\vec{E}_0^2 \frac{\sqrt{\varepsilon_0}}{8\pi} \tag{2.24}$$

In the case of a spherical nanoparticle of radius, R_{np}, in a medium with a dielectric constant, $\varepsilon_m(\omega)$, a time-dependent solution exists[68]. The steady-state solution, i.e. for $t \to \infty$, leads to a simple temperature distribution outside the nanoparticle:

$$\Delta T(\vec{r}) = \frac{V_{np}Q}{4\pi\kappa_m} \frac{1}{\vec{r}} \tag{2.25}$$

The maximum temperature, $\Delta T_{max}(I_0)$, occurs on the surface of the nanoparticle ($r = R_{np}$) and can be calculated by inserting the equation for heat dissipation:

$$Q = -\text{Re} \left[i\omega \frac{\varepsilon(\vec{r}) - 1}{8\pi} \vec{E}_0^2 \left| \frac{3\varepsilon_0}{2\varepsilon_0 + \varepsilon_m} \right|^2 \right] \tag{2.26}$$

and equation 2.24 into equation 2.25:

$$\Delta T_{max}(I_0) = \frac{R_{np}^2}{3\kappa_m} \text{Re} \left[i\omega \frac{1 - \varepsilon(\vec{r})}{8\pi} \left| \frac{3\varepsilon_0}{2\varepsilon_0 + \varepsilon_m} \right|^2 \right] \frac{8\pi I_0}{c\sqrt{\varepsilon_0}} \tag{2.27}$$

Only the real part of the brackets, Re, is taken. Figure 2.10 shows the temperature distribution for optically heated gold nanoparticles of different sizes in water. All are illuminated by the same laser power density. As shown in equation 2.27 the maximum temperature is at the surface of the nanoparticle and is nearly proportional to R_{np}^2; the temperature decreases rapidly with increasing distance from the nanoparticle. The extent of heating is larger for larger nanoparticles.

For some applications not only the maximal temperature around the gold nanoparticles is of interest, but also the time dependence of the temperature. An estimate[21] is provided for the time necessary to reach $\Delta T_{max}/2$:

$$t = \tau_0 = R_{np}^2/\alpha = R_{np}^2 \frac{c_w\rho_w}{\kappa_w} \tag{2.28}$$

with the thermal diffusivity, α, the thermal conductivity, κ_w, the mass density, ρ_w, and the specific heat capacity, c_w, of water. Taking the values at $20\,°\text{C}$ leads to a thermal diffusivity of $\alpha = 1.4 \times 10^{-7}\,\text{m}^2/\text{s}$ and thus to $\tau_0 \approx 3\,\text{ns}$ for $40\,\text{nm}$ gold nanoparticles and $\tau_0 \approx 11\,\text{ns}$ for $80\,\text{nm}$ gold nanoparticles. This formula gives a general estimate of the time dependence of the heating process. However, it can be useful to model the dynamics of the entire heating and subsequent cooling processes. For this it is practicable to use an approximation method, e.g. *finite*

Figure 2.10 | Steady-state temperature profiles for optically heated gold nanoparticles in water (laser power density P=40 kW/cm^2). The maximum temperature difference scales approximately with R_{np}^2 and the spatial extent of heating is also larger for larger nanoparticles.

element analysis, instead of trying to solve everything analytically. This is a technique for finding approximate solutions of partial differential equations. The technique relies on rendering the partial differential equations into an approximate system of ordinary differential equations, which are subsequently numerically integrated. In the present work the modeling was done with the software Comsol Multiphysics. As an example, an optically heated $80\,\text{nm}$ gold nanoparticle in water is simulated. A mesh structure is established (Figure 2.11a), in which the temperature transfer equations are solved analytically for each separate element and then the boundary conditions are taken into account. The result is a temperature distribution around the gold nanoparticle in all three dimensions (Figure 2.11b).

The temperature dynamics of the optical heating of gold nanoparticles can also be modeled with Comsol Multiphysics. As described in section 2.1.2.1, the gold nanoparticle reaches its maximal temperature within several nanoseconds. However, this depends on the thermal conductivity and the thermal capacity of the surrounding medium. For a gold nanoparticle in water, the heat rapidly dissipates through the water. It takes much longer for the gold nanoparticle to reach

Figure 2.11 | Heat-transfer simulations. (a) Mesh structure of the finite elements for a gold nanoparticle sitting on a phospholipid membrane. The heat transfer equation is solved in each element separately and the boundary conditions are then accounted for. (b) Steady-state temperature profile around an optically heated $80\,\mathrm{nm}$ gold nanoparticle in water (laser power density $P = 10\,\mathrm{kW/cm^2}$). The temperature increase in the surrounding medium is confined to a nanosized region around the nanoparticle.

equilibrium and it cannot heat up to the same degree as a gold nanoparticle in air. To show this effect the heating process of an $80\,\mathrm{nm}$ gold nanoparticle illuminated by a laser is simulated both for air and water as surrounding media. In air, the gold nanoparticle reaches 90% of its maximum temperature, $T_{max} = 159\,^\circ\mathrm{C}$, within $128\,\mathrm{ns}$. With water surrounding the gold nanoparticle, the maximum temperature at thermal equilibrium is $T_{max} = 26.2\,^\circ\mathrm{C}$ of which 90% is reached after $403\,\mathrm{ns}$. The dynamics of the heating and cooling process can be seen in Figure 2.12.
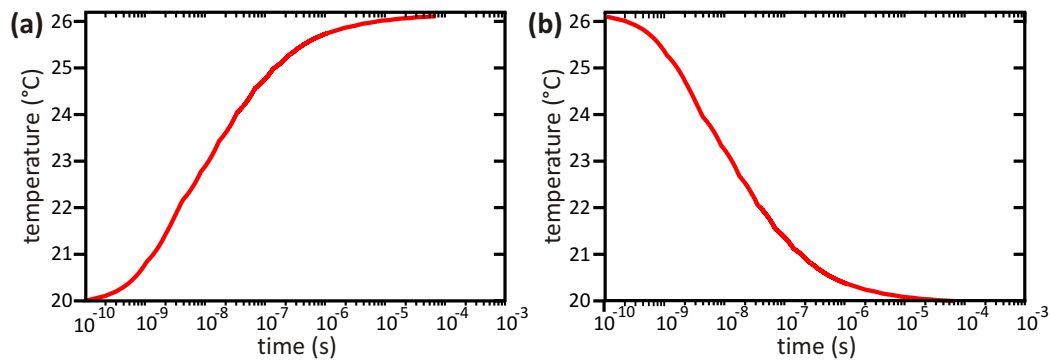
Figure 2.12 | Heating dynamics of a gold nanoparticle in water. (a) Temperature profile of an optically heated $80\,\mathrm{nm}$ gold nanoparticle. The nanoparticle reaches 90% of its maximum temperature after $403\,\mathrm{ns}$. (b) The same gold nanoparticle is heated to maximum temperature and then left to cool off. Again 90% of its final temperature is reached after $403\,\mathrm{ns}$

2.2 Optical Forces

As described in section 2.1.1.3, how light interacts with particles depends strongly on the ratio between the particle size and the wavelength of light. This ratio is divided into two size regimes. The first is the *Rayleigh scattering* regime, when the particles are much smaller than the wavelength of light (characteristically $d < 0.1\lambda$). Rayleigh scattering is most prominently seen in gases. It has a strong wavelength dependence ($I_{sca} \propto \lambda^{-4}$), which is the main reason for the blue colour of the sky during the day and the red coloring at sunset and sunrise[69]. The second regime is the *Mie scattering* regime, characterized by the particles being much larger than the wavelength of light. The intensity of Mie scattering is nearly independent of wavelength. Thus, scattering from water droplets in clouds is the reason for them appearing white when the sun is in front of them, and black when the sun is behind them[70].

In both modes of scattering, light exerts a force upon the particles. This total force depends on two separate forces, the *gradient force* and the *scattering force*. These forces were first detected on micrometer sized particles by Ashkin et al.[71] in 1970. Many years later they expanded their work and created a particle trap made entirely out of light[72]. These so called *optical tweezers* have since found wide application. Steven Chu was awarded a Nobel Prize in Physics for his work in cooling and trapping of neutral atoms[73]. Optical tweezers have also found wide use in the field of biology, e.g for trapping bacteria or conducting experiments on molecular motors[74,75].

For Mie scattering these forces can be understood using ray optics (Figure 2.13). If a laser beam impinges upon a particle, individual photons will be *reflected* as they hit the particle. According to Newton's third law, this change of momentum must be compensated by a force of equal magnitude but opposite direction. Thus, the reflection of light results in a force acting in the direction of light propagation and is known as the scattering force. The second force, the gradient force, is due to the difference in refractive indices between the particle and the surrounding medium. Here, individual rays of light will be refracted as they enter the particle. The rays

exit the particle in a direction different than from that in which they entered. Again, a change in momentum is involved and results in a force moving the particle towards the center of the laser beam.
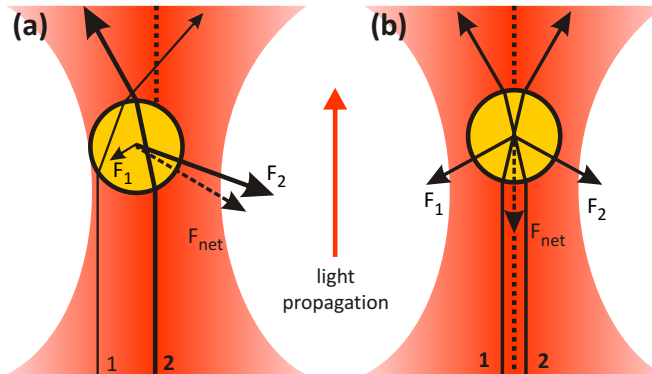
Figure 2.13 | Ray optics diagram of the gradient force acting on a particle inside a laser beam. (a) A particle not in the center of the laser beam experiences a restoring force due to the refraction of light, drawing it to the center. (b) The sum of the total forces in radial direction acting on a particle in the center of a laser beam is zero.

If the conditions for Rayleigh scattering are satisfied, then the particle can be treated as a point dipole in an inhomogeneous electromagnetic field. The force acting on this point dipole is known as the Lorentz force, $\vec{F} = q\left(\vec{E} + \frac{d\vec{r}}{dt}\text{x}\vec{B}\right)$. For a dipole in a laser field this becomes[76]:

$$\vec{F} = \frac{1}{2}\alpha\vec{\nabla}\left|\vec{E}\right|^2 \tag{2.29}$$

with the electric field, $\vec{E}$, and the polarizability, α. The square of the magnitude of the electric field is directly related to the local intensity via $I = c\varepsilon_0 n/2\left|\vec{E}\right|^2$ for a monochromatic propagating wave. Thus the force on the point dipole is proportional to the intensity gradient along the laser beam such that the gradient force attracts the particle to the position of highest intensity within the beam. The term scattering force is actually misleading in the Rayleigh regime, because it also is comprised of two separate forces, namely the actual *scattering force* and an *absorption force* resulting from momentum conservation after absorption of light by the particle. Both forces act in the direction of light propagation. Since many particles do not absorb light at specific wavelengths, the two forces are thus often combined into one single *scattering force*. In an optical tweezer the combination of all of these forces acting on a particle will lead to it being trapped. Its trapping position is in the beam center in the radial direction, but slightly behind the focal plane due to the scattering force acting against the gradient force.

2.3 Derjaguin-Landau-Verwey-Overbeek Theory

The Derjaguin-Landau-Verwey-Overbeek theory (DLVO-theory) is, despite its age, still the basic theory that researchers use as a starting point for understanding the stability and phase behaviour of colloidal dispersions. It uses a linear combination of a screened repulsive Coulomb potential and the van der Waals potential[77] and goes back to the work done by Derjaguin and Landau in 1941[78] and Verwey and Overbeek seven years later[79]. A charged nanoparticle in a liquid will bind ions of the opposite charge to the surface. The total surface charge of the nanoparticle is balanced by an equal but oppositely charged region of so called *counterions* (Figure 2.14). These

Figure 2.14 | Electric double layer of a charged surface in a liquid. The negatively charged surface attracts oppositely charged ions, some of which adsorb to the surface in the Helmholtz layer. Further away from the surface ions are only lightly bound to the surface and move around in the diffuse electric double layer. When the nanoparticle moves the ions that are more strongly bound will move with it. The plane up until which this happens is known as the slipping plane, and the potential at this plane is the zeta potential.
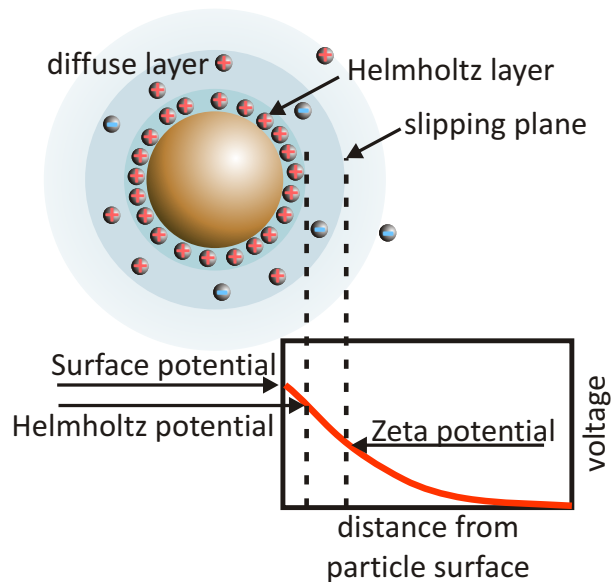
are divided into two layers: those transiently bound to the surface in the *Helmholtz layer* and those that form an atmosphere of ions in the diffuse *electric double layer*. These later ions are in rapid thermal motion close to the nanoparticle surface. The thickness of the electric double layer is known as the *Debye screening length*, κ^{-1}, and is given by

$$\kappa = \left(\sum_i \rho_{\infty,i} e^2 z_i^2 / \varepsilon \varepsilon_0 kT \right)^{1/2} \tag{2.30}$$

with the number density of ion of type i in the bulk solution $\rho_{\infty,i}$, the valency of the ion, z, and the relative static permittivity of the liquid, ε. The electric potential energy falls off very sharply with increasing distance to the particle surface and is

reduced to 2% of the value at the surface wall at a distance of two Debye screening lengths. When the nanoparticle moves through the solution, those ions that are close enough to the nanoparticle in the diffuse layer will move with the particle. The boundary for this is known as the *slipping plane* and the potential between this point and zero potential is known as the *zeta potential*, ζ. This potential serves as a measure of stability of colloidal dispersions. The zeta potential indicates how strongly particles of the same charge will repel each other. For a strong zeta potential the repulsion is strong and the dispersion resists aggregation. On the other hand, a low zeta potential means that attraction between the nanoparticles is larger than repulsion and the dispersion will flocculate. Generally the dividing line between unstable and stable suspensions is drawn at ± 30 mV, with nanoparticles having values outside of this range considered stable[80]. If the nanoparticles have a larger density than the dispersant, they will still sediment after a given time[81]. The interaction free energy between two nanoparticles is given by:

$$W(d) = \left(64\pi kTr\rho_\infty\gamma^2/\kappa^2\right)e^{-\kappa d} \tag{2.31}$$

with the reduced surface potential, $\gamma = tanh\left(\frac{ee\psi_0}{4kT}\right)$, the potential on the surface, ψ_0, and the distance between the two nanoparticles, d. The *Derjaguin approximation* gives the force between two spheres in terms of the energy per unit area of two flat surfaces at the same separation. The force is given by $F(d) = 2\pi\left(\frac{r_1r_2}{r_1+r_2}\right)W(d)$ yielding the force resulting from the electric double layer for the cases of a sphere near a flat surface ($F_{sph-sur}$) or of two spheres ($F_{sph-sph}$):

$$F_{sph-sur}(d) = 2\pi r_1 W(d) \tag{2.32}$$

$$F_{sph-sph}(d) = \pi r W(d) \tag{2.33}$$

The second important force acting upon particles (in liquids) in close proximity to each other is the *van der Waals force*. This force actually encompasses several forces: the force between two permanent dipoles (*van der Waals-Keesom force*), the force between a permanent dipole and a corresponding induced dipole (*van der Waals-Debye force*) and the force between two instantaneously induced dipoles (*London dispersion force*). H.C.Hamaker was the first to realize that the formalism of van der Waals forces could be extended from the interaction of two molecules with induced

dipoles to macro-scale objects[82]. This is done by integrating over all the forces of all the atoms in one body with all the atoms of the other body. With the interatomic van der Waals pair potential, $w(r) = -C/r^6$, one obtains thus a two-body potential for any kind of geometry. The interaction energies for two spheres (a), a sphere and a flat surface (b) and two flat surface (c) are given by:

$$W_{sph-sph}(d) = \frac{-A}{6d} \frac{r_1 r_2}{(r_1 + r_2)} \tag{2.34a}$$

$$W_{sph-sur}(d) = \frac{-Ar}{6d} \tag{2.34b}$$

$$W_{sur-sur}(d) = \frac{-A}{12\pi d^2} \tag{2.34c}$$

with the radii of the two spheres, r_1 and r_2, the distance between them, d, and the Hamaker constant, $A = \pi^2 C \rho_1 \rho_2$. This is based on the assumption of simple pairwise additivity and ignores the influence of neighboring atoms on the interaction between any pair of atoms. This assumption is avoided in the *Lifschitz theory*, which ignores the atomic structure and instead derives the bodies, now treated as continuous media, in terms of bulk properties, e.g. dielectric constants and refractive indices. This theory does not change the validity of the expressions in equation 2.34, but instead yields more accurate values for the Hamaker constant[83]. The derivation of the formulas for the Hamaker constant will not be covered here, but is explained in detail elsewhere[84]. There, based on the Lifshitz theory, the Hamaker constant for the interaction of medium 1 and medium 2 across a third medium 3 is given by:

$$A \approx \frac{3}{4}kT \left(\frac{\varepsilon_1 - \varepsilon_3}{\varepsilon_1 + \varepsilon_3} \right) \left(\frac{\varepsilon_2 - \varepsilon_3}{\varepsilon_2 + \varepsilon_3} \right)$$
$$+ \frac{3h}{4\pi} \int_{\nu_1}^{\infty} \left(\frac{\varepsilon_1(i\nu) - \varepsilon_3(i\nu)}{\varepsilon_1(i\nu) + \varepsilon_3(i\nu)} \right) \left(\frac{\varepsilon_2(i\nu) - \varepsilon_3(i\nu)}{\varepsilon_2(i\nu) + \varepsilon_3(i\nu)} \right) d\nu \tag{2.35}$$

where ε_1, ε_2 and ε_3 are the static dielectric constants of the three media, $\varepsilon(i\nu)$ are the values of ε at imaginary frequencies and $\nu_n = (2\pi kT/h)n$. To obtain the Hamaker constant for an arbitrary system, the dependence of the dielectric permittivities of the media on the frequency must be known, so that equation 2.35 can be integrated. These permittivities vary with frequency in a similar way to the atomic polarizability

of an atom. This leads to a form for the dielectric permittivities:

$$\varepsilon(i\nu) = 1 + (n^2 - 1)/(1 + \nu^2/\nu_e^2) \tag{2.36}$$

which can be substituted into equation 2.35 and leads to an approximate expression for the non-retarded Hamaker constant for two macroscopic phases 1 and 2 interacting across medium 3[85]:

$$A \approx \frac{3}{4}kT \left(\frac{\varepsilon_1 - \varepsilon_3}{\varepsilon_1 + \varepsilon_3}\right) \left(\frac{\varepsilon_2 - \varepsilon_3}{\varepsilon_2 + \varepsilon_3}\right)$$
$$+ \frac{3h\nu_e}{8\sqrt{2}} \frac{(n_1^2 - n_3^2)(n_2^2 - n_3^2)}{(n_1^2 + n_3^2)^{1/2}(n_2^2 + n_3^2)^{1/2}[(n_1^2 + n_3^2)^{1/2} + (n_2^2 + n_3^2)^{1/2}]} \tag{2.37}$$

where n_i are the refractive indices of the respective medium, ε_i are their dielectric permittivities and ν_e is the main electronic absorption frequency. This expression for the Hamaker constant can be applied to any of the geometries in equation 2.34. Interestingly, a result from equation 2.37 is that the van der Waals force between two identical bodies in a medium is always attractive (Hamaker constant is positive), but for different bodies the Hamaker constant can be either positive or negative resulting in either an attractive or repulsive van der Waals force. Values for Hamaker constants are often unknown. In this case approximate values can be obtained by applying combining relations (or combining laws). With the Hamaker constant, A_{132}, which is valid for media 1 and 2 interacting across medium 3 one obtains a relation for A_{132} with A_{131} and A_{232} via $A_{132} \approx \pm\sqrt{A_{131}A_{232}}$ and from this one obtains $A_{12} \approx \sqrt{A_{11}A_{22}}$, where A_{12} is the Hamaker constant for media 1 and 2 interacting across a vacuum. Three other useful relations are[86]:

$$A_{131} \approx A_{313} \approx A_{11} + A_{33} - 2A_{13} \tag{2.38}$$

$$\approx \left(\sqrt{A_{11}} - \sqrt{A_{33}}\right)^2 \tag{2.39}$$

$$A_{132} \approx \left(\sqrt{A_{11}} - \sqrt{A_{33}}\right)\left(\sqrt{A_{22}} - \sqrt{A_{33}}\right) \tag{2.40}$$

These equations can be very useful when the Hamaker constants of individual materials are known, but not those of the entire system. The theory can be further extended to include adsorbed layers (Figure 2.15). For the van der Waals force between two surfaces 1 and 1' with adsorbed layers 2 and 2' of thickness l and l' across medium 3 of thickness d one obtains:

$$F(d) = \frac{1}{6\pi} \left[\frac{A_{232'}}{d^3} - \frac{\sqrt{A_{121}A_{32'3}}}{(d+l)^3} - \frac{\sqrt{A_{1'2'1'}A_{323}}}{(d+l')^3} + \frac{\sqrt{A_{1'2'1'}A_{121}}}{(d+l+l')^3} \right] \qquad (2.41)$$

For the two cases, when the surfaces are either very close or very far apart from each other, this equation reduces to:

$$F(d) = A_{2'32}/6\pi d^3 \quad \text{for} \quad d << (l+l') \qquad (2.42)$$

$$F(d) = A_{1'31}/6\pi d^3 \quad \text{for} \quad d >> (l+l') \qquad (2.43)$$

Accordingly, the van der Waals interaction is dominated by the properties of the bulk material at large separations and by the properties of the adsorbed layers at distances less than the thickness of the layers[84].
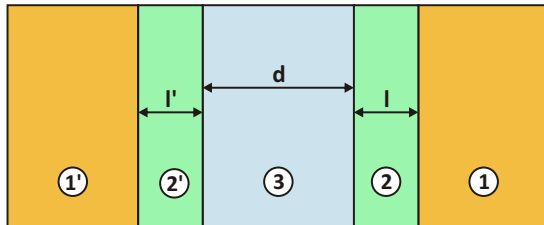
Figure 2.15 | Forces between surfaces with adsorbed layers. The van der Waals interaction is dominated by the properties of the surface material (1 and 1') at large separations and by the properties of the adsorbed layers (2 and 2') at separations less than the thickness of the layers[84].

2.4 Biological Membranes

All cells (both eukaryotic and prokaryotic) are surrounded by a plasma membrane, which shields the cell from its environment. The membrane serves as a barrier to the passage of all but lipophilic molecules, allowing small uncharged molecules such as oxygen or ethanol to pass, but being impermeable to large molecules such as glucose or amino acids and also to ions. Furthermore, the cellular or sub-cellular membranes are the site of many important processes, such as cellular transport, nutrient recognition and signaling (Figure 2.16). To study such processes one must have knowledge of the general properties and compositions of membranes.
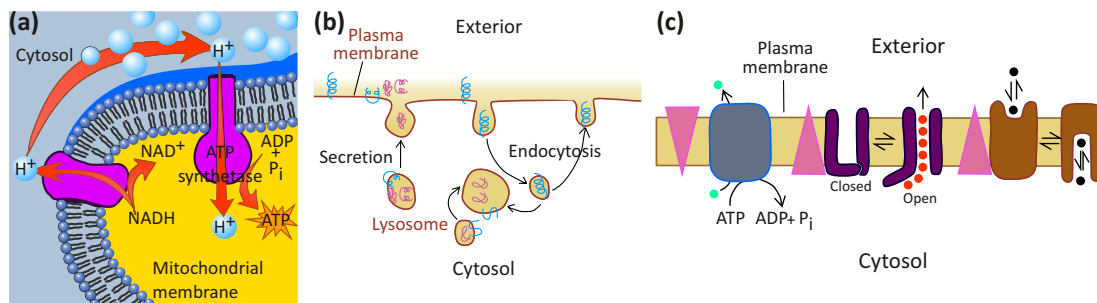
Figure 2.16 | Important processes occurring in or at cellular and subcellular membranes. (a) cellular respiration, (b) nutrient recognition and (c) ion transport/signaling.

2.4.1 Membrane Lipids

Phospholipids are the primary building block of all cell membranes. With their amphiphilic structure, consisting of a phosphate-containing hydrophilic head group attached to two hydrophobic fatty acid chains (Figure 2.17a), phospholipids sponta-neously form bilayers in aqueous solutions. The headgroups of the lipids form the outside of the bilayer, shielding the hydrophobic chains from the water surrounding the lipids (Figure 2.17b). These bilayers are highly stable structures and represent the basic structure of all biological membranes. Lipids themselves make up a large part of most cell membranes. Depending on the type of membrane, they typically constitute 50% of the mass of the membrane (e.g. plasma membranes). Extreme membranes are the inner membrane of mitochondria with only 25% of the mass from phospholipids and E.coli plasma membranes with 80% of the mass from

(a) **(b)**
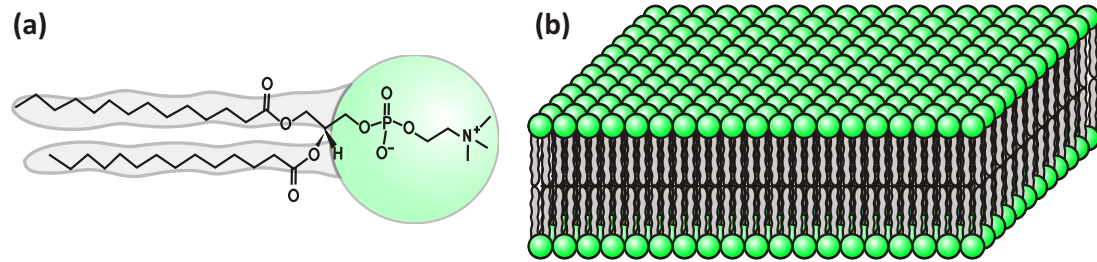
Figure 2.17 | Phospholipids are one of the primary building block of cell membranes.
(a) Chemical structure of a typical phospholipid molecule *(1,2-dimyristoyl-sn-glycero-3-phosphocholine* or *DMPC).* The hydrophilic headgroup is attached to two fatty acid chains.
(b) Because of the amphiphilic structure of phospholipids, they spontaneously form bilayers in aqueous solutions with the hydrophobic chains shielded from the water by the hydrophilic headgroups.

phospholipids. Mammalian plasma membranes are made up of four major types of phospholipids: phosphatidylcholine, phosphatidylserine, phosphatidylethanolamine and sphingomyelin. Each type again is comprised of many different phospholipids with identical headgroups, but different chain lengths and even chain numbers. The two other main components of the membrane lipids are the glycolipids and cholesterol. Apart from their role of forming cell membranes, phospholipids also function as signaling molecules both between and within cells[87].

2.4.2 Lipid Bilayers

In the last section it was said that phospholipids spontaneously form bilayers in aqueous solutions. This is only partly true, as some phospholipids form other structures, such as spherical micells, cylindrical micells or inverse micells[88]. However, the phospholipids involved in forming the plasma membrane all have a *critical packing parameter*, which allows them to form bilayers. This parameter is a measure of the dimensions of the phospholipid and is calculated by: $P_{cr} = V/A \cdot l$, with the volume of the phospholipid, V, the interfacial area, A, and the length of the molecule, l. If the phospholipid molecules have a value of P_{cr} between $1/2$ and 1, they can form bilayers.

These bilayers can be in several lamellar phases, which differ strongly in many physical parameters. The four main phases are: the crystalline phase, L_c, the gel-phases , L_β, $L_{\beta'}$ and $L_{\beta 1}$, the ripple-phase, $P_{\beta'}$, and the liquid-crystalline phase, L_α. In the crystalline phase the phospholipids are arranged in bilayers which are stacked on top of each other. The phospholipid headgroups form a periodic hexagonal lattice and have a long range order. The aliphatic chains are in the all-trans conformation (Figure 2.18a). This phase forms spontaneously through self-organization when a solution of phospholipids is dried. The electroformation method for creating giant unilamellar phospholipid vesicles (section 3.2.1) uses this self-organization.
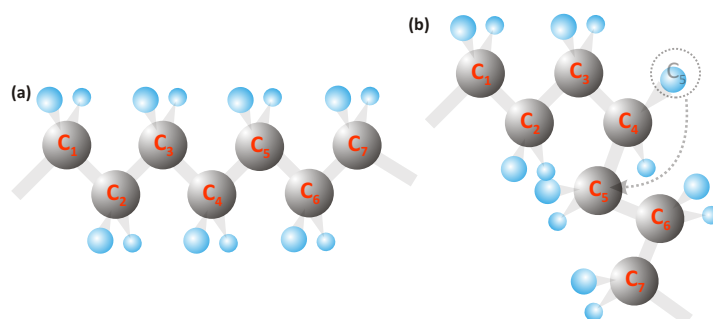
Figure 2.18 | Conformations of phospholipid aliphatic chains. (a) At low temperatures all carbon bonds in the aliphatic chains of phospholipids are in the trans configuration. (b) For higher temperatures some of these bonds go over to the gauche-configuration as here between the C_4 and C_5 atoms.

Upon addition of water, the water molecules accumulate near the polar part of the phospholipid molecules and the headgroups become hydrated. The individual phospholipid bilayers separate and undergo a phase-transition to the gel-phase. In this phase the chains are also stiff and fully extended (all-trans). The difference between the three gel phase configurations lies in the alignment of the chains. These can be parallel to the bilayer normal (L_β), tilted ($L_{\beta'}$) or interdigitated ($L_{\beta 1}$) (Figure 2.19). Which of these phase configurations the bilayer assumes depends on the relation between the headgroup spacing and the cross-sectional area of the chains, which characteristically has a value of approximately $0.21\,\mathrm{nm}^2$. If the headgroup packing requirement is close to twice the value of the cross-sectional chain area, the phospholipids arrange themselves in the untilted phase. For a larger headgroup requirement the tilted phase is assumed to accommodate the mismatch.
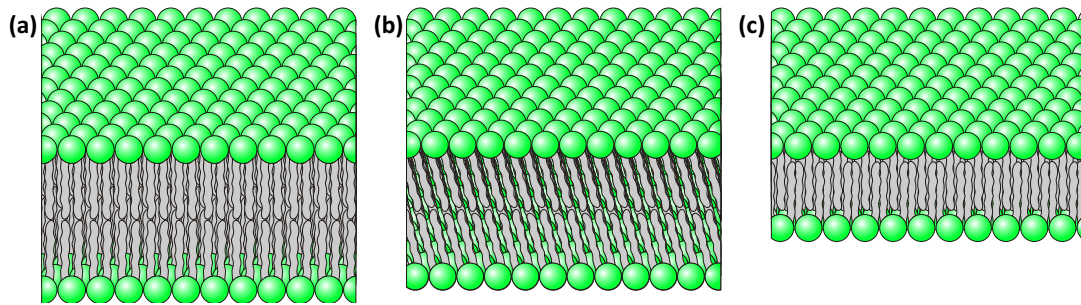
Figure 2.19 | Three possible configurations for gel-phase membranes. Which configuration occurs depends on the lipid species and the ratio of the headgroup spacing to the cross-sectional-area of the chains. (a) The non-tilted gel phase (L_β) occurs for phospholipids with small headgroups with a spacing requirement of up to $0.42\,\text{nm}^2$. (b) For larger headgroup spacing requirements, the membrane forms in a tilted-phase ($L_{\beta'}$) (c) and for head group spacing requirements larger than $0.84\,\text{nm}^2$ an interdigitated gel phase ($L_{\beta 1}$) is formed.

The phospholipid molecules are tilted at an angle of around $30°$ in this configuration[89]. For extreme mismatches, the interdigitated phase can be assumed with an available packing area of $0.84\,\text{nm}^2$ possible[90]. If the temperature of the system is raised, then another phase transition can occur for certain phospholipids from the gel phase to the ripple phase ($P_{\beta'}$) (Figure 2.20a). Here, the lipid chains are no longer solely in the all-trans configuration, instead part of the bonds change to the gauche-configuration producing kinks in the aliphatic chains (Figure 2.18b).

This configuration is energetically less favorable because the kinks in the phospholipid tails lead to larger chain separations, reducing the van der Waals interactions. It therefore only occurs at higher temperatures. The lipid chains are no longer fully extended and the headgroups also lose their order. This leads to an increase of cross-sectional area per lipid of around 24%. In this phase the bilayer is
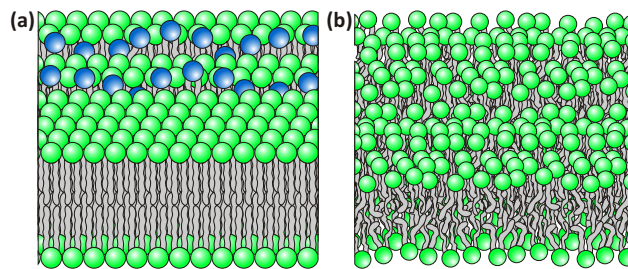
Figure 2.20 | Ripple-phase P_β **and fluid phase** L_α. (a) Upon heating over the pretransition temperature, T_p, linear distortions of melted lipids form in the membrane. (b) For further heating above the main transition temperature, T_m, the entire membrane melts and goes over into the fluid phase.

distorted by periodic ripples with periods between 10 and $30\,\mathrm{nm}$[91]. The ripples are caused by single lipids undergoing a phase transition to the fluid-phase. These molecules form one-dimensional defects due to the triangular lattice and lead to a local bending of the phospholipid bilayer. These defects can be seen as height modulations in the membrane, but as stated before only occur in some phospholipids under high hydration[92]. The temperature for this transition is known as the *pre-transition temperature*, T_p. For even higher temperatures the bilayer undergoes a final transition to the fluid phase, L_α, (Figure 2.20 b). In this phase all lipid chains are *melted* and the headgroups are no longer arranged in a lattice. Water can enter the headgroup region, increasing the cross-sectional area of the lipid molecules by up to 24%[93]. Simultaneously, because the chains are no longer fully extended, the bilayer thickness is reduced by up to 30%[94]. The temperature at which this transition occurs is known as the *main transition temperature* or *melting temperature*, T_m. This temperature is influenced by several factors.

Increasing chain length leads to larger van der Waals interactions and thus to higher melting temperatures. This increase is approximately linearly proportional to the chain length (Figure 2.21). Chain unsaturation, i.e. the presence of double bonds in the chains, leads to a large reduction of T_m. The double bond decouples the parts of the chain on either side of the double bond, and thereby reduces the length of the parallel, strongly interacting chain segments. This has the same effect as a chain shortening. The headgroup also plays a large role in determining T_m, as can be seen in Figure 2.21. For identical chain lengths phos-
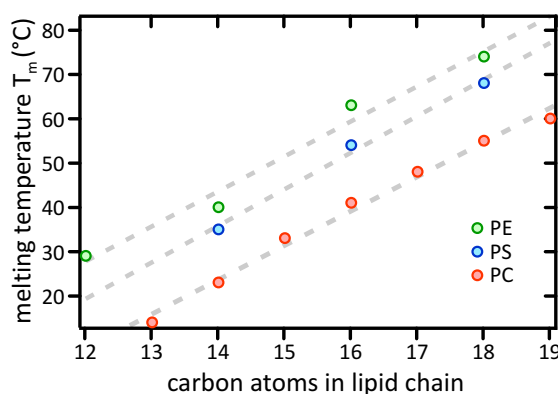
Figure 2.21 | For saturated phosphatidylcholines, the main transition temperature T_m depends almost linearly on the chain length. Increasing the chain length increases the van der Waals forces between the chains and thus raises T_m. The headgroup also plays a large role in defining T_m. For the same chain length but different headgroups, phosphoethanolamine (PE) has the largest T_m, followed by phosphoserine (PS) and phosphocholine (PC), having the lowest.

phoethanolamines have a higher T_m than phosphoserines, which in turn have a higher T_m than phosphocholines. For mixtures of lipids with different transition temperatures, the effective melting temperature lies between the single lipid temperatures and depends on the lipid mixture ratio. However, for bilayers comprised of lipids with different melting temperatures phase separation can occur. Thus parts of the bilayer can already be fluid, while others are still in the gel-phase. This phase separation plays a crucial role in certain biological phenomena. Membrane components, e.g. proteins, can partition favorably into one of the phases and so be locally concentrated or activated[95].

Many physical parameters of a phospholipid bilayer change considerably upon undergoing the transition from the gel phase to the fluid phase. As stated before, water entering the headgroup region and the formation of gauche-bonds reduces the lipid binding, increasing the bilayer surface area while reducing the bilayer thickness. Another very important factor is the dramatic increase of lipid mobility. Generally, there are two possibilities for lipids molecules to move within the membrane, either to undergo a *lateral exchange* with a neighboring molecule ot to *flip-flop* between the inner and outer leaflet of the bilayer. The flip-flop is a very slow process[96] with exchange rates of $2 \times 10^{-3} - 0.11 s^{-1}$. This is because the hydrated head-group must cross the hydrophobic core of the bilayer, an energetically unfavourable process. However, in a bilayer in the fluid-phase, a lipid molecule will laterally exchange its place with a neighbor once every 100 ns on average. This leads to lipid diffusion constants of roughly $1\,\mu m^2/s$. In the gel phase this value is two to three orders of magnitude lower[89]. Bilayer fluidity is particularly crucial from the biological point of view[97]. Very importantly, fluid bilayers are able to reseal small holes quickly[98,99]. Also, bilayer fluidity enables protein mobility and synthesis as well as many other processes[100]. Living organisms try to keep their membrane bilayers in the fluid phase slightly above the main transition temperature. They do this by synthesizing appropriate phospholipid molecules or by chemical chain modifications[90].

One of the shapes a phospholipid bilayer can assume is that of a vesicle. A vesicle can be comprised of a single bilayer (*unilamellar* vesicle) or of several bilayers

(*multilamellar* vesicle). These generally spherical structures are quite common in living organisms and are used, e.g. for signaling between cells or for endocytosis and exocytosis, the processes through which a cell brings molecules into or expels them from the cell[101]. Vesicles were first artificially created by shaking a lipid-water mixture[102]. However, once their enormous scientific potential had been recognized, many different methods for creating vesicles were established[33]. Vesicles are effectively model cells, but reduced to only a lipid membrane. Without many of the other structures normally present inside living cells, the study of membrane processes becomes much easier with artificial cells. The reduction of the number of variables present in the system permits the study of specific characteristics of the membrane, e.g. mechanical properties[103], transport phenomena[104,105], or osmotic effects[106]. Depending on the study, vesicles of all sorts of size ranges can be produced, from below $100\,\mathrm{nm}$ in diameter (SUV - small unilamellar vesicle) to well over $1\,\mu\mathrm{m}$ (GUV - giant unilamellar vesicle, which are of the same size order as biological cells). Intermediate vesicles (diameter $0.1 - 1\,\mu\mathrm{m}$) are known as LUVs or large unilamellar vesicles. SUVs tend to fuse together, forming LUVs, in order to reduce high surface tension[107]. LUVs and GUVs are in contrast very stable.

GUVs produced for the experiments of this thesis were stable over several weeks, showing no signs of deformation or size variations over time. Even though vesicles are commonly spherical, they can have all sorts of faceted shapes. Vesicles in the fluid phase are generally spherical (Figure 2.22) because this is the energetically most stable shape and fluid membranes have a high elasticity. On the other hand, gel phase vesicles (Figure 2.23) have much more rigid membranes and thus often have faceted shapes.
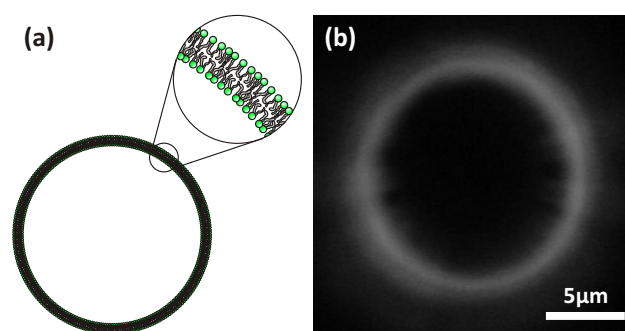
Figure 2.22 | Phospholipid vesicle in the fluid phase. (a) In the fluid phase a phospholipid vesicle often forms a sphere, because this is the energetically favorable shape as depicted in this diagram. (b) The membrane scatters light efficiently around $400\,\mathrm{nm}$ wavelength and can thus be easily seen in a dark field microscope.

The shape differences result from differing membrane elasticities of the various phases[108]. A possible reason for the creation of faceted shapes is non-uniform cooling of fluid-phase vesicles below the main transition temperature. Some parts of the membrane have already entered the gel phase while the rest of the fluid phase membrane reshapes to minimize the energy in the system, thereby deforming the vesicle.
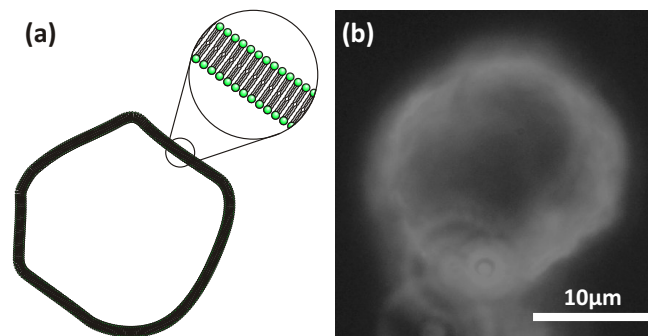
Figure 2.23 | Phospholipid vesicle in the gel phase. (a) Diagram of a gel phase vesicle (the membrane is magnified to show its structure). In this phase the membrane is much more rigid and often assumes a faceted shape. (b) Dark field image of a gel phase vesicle. The membrane appears thicker than $5\,$nm, because of the diffraction limit of the scattered light.

3 Methods and Materials

This chapter lists all of the methods and materials used to prepare the samples for the measurements and to perform the actual experiments. The experiments of this dissertation can be categorized into two groups. The first group focuses on the interaction of nanoparticles with light. This was exploited to print complex structures with metallic nanoparticles on glass coverslips (chapter 4), both of which had to be modified depending on the experiment (sections 3.2.2 and 3.2.3). The second group of experiments deals with the interaction between gold nanoparticles and phospholipid membranes (chapter 5). Giant unilamellar vesicles were grown (section 3.2.1). As in the first part of the experiments, the gold nanoparticles and glass coverslips had to be modified according to the experimental settings. Section 3.1 contains the methods and setups used to monitor the surface modification of gold nanoparticles and also the dark field microscope, the basis for the majority of the experiments conducted here.

3.1 Experimental Setups

3.1.1 Dark Field Microscope

The most important setup for this thesis work is a dark field microscope (Axiotech 100, Carl Zeiss MicroImaging GmbH), a diagram of which can be seen in Figure 3.1. The basis of this setup is an upright microscope, with illumination from below the sample. Illumination can be switched, depending on the measurements, between a $100\,W$ halogen lamp and a $50\,W$ mercury lamp. The light passes through a filter wheel for selecting specific excitation wavelengths to be passed on to the dark field condensor. In the condensor the light is blocked in the middle of the beam and focused onto the sample at a wide angle. Provided the *numerical aperture* (*NA*) of the condensor is higher than that of the microscope objective, the excitation light will bypass the objective and not enter it, hence the name dark field. Light, however, that is scattered by particles in the solution or emitted by fluorescent or phosphorescent molecules is emitted isotropically. This light can be collected by the objective and be seen because of the missing background light. Thus gold nanoparticles down to a size of $20\,nm$ in diameter, invisible in other microscope setups, can be easily seen in a dark field microscope. In this setup an oil immersion dark field condensor is used with an NA of $1.2 - 1.4$. An oil drop with a refractive index matched to the glass coverslips ($n = 1.518$) is brought onto the condensor, and the glass coverslip (thickness: $0.19 - 0.23\,mm$) is brought into contact with the oil drop. The glass coverslip itself is fixed to a self-made three dimensional piezo scanning stage with a resolution of $15\,nm$. The scanning stage is controlled by a gamepad. The sample is placed onto the glass coverslip and can be viewed with a objective. The objectives used in this thesis were two water immersion objectives (100x - NA 1.0 and 63x - NA 0.95) and two air objectives (10x - NA 0.2 and 100x - NA 0.75), all purchased from Carl Zeiss MicroImaging GmbH. The light that is collected by the objective passes through a 50/50 beam splitter which is used to couple lasers into the microscope. These are used for manipulation of the samples, as will be explained in chapters 5 and 4. The lasers used here were a *continuous wave* (*cw*) diode-pumped Nd:YAG laser (Millennia V, Spectra Physics Lasers GmbH) with a wavelength of $532\,nm$ and a maximum output power of $4\,W$, a cw argon-ion laser (Model 2020, Spectra Physics Lasers GmbH) with emission lines between $457\,nm$ and $514\,nm$ and a Ti:Sa laser
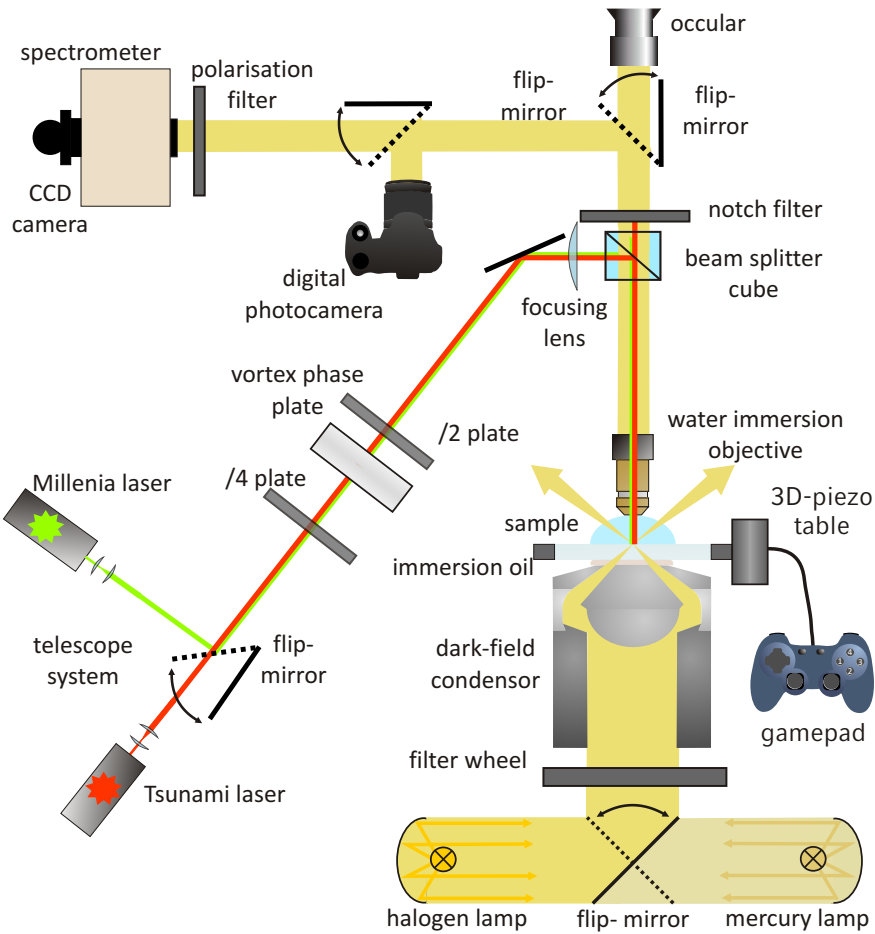
Figure 3.1 | Diagram of the dark field microscope used in the measurements.

(Tsunami, Spectra Physics Lasers GmbH), which is also pumped by a Millennia V laser. The Tsunami is tunable between about $700\,\text{nm}$ and $900\,\text{nm}$ and can be operated either in cw or in *mode-locked* mode. In the mode-locked mode, the Tsunami emits a pulsed beam with pulses around $100\,\text{fs}$ long and $15\,\text{nm}$ wide. Between the laser output and the 50/50 beam splitter are several options to modify the beam. Among others, are a half-wave plate to rotate the angle of the linearly-polarized laser beams, a quarter-wave plate to convert these beams to a circular polarization, and a vortex-phase plate (RPC Photonics, Inc.) to create a radially polarized beam. A telescope system can be used to expand the laser beams and also to shift the laser focus in z-dimension with respect to the surface of the glass coverslip. A notch-filter behind the

50/50 beam-splitter prevents any laser light from being passed on to the detection. Alternatively, band-pass filters or razor-edge filters can be used depending on the type of measurement conducted. The light passing the filter can be detected by three different methods. The ocular of the microscope enables the user to look at the sample directly and position it with respect to the laser. A digital camera (Canon EOS 550D) can be used to take optical images of the sample. A spectrometer (Acton SpectraPro 300i) coupled to a liquid nitrogen-cooled CCD-system (Princeton Instruments Spec-10) is available to obtain spectral information of the detected light. The spectrometer is equipped with three diffraction gratings (300, 600 and 1200 lines/mm), enabling both high-resolution measurements (1200 l/mm grating) and also measurements with a high spectral range (300 l/mm grating).

3.1.2 UV-VIS-NIR Spectrophotometer

There are two major classes of *spectrophotometers* that measures light intensity as a function of the light source wavelength, single beam and double beam. Whereas a single beam spectrophotometer measures the relative intensity of the beam before and after a test sample is inserted, the double beam spectrophotometer employs two light paths to simultaneously measure the test and reference samples. With a sample inserted into the light path, the excitation light will be absorbed and scattered by the sample. The remaining light reaching the detector thus gives information about the extinction spectrum of the sample. This can be used to detect certain substances or measure concentrations. A single-beam spectrophotometer (model Cary 50, Varian, Inc.) was used to measure extinction spectra for this thesis. It uses a Xenon flash lamp as a white light source and a Czerny-Turner monochromator to select the wavelength. A beam splitter splits the incoming light into two parts, with one part, I_0, going to a reference photodiode and the other part, I, first passing through the test sample. The ratio of these two intensities is the *transmittance*, T, and is related to the mean extinction cross section per nanoparticle, $\overline{\sigma_{ext}}$, the molar concentration of the nanoparticles, c_{mol}, the Avogadro constant, N_A, and the path length of the light through the sample, l, via the *Beer-Lambert law*:

$$T(\lambda) = \frac{I}{I_0} = e^{-N_A \overline{\sigma_{ext}} c_{mol} l} \tag{3.1}$$

This is used, for example, to determine the concentration of gold nanospheres of a given size in a colloidal suspensionas the extinction cross-section of gold nanospheres at $520\,\text{nm}$ is known and as the transmittance at this wavelength can be measured.

Often, instead of the transmittance, the *absorbance*, A, of a sample is used, also known as the *optical density*, OD. This is directly related to the transmittance via:

$$A = -log_{10}T \tag{3.2}$$

3.1.3 Fluorescence Spectrophotometer

Instead of measuring the difference between the emitted light and the light reaching the detector, a fluorescence photometer measures light created in a fluorescent sample. To assure no excitation light reaches the detector, the fluorescence, which is emitted isotropically, is collected in an angle of $90°$ with respect to the angle of excitation. A Cary Eclipse fluorescence spectrophotometer (Varian Inc.) was used to measure the fluorescence of several luminescent dyes. It is important to measure strongly diluted samples (absorbance < 0.05) in order to avoid *reabsorption*. This occurs when fluorescence photons emitted by a molecule within the sample are absorbed by another molecule, which can then also emit a photon. Because of the *Stokes-shift* of fluorescent molecules, the process of reabsorption leads to a red-shift of the fluorescence spectrum.

3.1.4 Zeta-Sizer

As described in section 2.3, the magnitude of the zeta potential gives an indication of the stability of a colloidal system. The most widely used theory for calculating the zeta potential from experimental data was developed by Smoluchowski in 1903[109]. The theory is valid for arbitrary nanoparticle shapes and concentrations. However, there are limitations, as the theory is valid only for thin double layers, when the radius of the nanoparticle is much larger than the Debye length: $a >> \kappa^{-1}$. The

zeta potential, ζ, is related directly to the electrophoretic mobility, μ_{el}, by:

$$\mu_{el} = \frac{\varepsilon_r \varepsilon_0 \zeta}{\eta} \tag{3.3}$$

with the dielectric constant of the dispersing medium, ε_r, and its dynamic viscosity, η. Thus by measuring the electrophoretic mobility of the nanoparticles in solution, one obtains their zeta potential. As suitable method is *dynamic light scattering*. Light hitting small particles (in the Rayleigh regime) is scattered in all directions. If this light is monochromatic and coherent (e.g. from a laser) then the scattering intensity displays time-dependent fluctuations due to the Brownian motion of the nanoparticles. Light scattered from two nanoparticles can interfere either constructively or destructively, and because the nanoparticles have a relative velocity to each other, this interference also fluctuates in time according to their motion. Thus the intensity fluctuation contains information about the time scale of the nanoparticles movement. The dynamic information of the particles is obtained by autocorrelating the scattering intensity for increasing time intervals. At short time intervals the correlation is high, because the particles do not have much time to move between measurements, and thus the state after a short time interval, τ, is almost the same as the initial state. As the time interval becomes longer, the correlation decays exponentially down to zero. This exponential decay is related to the diffusion coefficient, D, of the nanoparticles and is fitted numerically to obtain values of D. A charged particle with an effective charge equal to $Q = 4\pi\varepsilon_0\varepsilon_r\zeta R_H$ exposed to an electric field, $\vec{E}$, will experience the Coulomb force:

$$\vec{F} = Q\vec{E} = 4\pi\varepsilon_0\varepsilon_r\zeta R_H \vec{E} \tag{3.4}$$

and be accelerated. The nanoparticle experiences a frictional force, which acts against the acceleration and is given by *Stokes' law*: $\vec{F}_d = -6\pi\eta R_H \vec{v}$ with the hydrodynamic radius of the object, R_H, and its velocity, $\vec{v}$. This force increases linearly with velocity and leads to a maximum velocity of the nanoparticles. When nanoparticles are accelerated with a sinusoidal electrical field, this results in a time-dependent velocity, $v(t) = sin\left(\omega_e t\right)\mu_{el}\left\|\vec{E_0}\right\|$. The laser light is split into a sample beam and a reference beam. The beam that is scattered by the nanoparticle displays

a *Doppler-shift* due to the nanoparticles' velocity:

$$\Delta\phi(t) = \int_0^t v(t')q\,dt' = \mu_{el}E_0q\frac{cos\left(\omega_e t\right)}{\omega_e} \tag{3.5}$$

where $q = k_f - k_i$ is the momentum transfer vector from light scattering. The reference beam is frequency modulated by ω_0, and this beam is combined with the signal beam to interfere with one another and produce a signal: $S(t) = Ae^{-i(\omega_0 t + \Delta\phi(t))}$. Multiplication of this signal with the reference signal $S_{ref}(t) = e^{-i\omega_0 t}$ leads straight to the Doppler shift $\Delta\phi(t)$, which through equation 3.5 leads to the electrophoretic mobility μ_{el}, and finally through equation 3.3 the zeta-potential, ζ, of the nanoparticles is obtained.

3.2 Sample Preparation

3.2.1 Growing Giant Unilamellar Vesicles

The size of giant unilamellar vesicles (GUVs) is of the same order as cells, enabling them to be directly observed in light microscopes. There are many methods described in literature for growing GUVs of sizes between 5 and $200\,\mu m$. Of these, the main methods are: *gentle hydration*[110], *solvent evaporation*[111] and *electroformation*[112,113]. In the gentle hydration method, lipid films are dried on a substrate and then exposed to an aqueous solution for up to 36 hours. This leads to vesicles of approximately $15\,\mu m$ diameter. The solvent evaporation method has the clear advantage of being able to form vesicles within a matter of minutes with diameters up to $50\,\mu m$. A clear disadvantage of both of these methods is the quality of the vesicles. They display a very high heterogeneity with respect to their size, shape, membrane thickness and internal structure[33]. The electroformation method, on the other hand, produces GUVs rather quickly (approx 3.5 hours) and homogeneously with a high degree of control on size. This was the reason for choosing to use the electroformation method for producing GUVs.

Originally, in 1986 Angelova et al. found that in the presence of a *direct current (DC)* field the gentle hydration method was improved significantly in terms of speed and

quality of GUVs produced. This method was improved even further in 1992 by using instead *alternating current (AC)* fields of small amplitudes (< 10 V) and frequencies (≤ 10 Hz). This method was used here and adapted slightly. We designed and built a chamber (Figure 3.2) similar to the one used by Bagatolli et al. al.[31]. The chamber is constructed out of *polytetrafluoroethylene (PTFE)* with nine separate compartments each 15 mm in diameter. Two platinum wires 0.5 mm in diameter are drawn through each of the three rows of three compartments and connected to an AC power supply. The wires are separated by a gap of 3 mm between each other and are positioned 2 mm above the floor of the compartment.
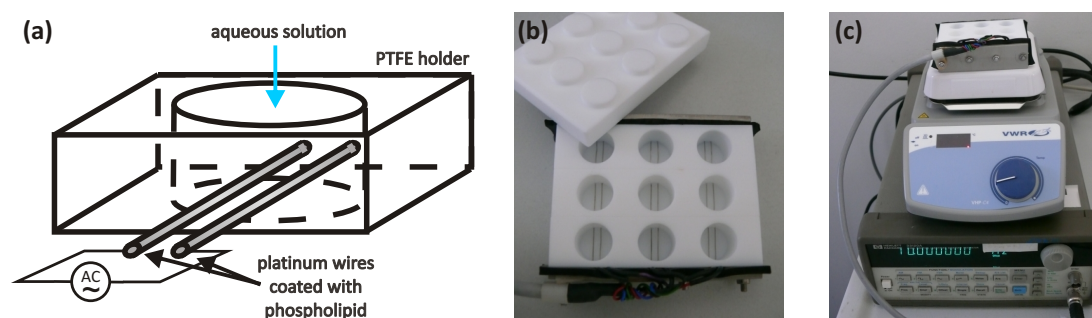
Figure 3.2 | Electroformation chamber for growing GUVs. (a) Diagram of a single compartment for growing GUVs. (b) Picture of the chamber and its lid, which seals off the compartments and prevents evaporation of the solution. (c) Picture of the entire growth setup with the chamber on top of the hot plate, which is on top of the signal generator supplying the AC field.

To produce the GUVs, the desired phospholipids are dissolved in chloroform for a concentration of 0.5 µg/µl. This solution is brought onto the platinum wires one drop at a time using a Hamilton syringe with a volume of 10 µl. The chloroform evaporates and the phospholipids form hundreds to thousands of bilayers on top of each other on the wires through self-aggregation. The thickness of this layer can be controlled by varying both the concentration of phospholipids in the solution and the total volume of applied solution. The gap between the platinum wires and the bottom of the compartments is very important.If the two parts were in direct contact, the phospholipid solution would spread along the PTFE chamber and not along the wires. After the chloroform is fully evaporated the chamber is filled with

an aqueous solution in which the GUVs are to be grown. Generally a solution of sucrose at 300 mM concentration was used. In the electroformation method, the phospholipid used must be in the fluid phase, otherwise the GUVs do not form. Therefore, depending on the phospholipid, the chamber must additionally be heated above the phospholipid melting temperature. This was done by sandwiching the chamber between two hot plates. It proved better for GUV growth during the experiments to heat up both the aqueous solution and the chamber to the desired temperature before filling the compartments and connecting the platinum wires to the AC power supply. Growth was usually conducted at a temperature of 75 °C. For the AC field, a modification of the Angelova protocol by Pott et. al[114] proved to be the most effective and was used here (table 3.1).
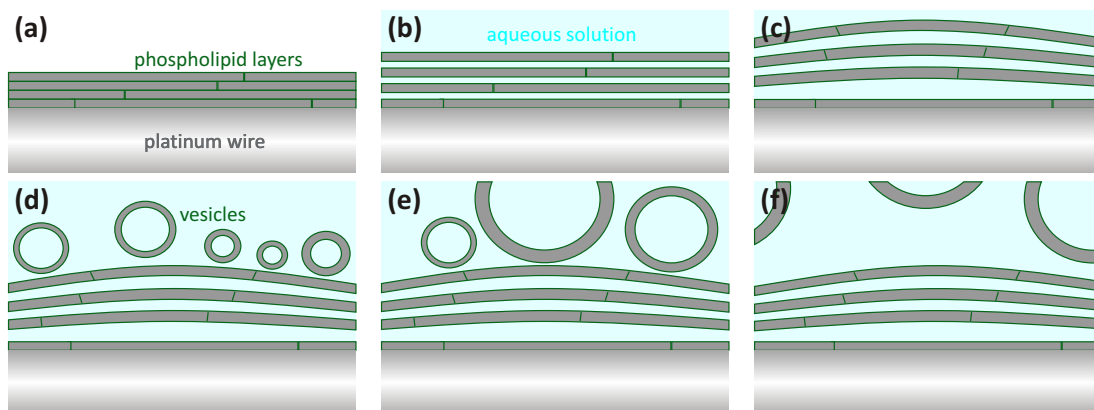
Figure 3.3 | Electroformation method for growing vesicles. (a) Dried phospholipids on the platinum wire, (b) bilayers become hydrated upon addition of water, (c) swelling begins with the presence of the AC field, (d) first small vesicles form and (e) later merge to form larger vesicles. (f) The GUVs are detached by lowering the frequency of the AC field.

The exact dynamics and forces of the formation process are still not fully understood[33] except for the general concept (Figure 3.3). The dried lipids form stacks of bilayer on top of the platinum wire (a). Upon addition of the aqueous solution the single bilayers become hydrated with water entering the gaps between the separate layers (b). The bilayers begin to swell as soon as the AC field is applied and more water enters in between the layers (c). Small vesicles begin to form, enclosing a portion of the aqueous solution (d). The vesicles become larger and

salinity	phase	field strength (V/m)	frequency (Hz)	time (min)
low (<10 mM)	preswelling	$50 \rightarrow 700$	10	60-90
	swelling	700	10	0-60
	detaching	700	$10 \rightarrow 4$	30-90
high (>10 mM)	preswelling	$50 \rightarrow 1300$	500	30
	swelling	1300	500	90
	deatching	1300	$500 \rightarrow 50$	30-60

Table 3.1 | Protocol for growing GUVs with the electroformation method for both low and high salinity, adapted from Pot el al.[114].

merge to form even larger vesicles (e). At the end of the process, the large vesicles are attached to the other bilayers on the platinum wire. To detach them, an AC field with a low frequency of only 4 Hz is applied to the wires (f). The full procedure takes approximately 3.5 hours, with three main phases during which the AC field is applied. In the first phase, the *preswelling phase*, the AC field strength is increased stepwise to the desired value at constant frequency. In the *main phase*, during which the GUVs grow to their full size, both field strength and frequency are kept constant. In the *detaching phase*, the frequency is reduced stepwise, which aids in removing the GUVs from the platinum wires. The values for frequency and field strength depend on the salinity of the desired solution. Here, low salinity (<10mM) and high salinity (>10mM) are distinguished. To control these values during growth we used a function generator (33120A, Hewlett Packard). After the growth process, the chamber is removed from the hot plate and allowed to cool down to room temperature. The solution is then extracted and stored in plastic containers because GUVs adsorb readily on glass surfaces. GUVs grown in sucrose solutions are stored at 4 °C to prevent the growth of bacteria in the solution.

For some experiments it can be quite practical to label the GUV membrane with a dye. The easiest way consists in adding a dye that is also soluble in chloroform to the phospholipid solution and growing these GUVs, as described above. Figure 3.4 shows several examples of GUVs grown during this thesis.
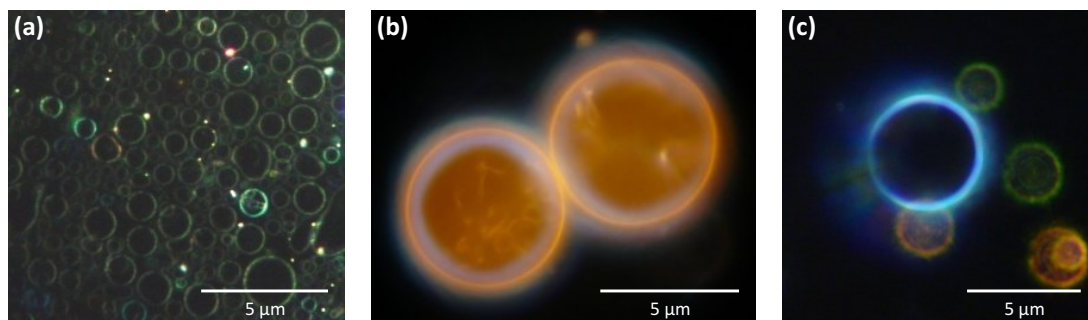
Figure 3.4 | Phospholipid vesicles grown via electroformation. (a) Vesicles viewed with dark field illumination, (b) stained with a Rhodamine dye and (c) stained with Laurdan dye.

3.2.2 Modifying the Surface of Gold Nanoparticles

The gold nanospheres used in this thesis were purchased from BBInternational. Exactly how they are produced and which molecules are present on the surface is not known. However, since the nanoparticles are mainly capped with citrate[115], it can be assumed that the procedure goes back to the method developed by Turkevich et al.[116]. In this method a boiling aqueous solution of gold salt ($HAuCl_4$) is combined with a reducing agent, in this case with citric acid. The acid not only reduces the gold ions but also serves as a stabilizing agent. The citrate ions bind lightly to the nanoparticle surface, giving it a negative surface charge and thereby preventing agglomeration of the nanoparticles (section 2.3). Because of the weak electrostatic binding between the citrate molecules and the gold nanoparticle surface, the citrate can easily be displaced by molecules that bind more tightly. In this thesis the citrate molecules were replaced with *cetyl trimethylammonium bromide (CTAB).* This molecule has a long aliphatic chain and a positively charged nitrogen atom at its head (Figure 3.5a). Normally, CTAB is used as a capping agent for the production of non-spherical gold nanoparticles[117], when it forms a bilayer around the gold nanoparticle[118] (Figure 3.5b). This bilayer must be highly interdigitated

because measurements of the thickness of the bilayers revealed values between 3 and $3.5\,\text{nm}$[119], whereas a fully extended CTAB molecule already has a length of $3\,\text{nm}$.

To replace the citrate ions with CTAB the as-received gold nanoparticles were diluted with deionized *(Milli-Q)* water and mixed with a $10\,\text{mM}$ solution of CTAB in a ratio of 5:10:1. This solution was shaken vigorously for one minute to enable the CTAB to cover all of the gold nanoparticles. Successful replacement was monitored by extinction spectrum and zeta potential measurements (Figure 3.5c). Due to the shift in surface charge, the extinction spectrum of gold nanoparticles shifts considerably to longer wavelengths and the zeta potential changes sign while maintaining more or less the same magnitude. This method is effective for gold nanoparticles with
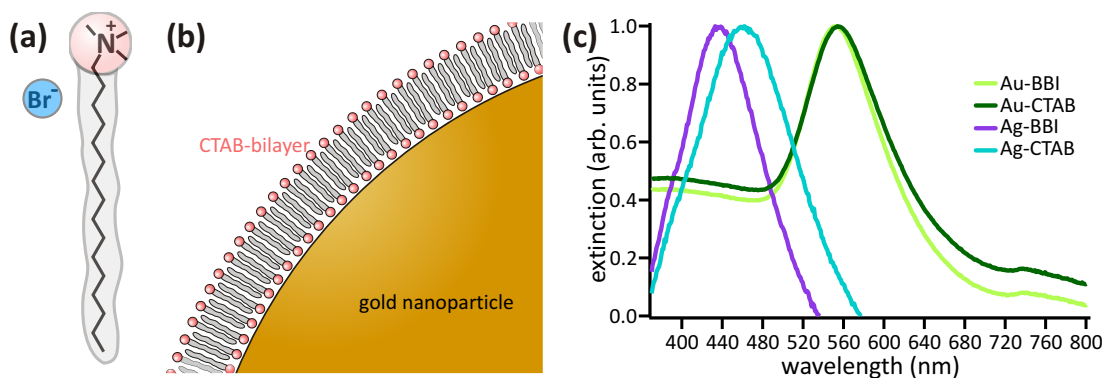
Figure 3.5 | CTAB on gold nanoparticles. (a) Chemical structure of a CTAB molecule. (b) Diagram of CTAB covering a gold nanoparticle. The CTAB forms an interdigitated bilayer approximately $3\,\text{nm}$ thick. (c) The extinction spectra of $80\,\text{nm}$ gold and silver nanoparticles show a pronounced redshift when coated with CTAB.

diameters larger than $40\,\text{nm}$. For smaller nanoparticles the ratio of the solution is changed to 2:4:1 (commercial gold nanoparticles : Milli-Q water : 10mM CTAB). The CTAB-stabilized gold nanoparticles are extremely stable and in contrast to citrate-stabilized nanoparticles, do not need to be kept at $4\,°\text{C}$. The gold nanoparticles also show a high stability when immersed in highly ionic solutions. The nanoparticles do not even aggregate in solutions of $150\,\text{mM}$ NaCl and $75\,\text{mM}$ KCl, implying that they should also be stable in common buffers with lower ionic strengths[120], such as *phosphate buffered saline (PBS)*.

3.2.3 Preparation of Glass Coverslips

The glass coverslips used in this thesis are 24x24 mm large and 0.19-0.23 mm thick and were purchased from Karl Hecht GmbH. In comparison with many other coverslips, they do not have a separating agent covering them. This agent can prevent the coverslips sticking together, but it also scatters light very strongly, which is very obstructive in dark field microscopy. To clean the coverslips they were first sonicated in *isopropyl alcohol* for 15 min and subsequently in Milli-Q water again for 15 min. Finally the coverslips were blown dry by a nitrogen gun and stored in wafer holders.

For some of the measurements it was necessary to coat the coverslips with one or several layers of a polyelectrolyte. We used the following established method[121]: The cleaned substrates are immersed for 30 min in a solution of *polydiallyldimethyl-ammonium chloride (PDADMAC, molecular weight, MW $\approx 400,000 - 500,000$)* at 2 mg/ml in a 0.5 M solution of sodium chloride (NaCl). The coverslip is then rinsed in Milli-Q water and dried again by a nitrogen gun. Because the polyelectrolyte has a positive charge, it binds to the surface of the glass, forming a layer $1 - 2$ nm thick. The coverslip can then be immersed, again for 30 min, in a solution of *sodium polystyrene sulfonate (PSS,* MW = 70 000) also at 2 mg/ml in a 0.5 M solution of NaCl. The coverslip is then cleaned as described before. PSS is a negatively charged polyelectrolyte and thus forms a layer, $1 - 2$ nm thick on top of the PDADMAC layer. These steps can be repeated many times, with alternating PDADMAC and PSS layers.

4 Laser Printing of Gold Nanoparticles

Electronic device structures have become rapidly smaller during the last few decades but are slowly reaching a critical limit. Thus, in the last several years extensive research has been directed towards developing and implementing new approaches for fabricating increasingly smaller features with high-yields and minimal defects, while maintaining cost-effectiveness[122]. The approach of aligning single nanoparticles into large-scale arbitrary patterns has recently come into focus[29]. Colloidal nanoparticles, which can already be produced by high through-put robotized methods[123,124], have certain unique properties due to their small sizes and materials. These properties can be custom tailored, holding great promise for future applications. Before nanoscale devices, capitalizing on the nanoparticle properties, can be fabricated, a way must be found to transfer these nanoparticles onto substrates without complications, where they can be integrated with other nanoparticles, waveguides or electrodes with a precision of only a few nanometers. Attempts to tackle this have resulted recently in several lithographical methods, typically involving multiple steps for chemical patterning of the substrate surfaces[122,125,126] but rarely providing the capability of single nanoparticle accuracy[29,127,128]. The approach presented in this chapter is based on a completely different physical technique, promising to overcome the challenges and problems of other methods. This new technique employs optical forces exerted on a nanoparticle by a laser. These are used to print individual nanoparticles onto substrates with a precision of a few tens of nanometers only. The method can be applied to virtually any type of nanoparticle, using optical forces to manipulate the nanoparticles and van der Waals forces to bind them.

4.1 Method: Principles and Calculations

As mentioned in section 2.2, the optical forces acting on dielectric colloidal particles in a tightly-focused laser beam have attracted enormous attention since Ashkin and coworkers' pioneering work[129], due to their relevance for optical trapping or *tweezing*. Optical forces on metallic NPs have been investigated for trapping, both at wavelengths far from[130,131] and, more recently, near the plasmon resonances where one has the advantage of an enhanced interaction with light[132-134]. For the work described in this section, we do not use the optical forces to trap nanoparticles but rather to guide them to a specific location and print them on a substrate.
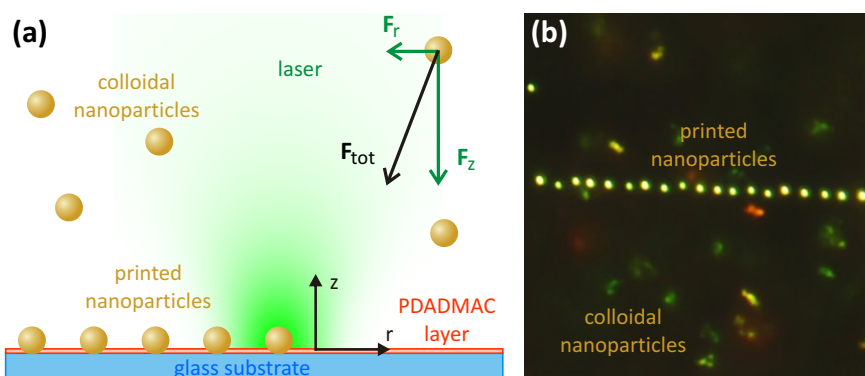
Figure 4.1 | Laser printing of single gold nanoparticles. (a) Scheme of the printing process. Gold nanoparticles are printed on the surface, using optical forces generated by a laser. (b) Dark field image of a row of printed gold nanoparticles. The green color shows that the particles are actually single spherical nanoparticles. Colloidal nanoparticles can be seen diffusing in the background.

To demonstrate the method, we use spherical gold nanoparticles with a diameter of $80\,\text{nm}$. These are stabilized by a CTAB-bilayer, as described in section 3.2.2. A $200\,\mu\text{l}$ drop is brought onto a glass coverslip and the latter is placed into the dark-field microscope. Since the gold nanoparticles have a positive surface charge and a cleaned glass coverslip in water has a negative surface charge, the nanoparticles adhere readily to the glass surface. To ensure that this does not happen, the glass coverslips are coated with a layer of PDADMAC, as explained in section 3.2.3. Due to this modification the gold nanoparticles do not bind spontaneously to the surface of the glass for the duration of the experiments (at least 5 hours). A laser beam

(Millennia V, Spectra Physics) with a wavelength of $532\,\text{nm}$ is focused onto the glass surface with a spot size of approximately $380\,\text{nm}$ (FWHM). We chose this laser wavelength, because we wanted to exploit the strong forces acting on the nanoparticle in a laser beam with a wavelength near the plasmon resonance. The gold nanoparticles diffuse through the solution. If they come close enough to the laser beam, they are propelled towards the glass surface. For low laser powers, they do not bind to the surface and continue diffusing through the solution. Increasing the laser power above a certain threshold, a nanoparticle accelerated by the laser can bind to the surface of the glass coverslip at the position the laser is focused on. Leaving the laser spot in the same place as the printed particle does not lead to any further printing events. Only one single gold nanoparticle is printed at the focal point of the laser. If the laser is moved to a new position, another nanoparticle will adhere to the glass surface after a period of time, again at the focal point of the laser. This printing can be repeated indefinitely (Figure 4.1). Because the process is monitored in real time, single nanoparticles can be printed at specific locations to form any desired pattern (Figure 4.2). The laser is turned off while the position is being changed and switched on to print a nanoparticle at the new position.
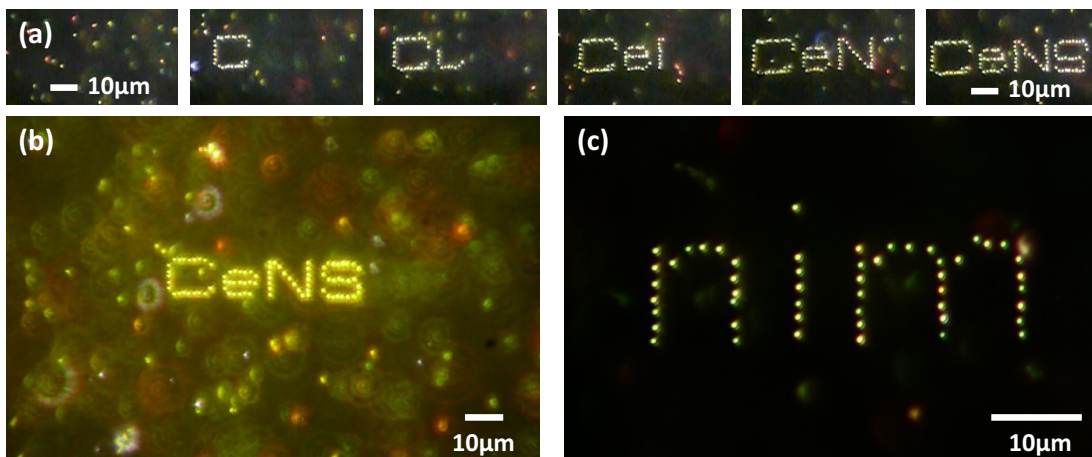
Figure 4.2 | Deliberate patterns of single gold nanoparticles printed on a glass coverslip. (a) Dark field images of a patterning sequence. The gold nanoparticles are printed one at a time, switching the laser off after a printing event and subsequently relocating the laser to the position for the next nanoparticle. (b, c) Large scale image of a printed pattern showing gold nanoparticles diffusing through the solution.

The DLVO deals with the stability of colloidal solutions and helps to explain the immobilization on the substrate described above (section 2.3). In the classical DLVO theory there is a certain balance between the attractive Lifschitz-van der Waals forces and the repulsive electrostatic forces. The resulting interaction energies between a sphere with radius r and a semi-infinite plate at a distance z are given by [135]:

$$E_{LvdW}(z) = -\frac{A}{6}\left[\frac{r}{z} + \frac{r}{z+2r} + ln\left(\frac{z}{z+2r}\right)\right] \tag{4.1}$$

$$E_{Elec}(z) = \pi\varepsilon r(\zeta_{np}^2 + \zeta_{su}^2)\left[\frac{2\zeta_{np}\zeta_{su}}{\zeta_{np}^2 + \zeta_{su}^2}ln\left(\frac{1+e^{-\kappa z}}{1-e^{-\kappa z}}\right) + ln\left\{1-e^{-2\kappa z}\right\}\right] \tag{4.2}$$

with the zeta potentials of the sphere, ζ_{np}, and of the surface, ζ_{su}, the Hamaker constant, A, the medium permittivity, ε, and the thickness of the electric double layer, κ^{-1}. Differentiating with respect to distance z leads to the forces acting on the nanoparticle:

$$F_{LvdW}(z) = \frac{2Ar^3}{3z^2(z+2r)^2} \tag{4.3}$$

$$F_{Elec}(z) = \pi\varepsilon r\kappa\left(\zeta_{np}^2 + \zeta_{su}^2 - 2\zeta_{np}\zeta_{su}e^{\kappa z}\right)(cot(z\kappa) - 1) \tag{4.4}$$

The calculation of the forces requires knowledge of the zeta potentials of both the gold nanoparticles and the silica surface, the thickness of the double-layer and the Hamaker constant of the system. The zeta potential of the gold was measured experimentally and has a value of approximately $40\,$meV. The value of the silica zeta potential is taken from literature, where a value is given around $35\,$meV for the prevalent conditions in our experiments [136]. Determining values for the Hamaker constant is more tricky. Because we have a system with coating layers, theoretically one would have to also take into account the Hamaker constants of these layers. However, as explained in section 2.3, the Hamaker constants of the coatings only become important at very small distances. The contribution to the effective Hamaker constant is in fact so small that even up to $1\,$nm the Hamaker constant is still dominated by the contribution of the gold-silica interaction. At this point short range steric forces offset the van der Waals forces, which means the effect of the CTAB coating can be disregarded without much error [137]. Values for the Hamaker constant, A_{gws}, for the gold-water-silica system are calculated using the values for the pure materials interacting across a vacuum [138]: $A_{gg} = 40 \times 10^{-20}$J,

$A_{ww} = 4.0 \times 10^{-20}$J, $A_{ss} = 6.6 \times 10^{-20}$J and inserting these into formula 2.40. This leads to an effective Hamaker constant of $A_{gws} = 2.46 \times 10^{-20}$J. The thickness of the double-layer (*Debye length*) is given by:

$$\kappa^{-1} = \left(\frac{2000F^2}{\varepsilon_0 \varepsilon_r RT}I\right)^{-1/2} \tag{4.5}$$

with the Faraday constant F and the ionic strength of the solution $I = 1/2\sum(c_i z_i^2)$, which is strongly dependent on the ions present in the colloidal solution. For room temperature ($T = 25\,°C$) this equation simplifies to: $\kappa = 3.288\sqrt{I}$. The actual composition of the commercially available gold colloid solution is unknown, and consequently also the ionic strength I of this solution. We estimate a $1\,mM$ concentration of ions in the solution. We use this value to calculate the forces present in the system (Figure 4.3a).
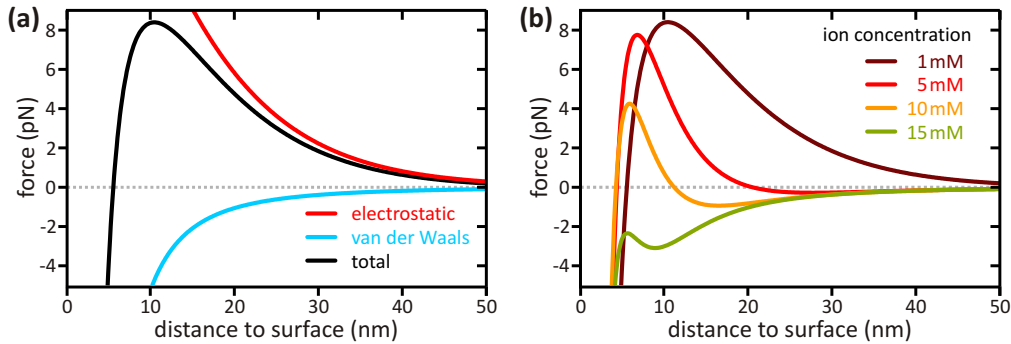
Figure 4.3 | Forces between a gold nanoparticle and a glass surface according to DLVO-theory. (a) Electrostatic, van der Waals and total forces between an $80\,nm$ large gold nanoparticle and a glass surface. If the nanoparticle comes close enough to the surface, the van der Waals forces become strong enough to bind the nanoparticle. (b) Effect of increasing ionic strength of the solution on the total force. For a large enough ionic concentration a second minimum develops further away from the surface. For even higher concentrations the nanoparticles bind directly to the surface.

For this case the electrostatic repulsion is the dominant force down to a distance of a few nanometers. This prevents the nanoparticles from binding to the glass surface, as was seen in the measurements. However, these calculations are very sensitive to small changes in the parameters. Small increases in the ionic strength

can alter the force profile significantly (Figure 4.3b). The lowest concentration, $1\,\mathrm{mM}$, is the same as used for the calculations for Figure 4.3a. At $5\,\mathrm{mM}$ there is already a pronounced second minimum from $30\,\mathrm{nm}$ outwards and for a value of only $20\,\mathrm{mM}$, the electrostatic repulsion can no longer screen the van der Waals forces and the nanoparticles bind spontaneously to the glass surface. This was confirmed experimentally. By adding NaCl to the gold nanoparticle solution (concentration $15\,\mathrm{mM}$), the nanoparticles bind to the surface readily, in stark contrast to the previous situation, when the nanoparticles would not bind at all. Thus, it is possible to qualitatively explain what is happening, but it is very difficult to actually present concrete values for the forces.

In the experiments where the nanoparticles were printed onto the surface of the glass, the nanoparticles must be pushed by enough force to overcome the repulsive forces of the electrostatic double layers. It is therefore necessary to look at the actual forces applied to the nanoparticle by the laser beam. The basis for the calculations is the non-relativistic Lorentz force, which leads to the time-averaged gradient and scattering forces:

$$\left\langle \vec{F}_g \right\rangle = \frac{\varepsilon_0}{2}\mathsf{Re}\left(\hat{x}_j \alpha' E_k^* \frac{\partial E_k}{\partial x_j} \right) = \frac{\varepsilon_0}{4}\left[\hat{x}_j \frac{\partial}{\partial x_j}(E_k^* \alpha' E_k) \right] \tag{4.6a}$$

$$\left\langle \vec{F}_s \right\rangle = \frac{\varepsilon_0}{2}\mathsf{Re}\left(-i\hat{x}_j \alpha'' E_k^* \frac{\partial E_k}{\partial x_j} \right) = \frac{\varepsilon_0}{2}\mathsf{Im}\left[\hat{x}_j E_k^* \alpha'' \left(\frac{\partial E_k}{\partial x_j} \right) \right] \tag{4.6b}$$

with the real and imaginary parts of the polarizability, α' and α'', the Cartesian-coordinate unit vectors, $\hat{x}_j$, and the components of the electric field amplitude, E_k. Re and Im are the real and imaginary part of the expression in the following bracket. The spatial distribution of the electric field in our setup is given by a paraxial Gaussian beam focused by a lens. However, this approximation is only valid for small focusing and breaks down for *numerical aperture* (*NA*) values that are too large. Thus, an error is expected for the values of the electric field depending on the NA of the system[139]. In the Gaussian approximation, the electric field at a distance z along the beam and a radial position r from the beam axis is given by:

$$\vec{E}(r) = \vec{E}_0 \sqrt{\frac{2}{\pi}} \frac{\omega_0}{\omega(z)} exp(-r^2/\omega^2(z)) exp\left(i\frac{k_m r^2}{2R(z)} \right) exp\left(ik_m z + i\eta(z) \right) \tag{4.7}$$

with the reduced functions:

$$\omega^2(z) = \omega_0^2 \left[1 + \left(\frac{z}{z_0} \right)^2 \right] \tag{4.8a}$$

$$R(z) = z \left[1 + \left(\frac{z_0}{z} \right)^2 \right] \tag{4.8b}$$

$$\eta(z) = tan^{-1} \left(\frac{z}{z_0} \right) \tag{4.8c}$$

Here $z_0 = \pi \omega_0^2 / \lambda_m$ and $k_m = 2\pi / \lambda_m$ with the beam radius in the focal plane ω_0, and the medium wavelength of light λ_m. After a coordinate transformation the equation for the electric field amplitude is inserted into equations 4.6a and 4.6b. This results in the gradient and scattering forces in radial and axial direction [140]:

$$\left\langle \vec{F}_{g,z} \right\rangle = - \frac{\varepsilon_0}{\pi} \alpha' \left| E_0^2 \right| z \frac{\omega_0^4}{z_0^2} \left[\frac{1}{\omega^4(z)} - \frac{2r^3}{\omega^6(z)} \right] exp \left[- \frac{2r^2}{\omega^2(z)} \right] \tag{4.9a}$$

$$\left\langle \vec{F}_{g,r} \right\rangle = - \frac{2\varepsilon_0}{\pi} \alpha' \left| E_0^2 \right| r \frac{\omega_0^2}{\omega^4(z)} exp \left[- \frac{2r^2}{\omega^2(z)} \right] \tag{4.9b}$$

$$\left\langle \vec{F}_{s,z} \right\rangle = + \frac{\varepsilon_0}{\pi} \alpha'' \left| E_0^2 \right| \frac{\omega_0^2}{\omega^2(z)} \left\{ k_m \left[1 - \frac{r^2}{2} \frac{(z^2 - z_0^2)}{(z^2 + z_0^2)^2} \right] + \frac{\omega_0^2}{z_0 \omega^2(z)} \right\}$$
$$\times exp \left[- \frac{2r^2}{\omega^2(z)} \right] \tag{4.9c}$$

$$\left\langle \vec{F}_{s,r} \right\rangle = + \frac{\varepsilon_0}{\pi} \alpha'' \left| E_0^2 \right| \frac{\omega_0^2}{\omega^2(z)} \frac{k_m r}{R(z)} exp \left[- \frac{2r^2}{\omega^2(z)} \right] \tag{4.9d}$$

These forces can be plotted to find their magnitude and direction and, thus, their effect on the nanoparticles inside the laser beam. The axial force is always directed along the beam path, with its intensity maximum slightly behind the focal plane and in the center of the beam (Figure 4.4). For the settings chosen here, the laser exerts a maximum force of approximately $15\,\mathrm{pN}$ on an $80\,\mathrm{nm}$ gold nanoparticle. The spatial distribution of the radial force is slightly more complicated than the axial force (Figure 4.5). Approaching from negative z-values, the radial force is directed towards the center of the beam, reaching a maximum of $4\,\mathrm{pN}$ approximately $50\,\mathrm{nm}$ in front of the focal plane and at a radial position of $90\,\mathrm{nm}$. The radial force remains directed towards the beam axis up until a position of approximately $150\,\mathrm{nm}$ behind
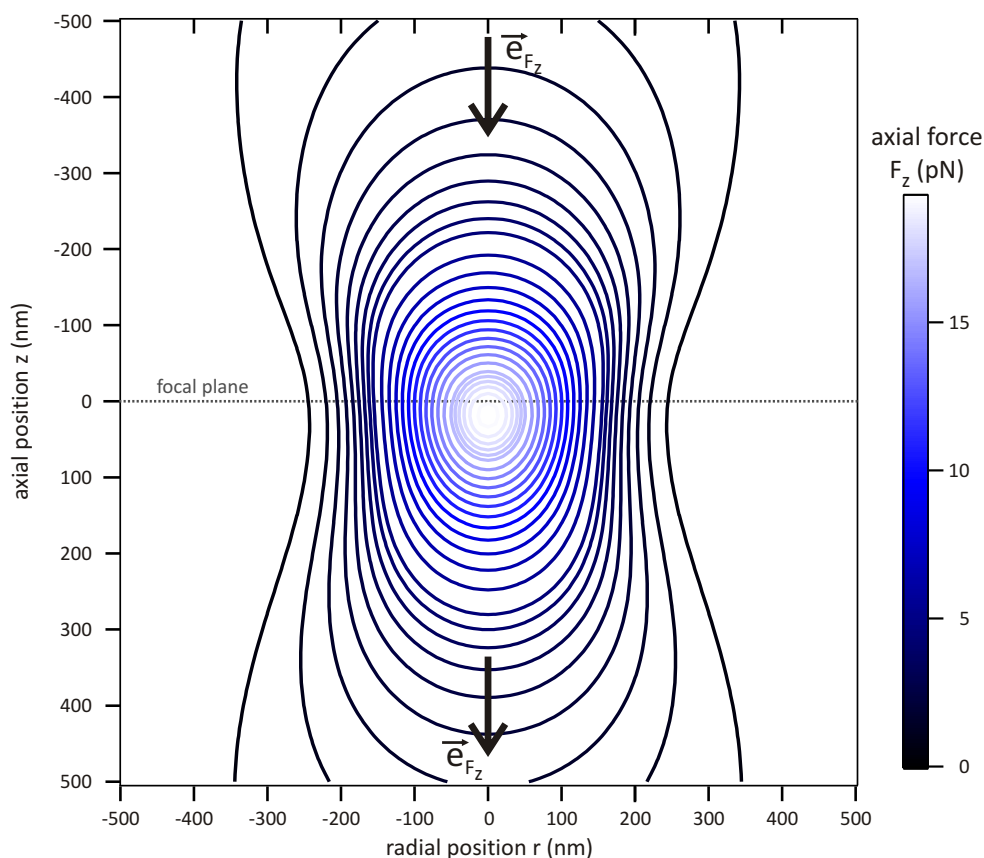
Figure 4.4 | Calculated axial force exerted on a gold nanoparticle by a laser beam. The calculations used an $80\,\mathrm{nm}$ gold nanoparticle illuminated by a Gaussian-shaped laser beam of wavelength $532\,\mathrm{nm}$ focused to a spot size of $380\,\mathrm{nm}$ (FWHM) with a laser power of $10\,\mathrm{mW}$ on the sample. The arrows indicate the direction of the axial force, which is always in the same direction as the light propagation.

the focal plane, where the force reaches a value of 0. Further behind the focal plane the radial force faces outwards away from the beam center. It reaches a maximum of $-0.4\,\mathrm{pN}$ at a position of approximately $280\,\mathrm{nm}$ behind the focal plane and a radial position of $150\,\mathrm{nm}$. The reason for this anomalous behavior is the beam focusing. Because the rays from the collimated laser beam are focused inwards down to the focal plane and outwards behind it, the scattering force is also directed towards the beam axis in front of the focal plane and away from the beam center behind the focal plane. The gradient force is always directed towards the beam center.
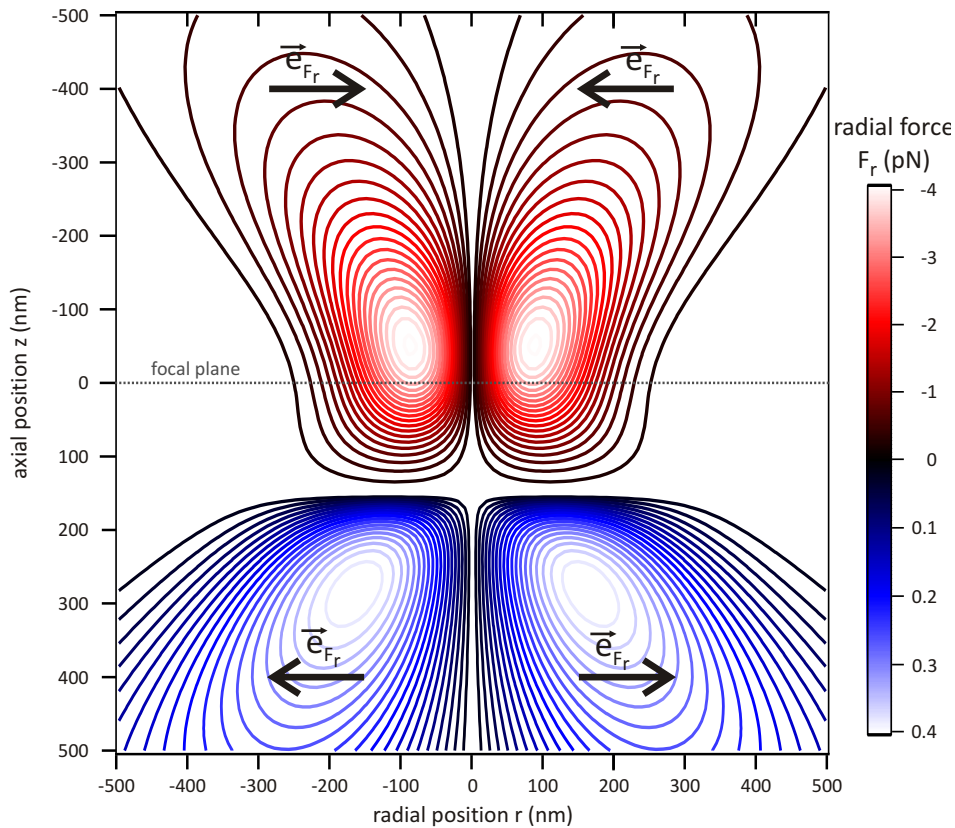
Figure 4.5 | Calculated radial force imposed on a gold nanoparticle by a laser beam. The calculations involved an $80\,\text{nm}$ gold nanoparticle illuminated by a Gaussian-shaped laser beam of wavelength $532\,\text{nm}$ focused to a spot size of $380\,\text{nm}$ (FWHM) with a laser power of $10\,\text{mW}$ on the sample. The arrows indicate the direction of the radial force, which is directed towards the beam center in front of the focal plane and also up to $150\,\text{nm}$ behind it. Further away the radial force changes sign and is directed outwards, away from the beam center.

With this information one can explain how the laser forces act on the gold nanoparticles. Once a gold nanoparticle comes close enough to the laser beam, it is pushed downwards towards the substrate while at the same time it is drawn towards the beam center. The volume within which this occurs is given by the magnitude of the forces, which must overcome the thermally activated diffusion of the nanoparticles in solution. Increasing the laser power leads to a larger volume, from which the nanoparticles can be collected and printed onto the surface. At the same time, however, because of the higher axial force, a nanoparticle will require less time to reach the surface of the glass coverslip and, thus, the radial force has less

61

time to guide the nanoparticle towards the beam center. As previously explained, calculating exact values for the forces present in the system is quite difficult and highly prone to errors. Consequently, it is not easy to exactly predict the laser power necessary to overcome the electrostatic forces and print the nanoparticles on the glass surface. We can, however, provide an educated estimate. Using the values of the electrostatic, Lifschitz-van der Waals and optical forces as detailed above, we estimate a required printing power of $10\,\mathrm{mW}$ for our laser at a wavelength of $532\,\mathrm{nm}$, focused to a spot size of $380\,\mathrm{nm}$ FWHM. Although we can expect significant deviations from this value in the experiments, it serves nevertheless as a reasonable guideline.

We conducted several experiments exploring the stability of the printed nanostructures. The glass coverslips with the printed gold nanoparticle structures showed no signs of degradation, when rinsed with different solvents, e.g. water and isopropyl alcohol. Even the use of a nitrogen gun and water to create a high-pressure cleaner did not detach the printed nanoparticles from the surface. The glass coverslip was taken out of the setup and brought to a different setup with an incorporated atomic force microscope. Here, we measured the pattern and found the printed nanoparticles remained in their printing positions. Another test was done to let the remaining nanoparticle solution dry, so that the other nanoparticles could precipitate onto the polyelectrolyte. This led to a widespread covering of the surface with nanoparticles. Adding water after this and rinsing the sample, however, removed all of the nanoparticles that were not printed and left those that were printed still tightly bound to the glass coverslip. One such printed structure was again inspected after 3 days, still showing no change. This printing method thus proves to be very stable, a necessity for large-scale applications.

4.2 Accuracy and Influence of Printing Parameters

With the knowledge of how the printing process works and of the forces acting upon the nanoparticle in solution, experiments can be conducted to find out exactly how diverse factors affect the printing method. The most important parameter is the laser power, as it can directly determine whether a nanoparticle is printed

or not. To study the effect of the laser power, we used the same parameters as before: $80\,\text{nm}$ gold nanoparticles coated with CTAB on a glass coverslip coated with PDADMAC and the same laser parameters (beam size $380\,\text{nm}$ (FWHM) at a wavelength of $532\,\text{nm}$). The minimum power at which printing was achieved was $P_{min} = 175\,\mu\text{W}$, this corresponds to a laser power density on the nanoparticle of $15.8\,\text{kW/cm}^2$. To determine the value of the minimum power, the laser power was gradually reduced until a printing event was no longer witnessed even after waiting for $30\,\text{min}$. Using the laser power density, we calculate the maximum force in axial direction imposing on the nanoparticles to $51\,\text{fN}$. The experimentally obtained printing power threshold is far below the expected value of $10\,\text{mW}$. Exactly why this power is so low is not clear, but experiments conducted later with non-resonant lasers, provide more insight. The power was then increased to a value ($P = 294\,\mu\text{W}$), at which a printing event occurred every five seconds and a row of nanoparticles was printed, shifting the laser beam by a constant value between each event (Figure 4.6a). An image of the nanoparticles was taken with a digital camera, and the positions of
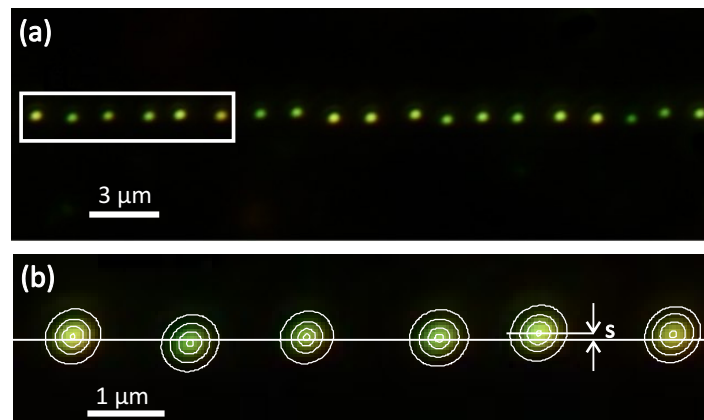
Figure 4.6 | Accuracy of the printing process. (a) The nanoparticles are printed in a row by moving the laser laterally by a constant value between each event. (b) The accuracy is determined by locating the position of the nanoparticles with two-dimensional Gaussian fits and measuring the deviation to the line along which the laser was moved.

the gold nanoparticle were determined by fitting a two-dimensional Gaussian to each spot. The accuracy of the printing process was determined by calculating the average displacement, s, of the nanoparticles perpendicular to the line along which the nanoparticles were to be printed (Figure 4.6b). The variations in the inter-

particle distance were larger and are explained by the fact that the piezo-stages were not closed-loop stages. Thus, the distance moved between each step had a certain amount of variation, masking the printing accuracy. For this reason, we could not use the inter-particle distance as a measure of printing accuracy. Several rows were printed for different laser powers to determine the effect of the laser power on the printing accuracy.
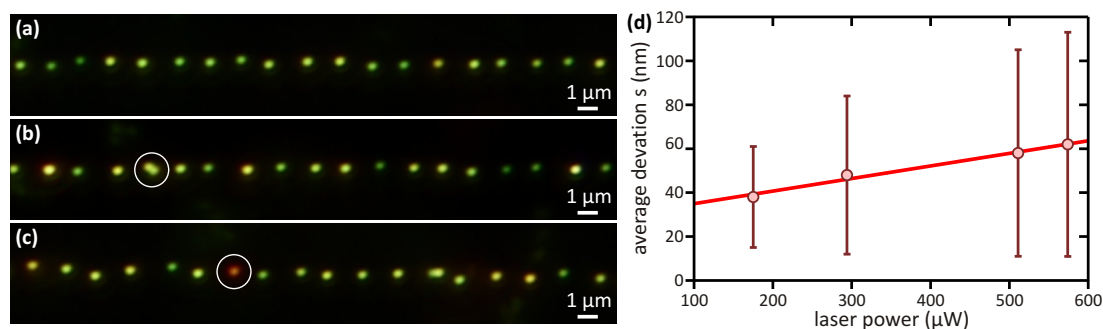
Figure 4.7 | Effect of the laser power on the accuracy of the printing process. (a) The highest accuracy is achieved with the lowest laser power ($P = 175\,\mu\text{W}$). (d) The average deviation s from the line along which the laser is displaced increases linearly with laser power (d). For higher powers ($P > 574\,\mu\text{W}$) two additional effects appear: (circle, b) printing of single particles in close proximity to each other and (circle, c) the printing of single, non-spherical nanoparticles or small aggregates of nanoparticles ($P > 738\,\mu\text{W}$).

At the lowest power ($P_{min} = 175\,\mu\text{W}$) the highest accuracy was achieved, with an average deviation from the printing axis of only $s = 38\,\text{nm}$. Increasing the power decreased the precision. At the laser power value $P = 294\,\mu\text{W}$, which enabled a printing event every $5\,\text{sec}$, we obtained an accuracy of $48\,\text{nm}$. The average deviation of the nanoparticles more than doubled from $58\,\text{nm}$ to $123\,\text{nm}$ for an increase in the laser power of less than 45% ($511\,\mu\text{W}$ to $738\,\mu\text{W}$) (Figure 4.7a-c). There are three reasons for this effect. Firstly, as stated before, there is a power threshold above which the optical forces are strong enough to overcome the barrier presented by the electrostatic barrier and print a nanoparticle. Increasing the laser power enlarges the area on the substrate around the beam center in which the optical forces are strong enough to accomplish printing. Secondly, at higher laser powers the nanoparticles absorb more energy and are consequently heated more. This leads to a faster diffusion, which acts against the radial force guiding the nanoparticles

towards the beam axis. Finally, as already stated, the stronger axial force propells the nanoparticles more rapidly towards the substrate, reducing the time during which the weaker radial forces can guide the nanoparticles towards the potential minimum at the beam center. However, even though using the minimum laser power needed to overcome the electrostatic barrier leads to a higher precision, it is accompanied by a reduced capture volume for the nanoparticles and thus an increased time between printing events. Thus speed is traded against precision such that a compromise has to be found . We chose a laser power that resulted in an average devitation of only $58\,\mathrm{nm}$ while simultaneously reducing the time between printing events to no more than $5\,\mathrm{s}$.

The gold nanoparticles have a large absorption cross section, as explained before. Thus, the nanoparticle temperature may also play a role in the printing process. To study this, we calculated the temperatures of the illuminated gold nanoparticles. For an initial temperature of $20\,^\circ\mathrm{C}$ the gold nanoparticles were heated up to only $25\,^\circ\mathrm{C}$ at the lowest laser power $P = 175\,\mathrm{\mu W}$. At the laser power enabling a printing event every five seconds ($P = 294\,\mathrm{\mu W}$) the nanoparticles reached a temperature of $T = 28.4\,^\circ\mathrm{C}$ and for the highest power used to measure the accuracy the temperature reached was only $T = 41\,^\circ\mathrm{C}$. These temperatures were quite low, and neither change the viscosity of water considerably nor do they lead to much convection in the solution. We can thus neglect the temperature influence in the experiments.

At higher powers ($P > 570\,\mathrm{\mu W}$) two other effects became noticeable. Firstly, occasionally two or more nanoparticles were printed in close proximity to each other (circle; Figure 4.7b). This did not happen for lower laser powers and most probably occurs because the substrate area, in which the optical forces are strong enough to enable printing, becomes large enough for the printing of several nanoparticles to occur. For even higher powers ($P > 735\,\mathrm{\mu W}$), occasionally non-spherical particles were also printed (circle; Figure 4.7c). These particles, which could be distinguished by their non-green color in dark field images, were probably elongated single nanoparticles, dimers or small aggregates of spherical gold nanoparticles. At lower laser powers no printing of such nanoparticles was observed. These effects could

be useful when printing more complex structures, such as rows of plasmonically coupling nanoparticles, but they must be avoided when creating patterns out of single, spherical nanoparticles.

The next factor effecting the laser printing is the wavelength of the laser beam itself. While in the first series of experiments the laser was more or less tuned to the plasmon resonance of the gold nanoparticles, for the next set of experiments it was detuned and the measurements were repeated. For this we used the Tsunami laser, which, running in cw-mode, could be set to emit between around $700\,\text{nm}$ and $900\,\text{nm}$. Printing was achieved at all wavelengths between the boundary values. The laser power necessary for printing increased for longer wavelengths. However, the laser power is not a useful quantity for comparison, as for longer wavelengths the absorption and scattering cross sections are greatly reduced for the gold nanoparticles (Figure 4.8a). This means that for longer wavelengths the laser
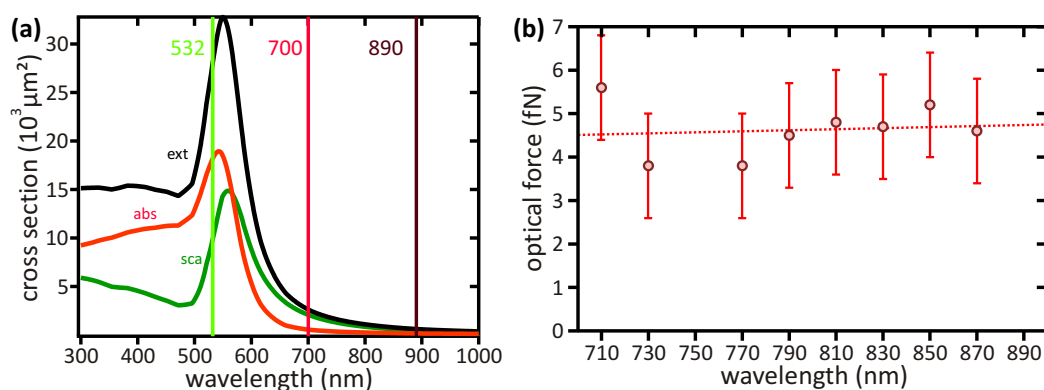
Figure 4.8 | Effect of using a non-resonant wavelength on the accuracy of the printing process. (a) Cross sections of an $80\,\text{nm}$ gold nanoparticle. Printing was achieved at $532\,\text{nm}$ and between $700\,\text{nm}$ and $890\,\text{nm}$. (b) The minimum force necessary to print the nanoparticles off resonance is an order of magnitude lower than for the resonant laser, but between $700\,\text{nm}$ and $890\,\text{nm}$ more or less constant.

power must be higher to induce the same force on the nanoparticles. Therefore, we calculated the total optical force exerted on the nanoparticles in axial direction and obtained values for the minimum optical force necessary to accomplish printing for each wavelength (Figure 4.8b). The results show that between $700\,\text{nm}$ and $890\,\text{nm}$ the force necessary to achieve is constant around $5\,\text{fN}$. The linear regression from

the graph has a slope of $0.0012 \pm 0.0044\,\text{fN/nm}$, so with a probability $p > 0.05$ is not different from 0, i.e. constant. The minimum value of the optical force at which printing was achieved for non-resonant wavelengths was approximately only one tenth of the value for the resonant wavelength ($F = 51\,\text{fN}$). This discrepancy can be explained when inspecting the laser forces acting on the gold nanoparticles for both resonant and non-resonant wavelengths. For this we calculated the optical force profile for a laser wavelength of $800\,\text{nm}$ (Figure 4.9) and compared it with the force profile at $532\,\text{nm}$ (Figure 4.4 and Figure 4.5). The calculations were set, so that in both cases the maximum force in axial direction was the same. The distinct difference for the two wavelengths lies in the radial force, which is more than ten times stronger for the $800\,\text{nm}$ laser. This leads to a much stronger trapping of the nanoparticles and thus a larger capture volume. To compare the capture volumes at different wavelengths, we took the minimum laser power at which printing was achieved for three different wavelengths and calculated the optical forces. We then took an value of $3\,\text{fN}$, and compared the volumes in which the radial force is larger than this value (Figure 4.10). Clearly the capture volume is much larger at $720\,\text{nm}$ than at $532\,\text{nm}$ and slightly larger still at $890\,\text{nm}$. This means that the time between
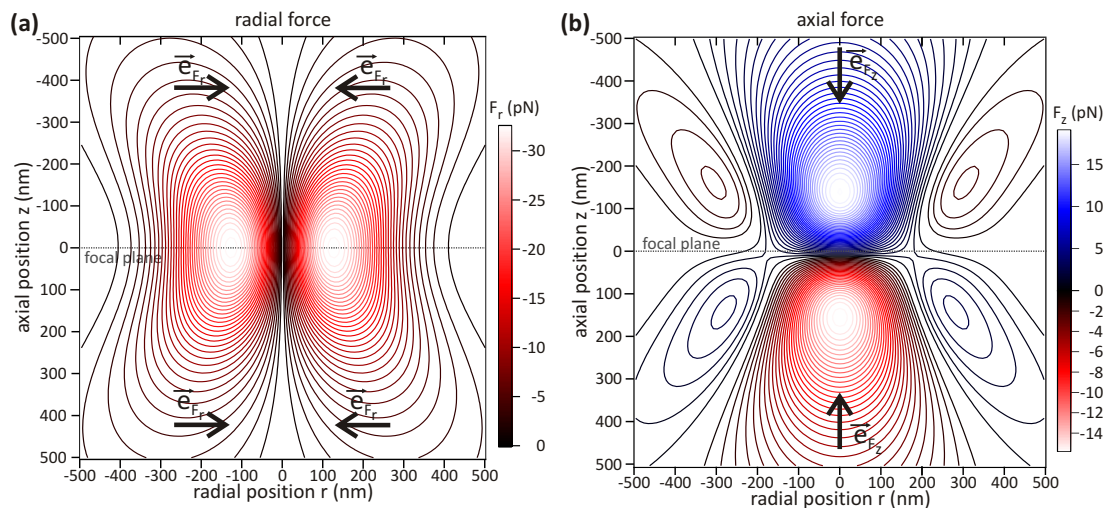
Figure 4.9 | Optical forces on an $80\,\text{nm}$ **nanoparticle exerted by a laser at** $800\,\text{nm}$ **wavelength.** For this simulation, the laser power is chosen so that the maximum axial force is the same as for the printing conditions at $532\,\text{nm}$ wavelength. (a) The radial force in this case is purely attractive and is also stronger than the axial force (b), which is repulsive in front of the focal plane and attractive behind it.

printing events is greatly reduced for the resonant laser. The minimum force with which printing was achieved was constant between $720\,\mathrm{nm}$ and $890\,\mathrm{nm}$ but much larger at $532\,\mathrm{nm}$. It can be thus concluded that the minimum force necessary for printing is the minimum force at which non-resonant printing was achieved ($5\,\mathrm{fN}$).

At resonant wavelengths, the capture volume becomes so small for laser powers inducing less than $51\,\mathrm{fN}$ axial force on the nanoparticle that the time between printing events greatly exceeds the observation times of up to $30\,\mathrm{min}$. These results suggest that using a non-resonant wavelength for printing could be even more effective than resonant printing. However, we observed that the accuracy at non-resonant wavelengths was worse than when using the laser at $532\,\mathrm{nm}$ (Figure 4.11). The lowest deviation s that could be achieved was $143\,\mathrm{nm}$ (Fig-
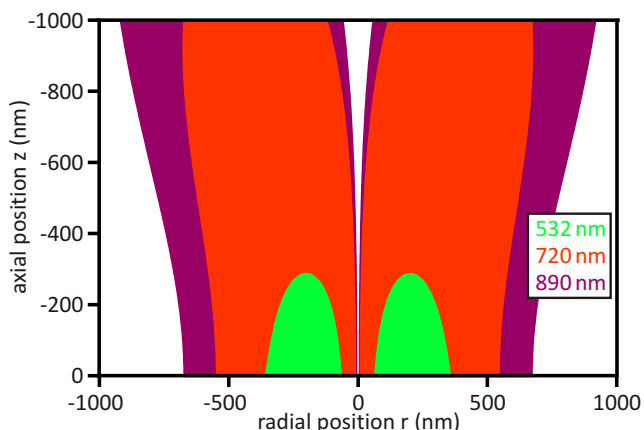
Figure 4.10 | Wavelength-dependent capture volume. A radial force of $3\,\mathrm{fN}$ is taken to mark a region for capturing the gold nanoparticles. One can see clearly that the volume is very small for the resonant laser and increases with increasing wavelength. The small capture volume at resonant wavelengths prevents lower printing powers due to the large time between printing events.

ure 4.11a), more than three times the value for resonant printing. This was most probably due to chromatic aberration from the microscope objective, which led to an offset between the laser and the imaging focal planes. This made simultaneous printing and imaging difficult and was most likely a large factor in the deviations. Currently, work is being carried out to shift the laser focal point to bring it to overlap with the imaging focal point and then repeat the measurements.
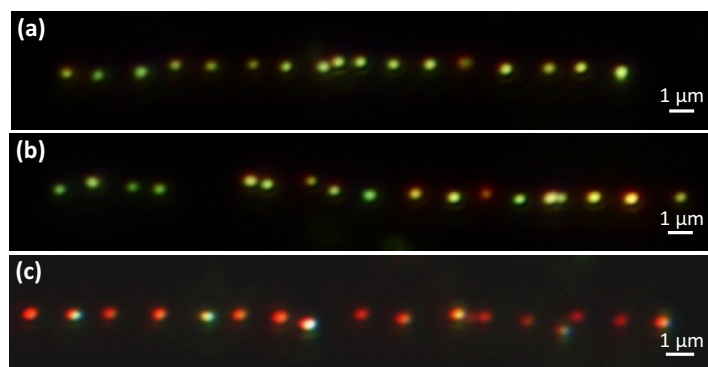
Figure 4.11 | Non-resonant printing accuracy. Printing the nanoparticles with a wavelength off resonance requires a higher laser power to exert the same force on the nanoparticles. (a) Here, using a laser wavelength of $720\,\text{nm}$ ($P = 1.51\,\text{mW}$), the precision is greatly reduced. However this could be due to chromatic aberrations from the microscope objective. (b) Increasing the laser power ($P = 1.96\,\text{mW}$) leads to a larger average deviation from the printing access. (c) At very high laser powers ($P > 3.2\,\text{mW}$) non-spherical nanoparticles are printed or single nanoparticle-dimers are created, with two nanoparticles printed in succession at the same spot.

A brief examination of the temperatures that are induced in the gold nanoparticles for non-resonant printing showed that the temperatures lay between $36\,°\text{C}$ and $48\,°\text{C}$ for wavelengths between $700\,\text{nm}$ and $890\,\text{nm}$. The nanoparticle temperature thus also has little influence on the printing process.

Three effects that do not occur for resonant printing are noticeable for the non-resonant printing. Firstly, the number of non-spherical nanoparticles that are printed is much higher than for resonant printing (Figure 4.11b). At the lowest laser power possible for printing, no such events are seen for printing with the $532\,\text{nm}$ laser, while for the red laser about 5% of the nanoparticles are non-spherical. This amount increases with increasing laser power and at $3.2\,\text{mW}$ power 95% of the printed nanoparticles are non-spherical. This is probably due to the larger forces exerted on the nanoparticle with a longitudinal plasmon resonance closer to the infrared. Secondly, if the laser power is increased further beyond a certain point then more than one single nanoparticle will be printed in one spot. After a spherical nanoparticle is printed, a second one is printed at the same spot. In the dark field microscope, one can see the green color of the first spherical nanoparticle. After

a short delay, a second nanoparticle can be pushed down, at which time the color of the previous nanoparticle changes to a deep red (Figure 4.11c). This means the nanoparticles must be close enough together for their plasmons to couple; and to have a scattering so far red-shifted, they must be closer together than $5\,\text{nm}$[141]. This effect could be used to create plasmonically coupled structures for devices. For laser powers below the threshold for printing, sometimes a third effect appears, namely optical trapping of gold nanoparticles. The nanoparticles are hereby pushed down towards the surface of the coverslips and are trapped, but do not stick to the surface. Once the laser is turned off, the nanoparticles diffuse away again. It is also possible to move the laser slowly and drag the nanoparticle along the glass surface. During the trapping events, the radial force acts towards the beam center and the glass surface counteracts the force in axial direction, creating a three-dimensional trap. At these laser powers, the axial force is not strong enough to overcome the barrier for printing.

The last important parameter we investigated is the effect of the thickness of the polyelectrolyte layer on the printing process. To vary the thickness controllably, we coat the coverslips in alternating layers of a positively charged (PDADMAC) and a negatively charged (PSS) polyelectrolyte (section 3.2.3). This leads to total thicknesses of $(2n + 1)\,\text{nm}$ with the number of PDADMAC layers, n (Figure 4.12a). The laser power necessary to achieve printing increases with each additional
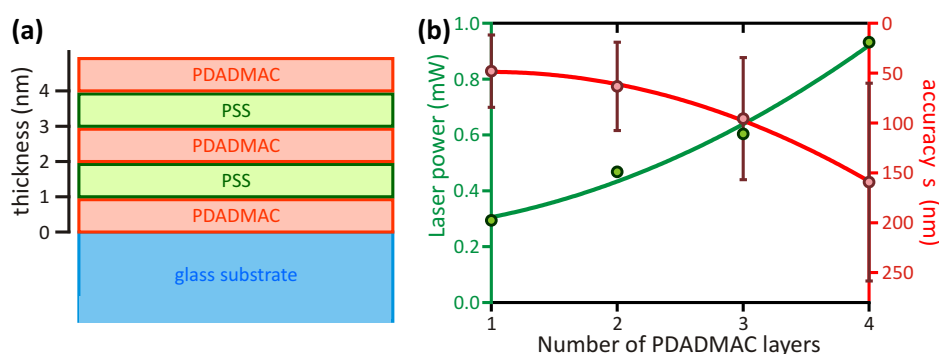

Figure 4.12 | Effect of polymer thickness on printing accuracy. (a) The differently charged polyelectrolyte layers are brought onto the glass coverslip to form a polyelectrolyte covering of controllable thickness. (b) The power necessary to achieve printing increases for thicker polyelectrolyte layers, while the printing accuracy worsens simultaneously.

polymer layer covering the glass coverslip (Figure 4.12b). The extra layers present an additional obstacle for the gold nanoparticles, shifting the the electrostatic potential towards greater separation distances and thus increasing the force that is necessary to overcome the printing barriers. As described in the power dependent measurements, increasing the laser power leads to a reduced printing accuracy. This is also the case for the extra polymer layers, which also require high laser powers. One additional effect occurs with extra polymer layers. The trapping that was before only seen for non-resonant laser wavelengths also becomes apparent for resonant printing. In addition, the optical trap is stable over a larger power range for the non-resonant wavelengths. This could be used in future to further increase the precision of the printing process. By using a laser power at which trapping occurs, but not printing, nanoparticles can be caught and directed with much higher precision to a location on the substrate. The power is then increased to a value at which the optical force can overcome the electrostatic barrier and the nanoparticle is printed.

4.3 Applications of Single Nanoparticle Laser Printing

The printing technique can be extended to print more complex structures. Two different ideas were investigated for this thesis. The first method makes use of the plasmon resonance of metallic nanoparticles. For metallic nanoparticles size, shape and material have a pronounced effect on the position and magnitude of the plasmon resonance. Knowing the cross sections of the nanoparticles, the force exerted on the nanoparticles by an incident laser beam can be calculated. The inter-particle forces according to the DLVO theory rely heavily on the Hamaker constants of the materials. Metals have similar values[84], ranging from 30 to $50 \times 10^{-20}\,J$. Thus it is possible to estimate the force needed to print the nanoparticles as well as the laser power at a given wavelength. The plasmon resonance of $80\,nm$ gold nanoparticles lies around $549\,nm$ and of same-sized silver nanoparticles around $447\,nm$ (Figure 4.13a). The extinction cross sections of the respective metals at their resonances are much larger than those of the other metal. Thus, if one uses a laser of wavelength $532\,nm$, near the gold plasmon resonance, and sets the power so that the optical force is just strong enough to print the gold nanoparticles, one
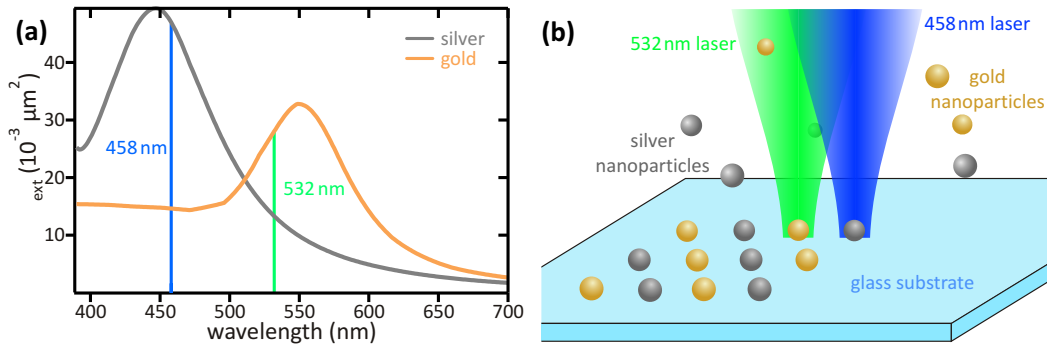
Figure 4.13 | Printing structures with nanoparticles of different metals. (a) Various metals have different strengths and positions of their plasmon resonances, as shown here in the case of $80\,$nm silver and gold nanoparticles. (b) This is used to print structures consisting of different metallic nanoparticles. The nanoparticles can be printed selectively by using multiple lasers, each emitting near the plasmon resonance of a nanoparticle. The laser power of each laser is then chosen so that one nanoparticle type is printed but not the other.

can ensure that the silver nanoparticles are not printed. The same is done for the silver nanoparticles with a laser, e.g. of $458\,$nm wavelength, ensuring that with this laser only silver and not gold nanoparticles are printed. Consequently one can print structures of nanoparticles, as described before, but now with the additional capability of placing different metallic nanoparticles at a desired location (Figure 4.13b). Of course this can also be done with other metals, choosing a laser at a wavelength appropriate for each metal.

This approach, while offering new possibilities to create complex plasmonic structures, is still limited. For example, printing of nanoparticles of the same material but of different sizes is very difficult, requiring lasers with wavelengths that are quite close together, and for small nanoparticles it becomes altogether impossible. This approach also fails if one wants to print nanoparticles without a plasmon resonance, i.e. by only using the optical forces, which depend on the geometric cross section of the desired nanoparticles. To be able to print such nanoparticles a different approach is necessary. As previously explained, when shifting the laser wavelength towards the near-infrared, we often observed nanoparticle trapping on the surface. At lower laser powers, the nanoparticles were held just above the surface of the glass coverslip by the optical forces exerted by the laser, which were not strong enough to print the

nanoparticles. With the microscope setup used in this thesis, there are many options for detecting the nanoparticles in the trap and analyzing their optical properties. The easiest is by looking at the nanoparticles through the ocular or the digital camera. But of course, the spectrometer can be used in more difficult cases and the excitation and emission wavelengths can also be specifically selected by inserting filters and switching between light sources. Thus the procedure to create complex structures is as follows:

A solution is prepared by mixing all nanoparticles to be printed on the substrate together. Next, the laser power is reduced so that nanoparticles are trapped but not printed. When a nanoparticle is caught in the trap, one determines optically whether the nanoparticle is the correct one to be printed. If it is, the laser power is increased, enabling the laser forces to overcome the electrostatic barrier and print the nanoparticle. If the trapped nanoparticle is not the correct one, the laser is switched off, the nanoparticle diffuses away from the trap and the process can be repeated (Figure 4.14).
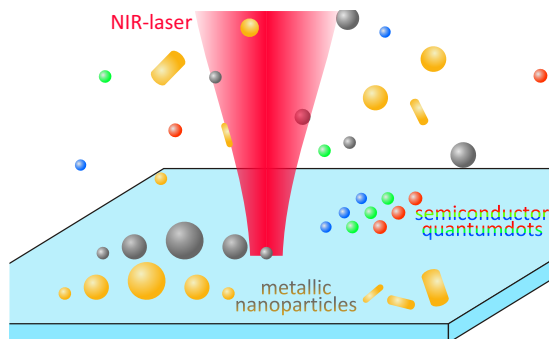
Figure 4.14 | Printing complex structures by trapping nanoparticles. A near-infrared laser can trap nanoparticles by pushing them against the glass coverslip. These can be analyzed optically and, if the trapped nanoparticle is the one to be printed, the laser power is increased to print the nanoparticles. If they are not the correct nanoparticles, the laser is switched off, the nanoparticle diffuses away and the process can be started anew.

With the methods discussed so far it is possible to create complex structures with various nanoparticles, but without having control over the orientation of the nanoparticles. For spherical nanoparticles this is of course not necessary.

Nevertheless, there are other types of nanoparticles, e.g. nanorods or bipyramids, whose shape gives them special optical properties. Depending on the desired function of the printed structures, it could be essential to have control over the nanoparticles' orientation. Our approach to accomplish this relies on the capability of aligning plasmonic nanoparticles using polarization dependent optical forces[142]. In their work, Tong et. al. showed that plasmonic nanoparticles will rotate and align in a polarized laser beam. For example, silver nanorods and gold nanosphere dimers will align with the long-axis dipole parallel to the plane of polarization of linearly polarized light that is tuned to the wavelength of the long-axis resonance. This is a result of the high long-axis dipole polarizability aligning to reduce the potential energy of the nanoparticle inside the electric field of the laser.
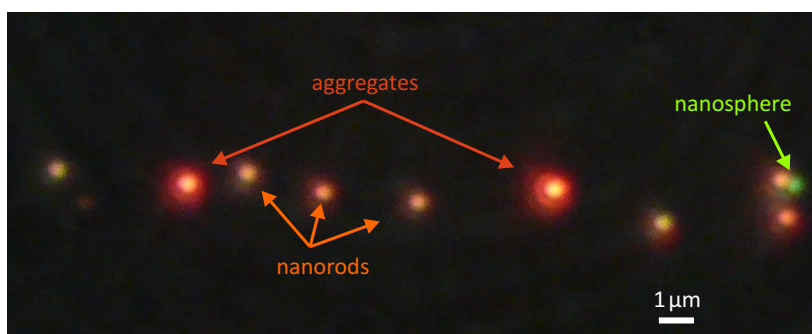
Figure 4.15 | Gold nanorods printed on a glass substrate. The nanorods can be distinguished by their orange color, resulting from the combination of scattered light from both the transverse as well as the longitudinal plasmon resonance. Unfortunately, the solution was not very pure, containing larger aggregates and also nanospheres.

As a first experiment, we used gold nanorods with dimensions of 73x25 nm and 60x25 nm. The nanorods long-axis resonances lie at wavelengths of 700 and 650 nm respectively. They were covered, like the modified gold nanospheres, with a CTAB double-layer, providing them with a positive surface-charge. The glass coverslips were coated accordingly with a layer of PDADMAC to prevent spontaneous aggregation of the nanoparticles on the glass surface. The same printing setup was used as before, with the Tsunami laser set to the resonance of the long-axis of the respective nanorods. In a first attempt, the nanoparticles were printed onto the glass substrate to prove that they can be printed. As can be seen

in Figure 4.15, the nanorods could be printed in the same way as the nanospheres were in the last section. The solution containing the nanoparticles was not very pure, with larger aggregates and spheres also present in the solution. The rods can be distinguished quite clearly due to their orange hue, which results from the combination of scattered light from both nanoparticle axes (Figure 4.16a).
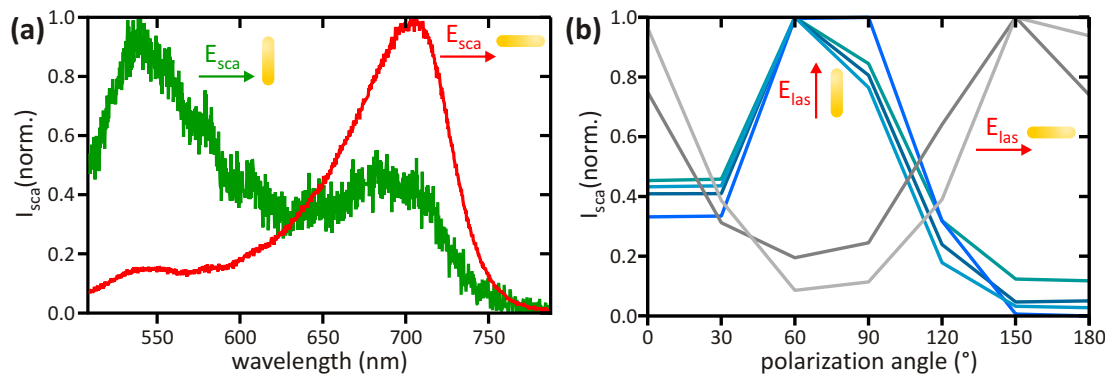
Figure 4.16 | Aligning gold nanorods on a substrate with linearly polarized laser light. (a) The nanorods each have two plasmon resonances, which can be seen separately by rotating a polarization filter in the detection path. (b) Polarization dependence of the scattering intensity of the longitudinal plasmon (I_{sca}). Here the intensities are plotted for 6 nanorods. Of these 4 were aligned in one direction (blue curves) and the other two were aligned perpendicular to them by rotating the polarization direction of the laser beam (E_{las}). The nanorods generally aligned on the substrate parallel to the polarization angle of the laser used to print the nanoparticles. An efficiency of 60% correctly aligned nanorods was achieved (out of 20 printed nanoparticles).

Next, we tried to align the nanoparticles along a certain direction. This was done by setting the polarization of the laser to a fixed angle, which can be rotated freely. By printing with a fixed polarization angle and then rotating this by $90°$, the nanoparticles printed after the rotation should be aligned perpendicular to the ones printed before the rotation. According to a previous publication [142], the power density required for aligning the rods is in the region of $20\,\text{MW/cm}^2$, which is two orders of magnitude larger than the power densities used to print the gold nanospheres. This is the main reason for the printing accuracy of the nanorods being so poor, together with the chromatic aberration of the microscope objective. Nevertheless, we attempted to align the nanorods on the glass coverslip. To monitor

the position of the nanorods, a polarization filter is inserted into the detection path and the scattering spectra of each rod are recorded, rotating the filter between $0°$ and $180°$. As can be seen in Figure 4.16b, we were able to align the rods parallel to the polarization angle of the laser. This angle can be rotated freely and through it the angle of the printed nanorods. The maximum efficiency we achieved was 60% of the nanorods in a row aligned along the desired direction (20 nanoparticles in a row). The approach can be improved significantly by adjusting the laser focal plane to match the optical focal plane. Additionally, more experiments are necessary to find out how the alignment on the glass coverslip depends on the laser power and wavelength.

4.4 Discussion

In this chapter a new method was presented for creating patterned nanostructures by placing individual nanoparticles onto substrates with a precision comparable to the nanoparticles' own dimensions. This method is novel which, instead of just optically trapping nanoparticles by a laser[127], uses the laser forces to collect the nanoparticles from the solution, guide them towards the center of the beam, while propelling them towards the glass surface and there attach them to the substrate. We demonstrated this by printing $80\,\mathrm{nm}$ gold nanoparticles onto a glass substrate using a laser with a wavelength ($523\,\mathrm{nm}$) near the plasmon resonance of the nanoparticles. The substrates were covered with a polyelectrolyte which through electrostatic repulsion prevents spontaneous binding of the gold nanoparticles. The total optical force exerted on the nanoparticles is the sum of a gradient force and of a combined scattering force, the latter resulting both from scattering and absorption of photons. In the axial direction the scattering force dominated completely, pushing the nanoparticles in the direction of the substrate. If the laser power was high enough, the optical forces overcame the electrostatic repulsion, so that the gold nanoparticles bound and were thus printed on the glass substrate. This binding, resulting from attractive van der Waals forces between the gold nanoparticles and silica, was very strong and the printed patterns survived many rinsing procedures without damage. In comparison to many previously reported methods for single

nanoparticle printing, which all rely on an electrostatic binding mechanism to attach the nanoparticles, our binding was stronger and should also be more stable. Moreover, no complicated preparation methods were necessary, as in many other reported procedures which require a complex, multi-step patterning of the surface with lithography masks or various inking and transfer steps. This not only speeds up our process but makes it more versatile as the desired patterns can be programmed into a computer, which can monitor and guide the printing through optical detection of the printed nanoparticles.

The maximum precision we were able to achieve while printing rows of $80\,$nm gold nanoparticles was $38\,$nm. This precision is much better than previously reported methods enabling the printing of single nanoparticles, where the precision generally lies above the size of the individual nanoparticles[29,127,143]. The power necessary to achieve the precision with our method was only $175\,\mu$W, which corresponds to a laser power density of $15.8\,$kW/cm^2 and a total axial force of $51\,$fN acting on the nanoparticles. In radial direction, the scattering force and the gradient force act together in front of the focal plane, guiding the nanoparticles towards the beam center. Behind the focal plane the scattering force changes direction, such that $150\,$nm behind the focus the nanoparticles are scattered away from the beam center. Thus, the position of the focal plane of the laser has a great effect on the precision of the mechanism. At these power densities the area on the substrate surface in which the optical forces were able to overcome the electrostatic barrier was so small that only one nanoparticle was printed at a given location. The low laser power thus automatically prevents the printing of nanoparticles at undesired positions.

The laser power is the most critical parameter in the process as it controls not only the precision of the process but also its speed. Higher laser powers than those mentioned above led to a reduced precision because of three separate effects: the area in which the optical forces can overcome the electrostatic repulsion becomes larger; the heating of the gold nanoparticles leads to an increased diffusion; and the time during which the weak radial forces guide the nanoparticles towards the center of the beam is reduced. At the same time the laser power determines the volume in the solution in which the radial forces are strong enough to overcome the

thermal diffusion of the nanoparticles, guiding the nanoparticles towards the glass surface. Increasing the laser power also increases the capture volume, reducing the time between printing events. Thus, one must find an optimal value which enables both high enough precision and acceptable speed. Using a laser power of $P = 294\,\mu W$ we were able to print rows of gold nanoparticles to an accuracy of $48\,nm$ per nanoparticle at a rate of one nanoparticle every five seconds (Figure 4.7).

The nanoparticles could also be printed using an non-resonant laser. For this we used a tunable Ti:Sa laser, which emits wavelengths between $700\,nm$ and $890\,nm$. The power necessary to achieve printing was much higher than for the resonant wavelength (between $1.5\,mW$ and $3\,mW$), due to the very low absorption and scattering cross sections of the nanoparticles at these wavelengths. However, the total force acting on the gold nanoparticles is one order of magnitude lower for the non-resonant printing, being only around $5\,fN$. This effect can be explained by examining the ratio of the radial force to the axial force. A laser beam emitting at a wavelength shifted far to the red from the plasmon resonance exerts strong radial forces on the nanoparticles, guiding them to the center of the beam. This leads to a larger capture volume, i.e. the volume in the solution out of which the nanoparticles can be guided to and printed on the substrate (Figure 4.10). This consequently reduces the time between printing events significantly. At resonant wavelengths and low laser powers the capture volume is so small that the time between printing events becomes very long. Thus, the reason the nanoparticles could not be printed for lower forces than the observed $51\,fN$ is that the capture volume was so small that a printing event did not occur within the $30\,min$ observation time at the respective setting of the laser power.

Taking these facts into account, using non-resonant lasers wavelengths to print gold nanoparticles should be more precise and much faster than for resonant printing. In our experiments, we were only able to achieve a precision of $143\,nm$, which is worse than for resonant printing, but still acceptable when compared to previously reported methods. The reduced precision can be explained by a chromatic aberration of the microscope objective. This led to an axial offset between the optical focus of the microscope and of the laser beam. The aberration made simultaneous, effective

focusing of the laser and imaging of the nanoparticles difficult and consequently led to the reduced precision. However, it could be compensated by introducing a telescope system into the laser beam path. By slightly detuning the telescope, the focus of the laser beam is shifted with respect to the optical focus of the microscope objective and the two foci can be brought to overlap. This is being pursued in current experiments.

Using the non-resonant laser wavelengths described above has even more advantages. We showed that it is possible to create plasmonically coupled structures out of single nanospheres at these wavelengths. The red laser at higher laser powers enable the nanoparticles to be printed close enough together than two nanoparticles form single dimers (Figure 4.11). It was also possible to create short plasmonic wires in dilute solutions using the same laser settings but moving the laser by a small amount after each printing event. With the non-resonant laser it was also possible to trap nanoparticles at lower laser powers by pushing them against the polyelectrolyte covering the glass surface. The laser power was not high enough to overcome the electrostatic barrier, but it held the nanoparticles in place on top of the substrate. The nanoparticles could be moved over the surface by slowly moving the laser spot laterally. This trapping enables an additional highly attractive feature. By trapping the nanoparticles and selecting according to their optical properties, different nanoparticles, present in the same solution, can be printed onto the glass surface. The laser power is set to trap the nanoparticles, and if the observed nanoparticle is the correct one to be printed the laser power is increased, printing the nanoparticle at the position it was trapped. This procedure eliminates the necessity for switching solutions during the entire fabrication process of complex nanostructures. Up-to-date no method presented for nanoparticle printing has shown the capability of achieving this. Furthermore, by using linearly polarized light, we were able to orient and print non-spherical nanoparticles on a substrate. This was done by tuning the wavelength of the printing laser to the longitudinal wavelength of the nanoparticle. The polarizability difference along the different axes of the nanoparticle led to the nanoparticles aligning parallel to the polarization plane of the printing laser. This was demonstrated in experiments presented here (Figure 4.16a) and could enable high efficiency sub-wavelength waveguides[144].

The printing method could also be used to print more complex structures out of different metallic nanoparticles. This is possible because of the different positions and magnitudes of the plasmon resonances of different metals. For example, by using a laser at 532 nm and one at 458 nm, one can either print gold or silver nanoparticles (sizes approx. $20 - 80$ nm). The power of the green laser is set so that it is just strong enough to print gold nanoparticles, and the same is done with the blue laser for the silver nanoparticles. By selectively turning one laser on and the other off, either gold or silver nanoparticles are printed. Again, this is a feature that to our knowledge has never before been demonstrated.

We developed a model of the patterning process, which used the optical forces acting on a nanoparticle and the DLVO-theory to explain the initial repulsion and later binding of the nanoparticles to the substrate surface. This theory encountered a large problem, in that it could not accurately predict the minimum power necessary for printing. On the contrary, our prediction was several orders of magnitude higher than the experimentally obtained value. However, this is only a minor drawback and in no way disproves our model. The DLVO-theory is not a complete theory of colloidal suspensions. There are also many forces acting on nanoparticles in the solution that are not taken into account by this theory. Furthermore, a minor change in the ionic strength of the solution, which we could only estimate, can have a significant effect on the printing power (Figure 4.3b). On the other hand, the model does explain several of the observed phenomena. It explains for example why at low laser powers only one nanoparticle can be printed at a specific site and at higher powers several can be printed. It also explains the dependence of the precision and speed of the printing process. Furthermore, it gives a reason why the minimum force needed for resonant printing is much higher than for non-resonant printing. It also explains the observations made in the next chapter on nanoparticle guiding. All of these observations show that while the model has some problems and obviously could be refined, it is able to explain many observed phenomena.

5 Manipulating Phospholipid Membranes with Gold Nanoparticles

In recent years impressive advances have been made in imaging structural features of cellular and subcellular systems[145,146], and in making their pathways visible[147,148] using optical techniques with nanometric resolution. The development of regulated nanoscopic sources of heat is an important step towards generating tools capable of investigating the thermodynamics of local processes at the nanoscale. Metallic nanoparticles are well known to efficiently convert light into heat when they are irradiated at their plasmon resonances.[60,149]. This optical heating has been capitalized on for many applications including microscopy[150], biomolecular analysis[25], remote release[151,152] as well as cancer therapy through the thermal destruction of tumor cells[153]. Metallic nanoparticles can deliver defined amounts of heat to nanoscopically confined regions. Through this one can not only obtain local information on the nanoscale but also exert control over certain thermally regulated processes. Up to the present this potential of gold nanoparticles has scarcely been explored. In this chapter, we exploit the properties of gold nanoparticles to create investigative and manipulative nanotools. The basis for this is an investigation of methods for binding gold nanoparticles to phospholipid membranes. We demonstrate how gold nanoparticles can be used for investigating membrane thermodynamics, manipulating the processes occurring therein and for enhancing drug delivery.

5.1 Attaching Gold Nanoparticles to Phospholipid Membranes

In order to manipulate phospholipid membranes with gold nanoparticles, these must be brought into close contact, and ideally bound to the membranes. Therefore we investigated how to bind gold nanoparticles to phospholipid membranes, which factors affect binding, and how it can be controlled. For the initial studies, giant unilamellar vesicles were grown, as described in section 3.2.1. Because the gold nanoparticles from BBInternational have a negative surface charge, we added a positively charged phospholipid to facilitate binding. The vesicles were prepared by adding the two phospholipids to the growth chamber. The first, *1,2-dioleoyl-sn-glycero-3-phosphocholine (DOPC)*, does not have a total charge, has a melting temperature of $T_m = -21\,°\text{C}$ and was the phospholipid used for most of the experiments. The second phospholipid, *1,2-dioleoyl-3-trimethylammonium-propane (DOTAP)*, has a single positive charge, and was mixed with the DOPC in a ratio of 1:19.

With the dark field microscope used for the experiments it is possible to image gold nanoparticles down to a size of $20\,\text{nm}$. While $10\,\text{nm}$ large gold nanoparticles bound to GUVs, causing the membrane to become more green, individual nanoparticles could not be distinguished (Figure 5.1a). On the other hand, $40\,\text{nm}$ large gold
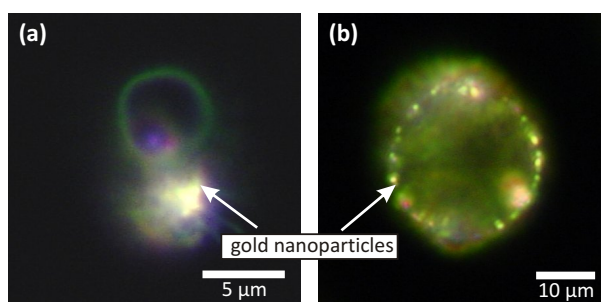

Figure 5.1 | Binding of citrate-coated gold nanoparticles to phospholipid bilayers. (a) While $10\,\text{nm}$ large nanoparticles cannot be seen individually in the dark field microscope, (b) $40\,\text{nm}$ gold nanoparticles can be seen quite clearly. They attach readily to the vesicle membrane.

nanoparticles binding to GUV membranes can be seen easily (Figure 5.1b). Because the scattering cross section increases with size, larger nanoparticles can be detected more easily. In order to reduce imaging time and increase the quality of the images, we mainly used $80\,\mathrm{nm}$ gold nanoparticles for the experiments.

The concentration of gold nanoparticles is a most important parameter for the binding process. At very low concentrations most GUVs do not have nanoparticles bound to them (Figure 5.2a), while high concentrations deform and destroy the GUVs (Figure 5.2c). Mixing the GUV and gold solutions in a ratio of 300:1 for the $80\,\mathrm{nm}$ nanoparticles and 600:1 for the $40\,\mathrm{nm}$ nanoparticles left most of the GUVs coated with between three and five nanoparticles. This mixing ratio allows the study of individual nanoparticles, as the nanoparticles will be separated clearly from each other due to the size of the GUVs ($> 5\,\mathrm{\mu m}$).
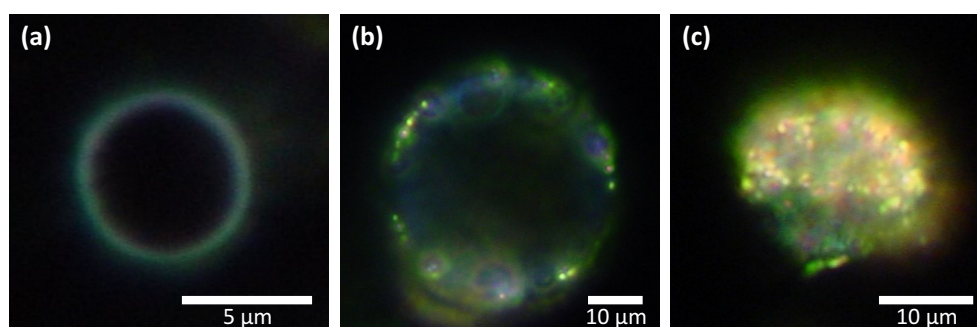
Figure 5.2 | Binding efficiency of gold nanoparticles to phospholipid GUVs depending on the nanoparticle concentration. The concentration is a crucial parameter, since (a) at low concentrations hardly any binding is observed and (c) at high concentrations the nanoparticles deform and destroy the GUVs. (b) In order to study single nanoparticles on the phospholipid membranes, the concentration must be kept well controlled between these extremes.

To determine the nature of the nanoparticle binding, GUVs were prepared adding either the positively charged phospholipid DOTAP or a negatively charged phospholipid, such as *1,2-dipalmitoyl-sn-glycero-3-phosphothioethanol (DPPTE)* or *1,2-dioleoyl-sn-glycero-3-phospho-L-serine (DOPS)* in certain ratios to the DOPC. Vesicle growth was achieved with charged phospholipid to DOPC ratios up to 1:9. For higher charged lipid contents, the vesicles were either not stable or did not form at all. As

in the previous experiments the citrate-coated gold nanospheres bound readily to the positively charged vesicles, but hardly at all to the pure DOPC vesicles, and not at all to the negatively charged ones (Figure 5.3a). This is due to the nature of the binding, which is electrostatic. The pure DOPC vesicles have a slight net negative charge in water[154,155], probably from acidic impurities or hydration layers, and therefore they also repel the gold nanospheres. To confirm this binding mechanism, we exchanged the gold nanospheres with gold nanorods, which were prepared in this group and coated with CTAB. The vesicles were prepared with DOTAP and DOPC phospholipids in a ratio of 3:93. The amount of DOTAP should easily compensate any negative charges from the DOPC molecules, giving the vesicles a positive net surface charge. To our surprise, the nanorods bound to these vesicles (Figure 5.3b), although not in such large numbers as for the control sample with the nanorods and the negatively charged GUVs. This suggests a completely different
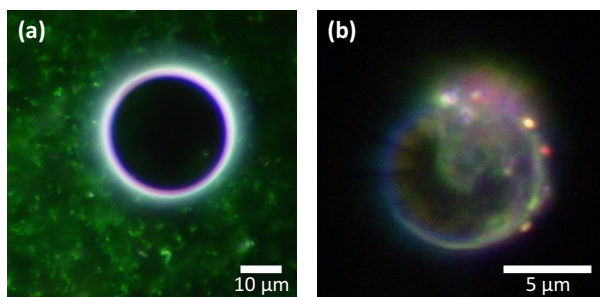
Figure 5.3 | Binding of gold nanoparticles to phospholipid GUVs. (a) Even at high concentrations, citrate-coated nanospheres do not bind to negatively charged GUVs due to electrostatic repulsion. (b) Gold nanorods coated with CTAB, however, bind even to positively charged GUVs, hinting at a non-electrostatic binding mechanism.

binding mechanism. As stated before, the CTAB, having a similar structure to the phospholipids, with a long nonpolar chain and a polar headgroup, forms a bilayer around the gold nanoparticles. Hence it is plausible that the CTAB molecules bind to the phospholipids much in the same way as they bind to each other. This creates a stable, merged bilayer. Whether the nanoparticle is enveloped entirely by the membrane or only partially depends on many factors, including the bending modulus κ of the membrane and the nanoparticle size, and is very difficult to determine both theoretically and experimentally[156–158]. Even so, the binding must be fairly strong, as it is able to overcome the electrostatic repulsion from the net charges of the GUV

and the CTAB-coated gold nanoparticle. Experimentally, cryo-electron microscopy studies might be able to shed some light on the exact binding mechanism. This was, however, not a primary concern within the scope of this work.

5.2 Growing Gold Nanoparticles Directly on Phospholipid Membranes

Instead of growing GUVs by electroformation and afterwards attaching gold nanoparticles to them, we developed the idea of growing gold nanoparticles directly on the phospholipid membrane of the GUVs. This not only has advantages for the study of gold nanoparticle-membrane interactions, but may also enable new applications such as liposome internalization[159] or drug delivery[160–162]. Loading vesicles with nanoparticles has previously been done by mixing preformed nanoparticles with vesicles directly (as discussed in the last section) or by spontaneous reduction of metal ions by a vesicle forming component[163,164]. However, these procedures all have one or more drawbacks. Often, the methods are very slow, with some of them taking days for the nanoparticles to reach full size[165]. Also, the size of the nanoparticles and the extent of loading of the vesicles cannot be controlled. Using protocols for preformed nanoparticles for direct growth on vesicles is generally of no use. These protocols either use reducing agents, e.g. $NaBH_4$, that are highly toxic to cells[166], or else the production method requires conditions that would destroy the vesicles during growth (e.g. high temperature synthesis using citrate as a reducing agent[116]). In light of all of these problems, the idea came for the rapid, controlled loading of gold nanoparticles onto phospholipid vesicles, suitable for biomedical applications.

The procedure that was developed is simple and is illustrated in Figure 5.4. GUVs are grown, as described in section 3.2.1, using the phospholipid DOPC and a sucrose solution. Charged GUVs are created by mixing the DOPC with a charged lipid in a mass ratio of 10:1. Adding *1,2-dioleoyl-sn-glycero-3-ethylphosphocholine (DOPC+)* to the DOPC creates positively charged vesicles, while adding *1,2-dioleoyl-sn-glycero-3-phosphopropanol (DOPP)* produces negatively charged vesicles. The size of the doped GUVs is comparable to the GUVs consisting only of DOPC. The solution

containing the GUVs is mixed with the gold precursor ($HAuCl_4$) and with ascorbic acid. The latter is added at a concentration of 1.6 times the concentration of gold ions and is used as a reducing agent for the gold. The gold salt concentration was varied between 4×10^{-6} M and 5×10^{-5} M. The growth process can be monitored by observing the extinction spectrum of the solution and by examining the GUVs before and after the process in a dark field microscope. The entire growth process takes $1 - 2$ h depending on the gold ion concentration. In the presence of the GUVs, the gold nanoparticles nucleate and grow preferentially on the membranes rather than directly in the solution.
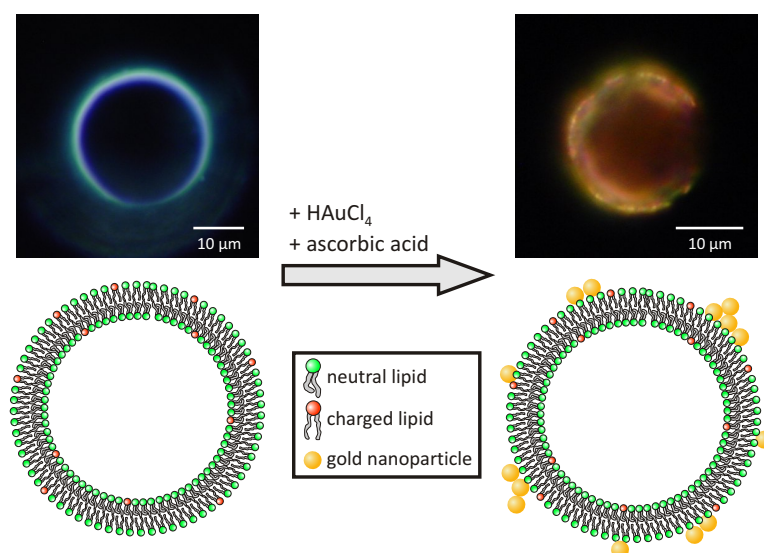
Figure 5.4 | Controlled loading of gold nanoparticles on phospholipid GUVs. GUVs are prepared by electroformation (left), mixed with a gold salt and ascorbic acid. Nanoparticles nucleate and grow preferentially on the GUV membrane (right) instead of in the solution.

To understand the growth process, the components were mixed separately. These control experiments prove that neither the phospholipids nor the sucrose are able to reduce the gold ions, confirming the ascorbic acid as the reducing agent. Varying the sucrose concentrations between 10 mM and 700 mM showed no effect on the growth process. The concentration of $HAuCl_4$ has a strong effect on the loading, however, as the amount of nanoparticles on the GUVs grows considerably with increasing gold ion concentration (Figure 5.5). Gold nanoparticle density can even be increased high

enough to induce plasmonic coupling between the nanoparticles (Figure 5.5c), which tend to aggregate together.
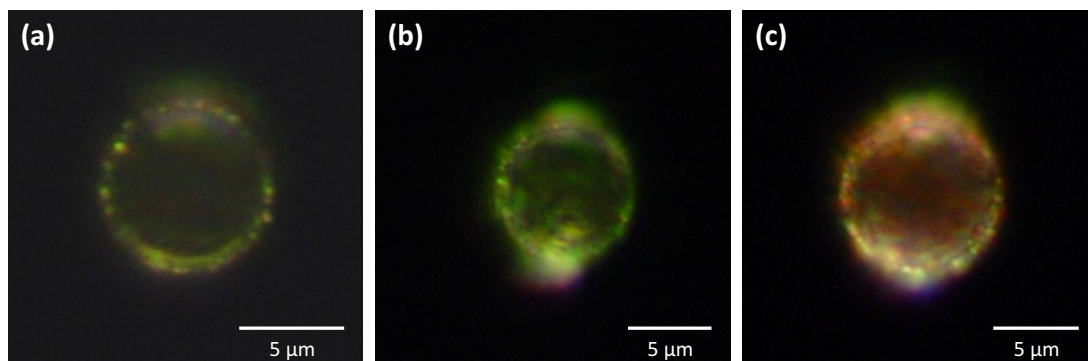
Figure 5.5 | Importance of the HAuCl$_4$ concentration on gold nanoparticle growth. The concentration of gold ions was increased from (a) 8×10^{-6} M to (b) 2×10^{-5} M, to (c) 4×10^{-5} M. The increase in nanoparticle density with increasing gold ion concentration can be seen clearly and plasmonic coupling becomes apparent at the highest concentrations.

Introducing charged lipids or ionic surfactants into vesicles can change a vesicles' properties in many ways[167,168]. To study this we added charged phospholipids to the DOPC vesicles, making both anionic and cationic vesicles, and comparing them to the undoped vesicles. The charged phospholipids have a pronounced effect on the gold nanoparticle growth. We first analyzed the effect by examining the nanoparticle-coated vesicles in the dark field microscope (Figure 5.6). The growing procedure itself is highly efficient, with around $98\,\%$ of the vesicles being loaded (over 300 vesicles imaged), with the exception of GUVs grown with a $10\,\%$ fraction of negatively charged lipid. At the lowest concentrations of the gold precursor used (8×10^{-6} M), there is a clear difference between the GUVs. The anionic GUVs are generally unloaded, with one out of twenty vesicles showing one or sometimes two seperate nanoparticles. These are fairly large, as can be seen from the intensity and color of the scattered light. The undoped GUVs have many more nanoparticles bound to them. The green color and lower intensity of the scattered light shows that the nanoparticles are probably spherical and not as large. The cationic GUVs have mainly aggregates, which can be identified by the orange-red hue of the scattered light, but also some single spherical nanoparticles attached to their membranes.

concentration HAuCl$_4$
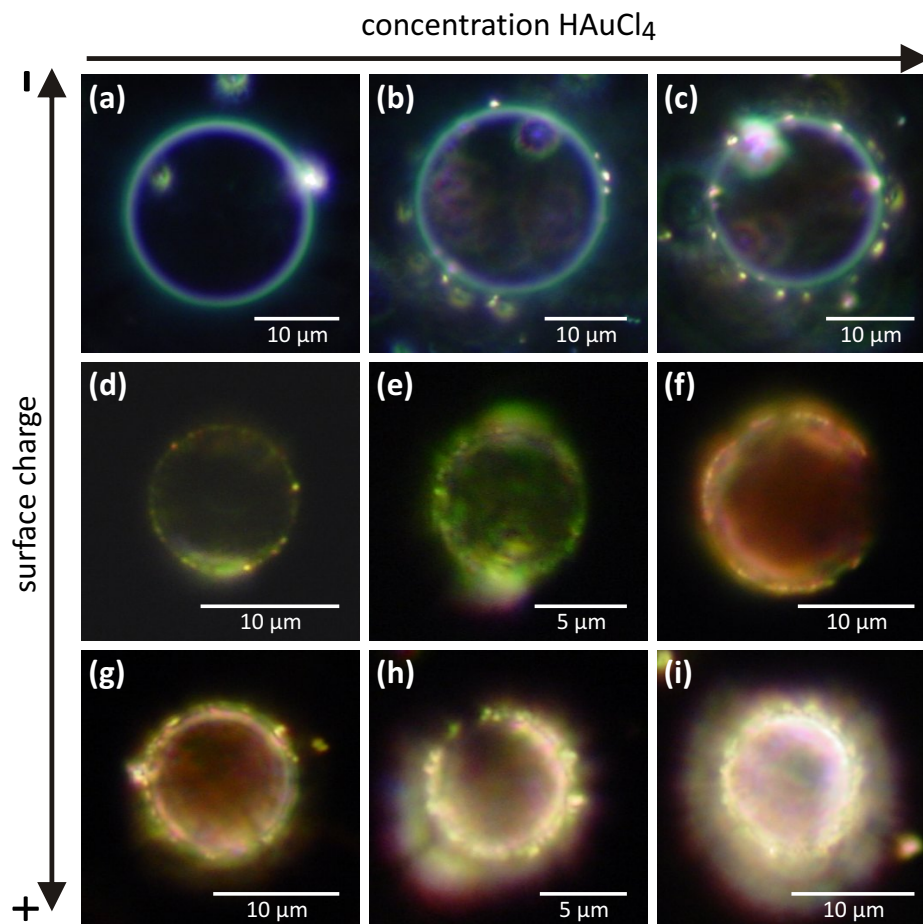
Figure 5.6 | Gold nanoparticles grown on phospholipid GUVs. Varying both the surface charge of the GUVs as well as the concentration of the gold precursor has a large effect on the growth process of the gold nanoparticles.

Increasing the concentration of the gold salt to 2×10^{-5} M increases the amount of nanoparticles attached to the anionic vesicles, while seemingly not affecting nanoparticle size. For the undoped GUVs the amount of nanoparticles also increases, with most of the membrane now appearing green. The more intense but still clearly green scattered light from the nanoparticles suggests that these are larger, but still spherical in shape. The inter-particle distance is also not close enough for the nanoparticles to couple plasmonically. The surface of the cationic GUVs is almost completely covered, as can be seen also by the amount of scattered light that is not emitted from the focus plane, but is still recorded. The scattered light is far

less green in the color and some larger single nanoparticles or aggregates are also visible. At the highest concentration of the gold precursor used (4×10^{-5} M), the gold nanoparticle loaded anionic GUVs showed the same trend as before: an increased amount of nanoparticles attached to the anionic vesicles, while the nanoparticle size was not visibly affected. The difference between the the lower and highest concentrations is far larger for the undoped GUVs. Now the GUVs no longer show a predominantly green coloring, but a distinct orange-red color. Single nanoparticles or larger aggregates can be seen, some of which appear green and some red. Single nanoparticles can no longer be seen on the cationic GUVs. The scattered light is so intense that they must be nearly completely covered with nanoparticles or nanoparticle aggregates.
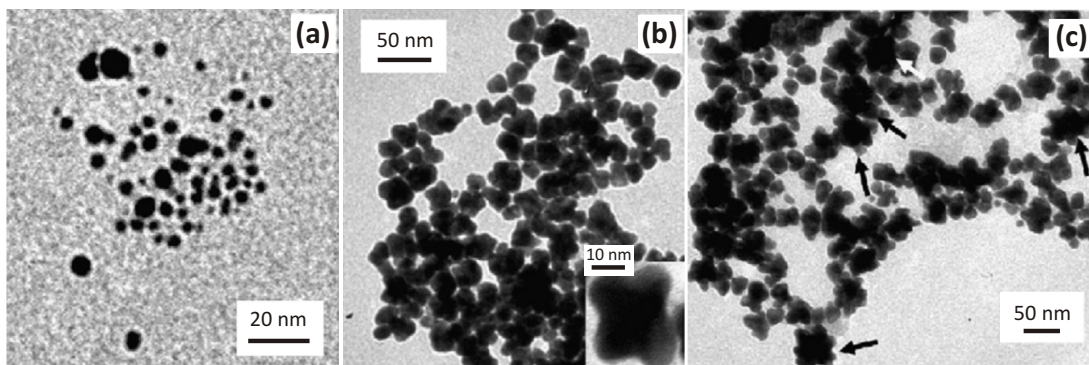
Figure 5.7 | Transmission electron microscope images of gold nanoparticles grown on phospholipid vesicles. (a) The nanoparticles formed are very small and mostly spherical when grown on positively charged vesicles at low precursor concentrations. (b) At higher concentrations the nanoparticles become larger and some are no longer spherical. (c) At the same high concentration as in (b), the gold nanoparticles grown on negatively charged vesicles are much larger and also predominantly non-spherical.

To understand this behavior in more detail we looked at the samples in a *transmission electron microscope (TEM)* (Figure 5.7). Unfortunately the vesicles do not survive the drying process necessary for preparing samples for the TEM, but the individual gold nanoparticles can be seen clearly. It cannot be determined which nanoparticles formed on the GUV surfaces and which did not. Additionally, no information can be gathered on the density and distribution of the gold nanoparticles on the vesicles. However, a general idea about shape and size of the nanoparticles can be obtained

by comparing these images. The nanoparticles grown at the lowest concentrations are mainly spherical and are a few nanometers in size (Figure 5.7a). At higher concentrations the nanoparticles become larger in size and also lose their spherical shape (Figure 5.7b). There is a clear dependence of the nanoparticle size on surface charge. The nanoparticle size is smallest on the cationic GUVs and largest on the anionic GUVs (Figure 5.7c).

Even though individual vesicles cannot be examined under the TEM, this can be done under the dark field microscope, with which it is also possible to take scattering spectra of the GUVs. This can give further insight into the distribution of nanoparticle size, shape and state of aggregation and thus of the growth mechanism. These measurements also show that all three of the GUV types behave quite differently (Figure 5.8). The scattering spectra of the gold nanoparticle-loaded GUVs show a complex feature that can be fitted with three Gaussian functions. For each type of GUV and concentration, there is a slight shift in the height and position of these peaks, but the trends are the same for each case. The spectral behavior of the bound gold nanoparticles is different than for gold nanoparticles grown in phospholipid-free solutions[169]. The latter are almost exclusively spherical and extinction spectra of gold nanoparticle solutions show almost no extinction for
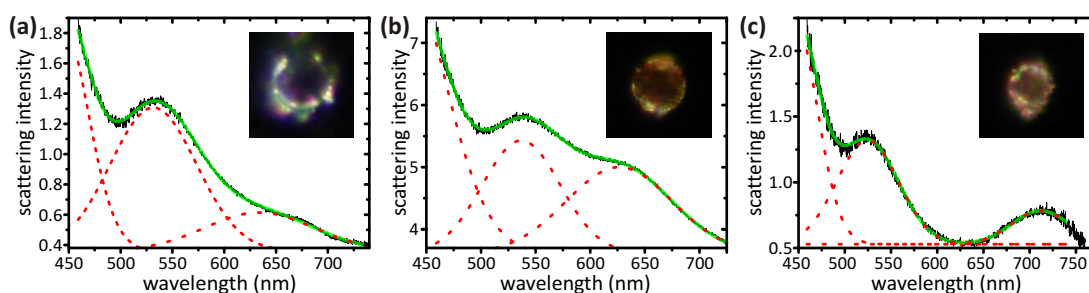
Figure 5.8 | Scattering spectra of vesicles coated with gold nanoparticles. All three spectra can be fitted with three separate Gaussian functions. The two at the shorter wavelengths are due to membrane scattering ($440\,$nm) and scattering by single spherical nanoparticles ($525\,$nm). The shape of the individual spectra is very different. (a) While the scattering spectrum of the anionic GUVs is dominated by the spherical nanoparticle scattering, (b) the spectrum of the neutral GUVS shows an increased contribution from nanoparticle aggregates and (c) the cationic sample displays a strongly red-shifted peak characteristic for larger aggregates. The inserts show the vesicle belonging to the respective spectrum.

wavelengths longer than $600\,nm$. The vesicle membrane is responsible for the intense scattering peak centered between $425\,nm$ and $445\,nm$, which is confirmed by measuring the scattering spectra of pure phospholipid GUVs. The second scattering peak, centered between $525\,nm$ and $535\,nm$ is due to the scattering of single, spherical nanoparticles smaller than $50\,nm$ in diameter. This is the predominant scattering source of gold nanoparticles for all samples. In both the anionic and undoped GUV samples the third scattering peak is centered between $625\,nm$ and $640\,nm$.
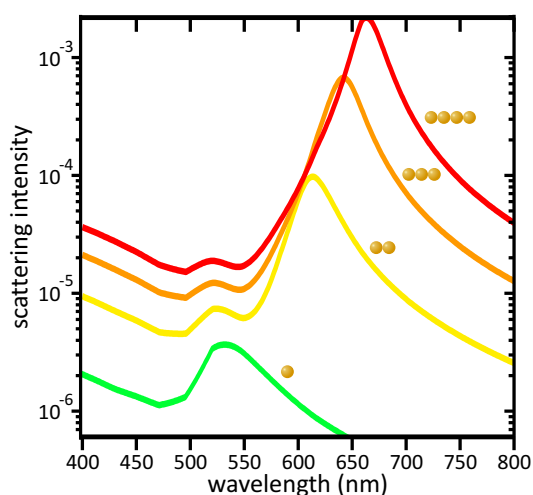

Figure 5.9 | Calculated scattering spectra for linear chains of 20 nm large gold nanoparticles. At higher gold precursor concentrations, the scattering spectra of the vesicles show a strong increase in the orange-red spectral region. This is probably due to small spherical nanoparticles aggregating together in chains, where their plasmons can couple. This graph shows calculated scattering spectra from such chains. Two 20 nm gold nanoparticles touching each other already can explain much of the observed scattering. Longer chains of gold nanoparticles shift the emission maximum to even longer wavelengths and increase scattering intensity significantly.

There is a clear difference in the relative intensities of the two gold nanoparticle scattering peaks. In the anionic GUVs the peak at $530\,nm$ is roughly three times as intense as the peak at $640\,nm$. In the undoped samples the two peaks have roughly the same intensity. In the cationic GUV samples the third peak is shifted considerably to longer wavelengths, with a maximum between $710\,nm$ and $740\,nm$. The relative intensity of the single nanoparticle and aggregate peaks of the cationic GUVs lies in between the values for the neutral and anionic GUVs. The peak at the longest wavelengths in all the samples is due to light scattering from non-spherical nanoparticles and small aggregates of plasmonically coupled single nanoparticles. To demonstrate this we calculated scattering spectra of linear chains of touching $20\,nm$ spherical gold nanoparticles (Figure 5.9). Increasing the aggregate size leads to a considerable red shift of the resonance peak and a strong increase in the

scattering intensity. This shows that scattering from small aggregates of small gold nanoparticles can sufficiently explain the observed scattering spectra.

Combining all of the analyses, we determined a model for the growth of the gold nanoparticles on phospholipid vesicles (Figure 5.10). The positively charged nitrogen molecule at the end of the headgroup of a DOPC molecule serves as a nucleation site for the gold precursor $[AuCl4]^-$. In the anionic GUVs the charged lipids lead to a negative surface charge of the vesicles, hindering nucleation through electrostatic repulsion. The neutral GUVs are actually not neutral, but possess a slightly negative surface charge in the sucrose solutions used in these experiments. Thus, while the nucleation is also slightly hindered as in the anionic GUVs, the hindrance is not as high. Because of the hindrance in nucleation, there are less growth seeds on the anionic than neutral GUVs. If the concentration of the gold precursor is kept constant, then the seeds on the anionic GUVs will grow faster and become larger,
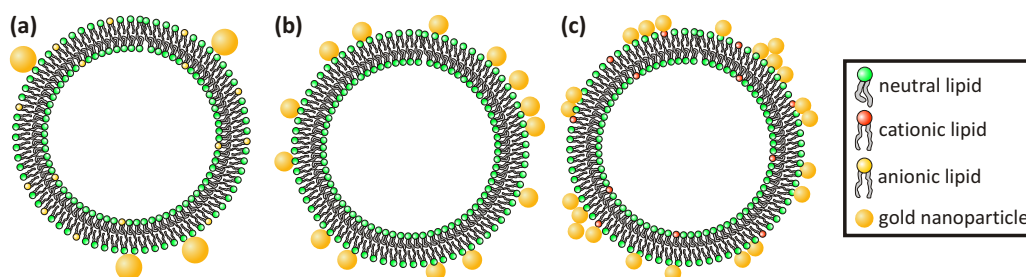
Figure 5.10 | Diagram of the gold nanoparticle growth process on phospholipid vesicles.
(a) The anionic phospholipids hinder the nucleation of the gold precursor and thus fewer, but larger nanoparticles are created with respect to (b) undoped DOPC vesicles. (c) Cationic lipids have the reverse effect, leading to many more, albeit smaller nanoparticles and nano-aggregates.

because more precursor material aggregates per site. For the cationic doped GUVs the process is reversed. Here, the net charge of the GUVs is positive, increasing the amount growth seeds for the gold nanoparticles. The same amount of gold precursor in the solution will thus result in more, albeit smaller, nanoparticles on the cationic GUVs. Aggregation of the nanoparticles can occur in all samples, because there is no molecule on the surface of the gold nanoparticles preventing aggregation. As has been shown previously, nanoparticles attached to fluid phase vesicles deform the membrane, leading to an inter-particle attraction. The nanoparticles consequently

tend to aggregate together when the possibility arises [170]. The degree of aggregation is controlled by the nanoparticles density, which is highest for the cationic GUVs and lowest for the anionic GUVs.

In conclusion, the method established here shows great promise as a rapid method for controlled loading of gold nanoparticles onto phospholipid vesicles. The method is biocompatible because none of the substances used in the growth process are cytotoxic. Changing the concentration of the gold precursor and doping the phospholipid vesicles with controlled amounts of charged phospholipids enables the control over gold nanoparticle size and density as well as the degree of aggregation of the nanoparticles. Negatively charged lipids promote the formation of larger, isolated nanoparticles, while positively charged lipids promote the growth of smaller nanoparticles, which form larger aggregates. The high degree of control is novel and of fundamental importance for the function of loaded vesicles. This renders the system useful not only as a model system for studying membrane-gold nanoparticle interactions, but also as a biomolecular tool. Amongst the many potential applications for these phospholipid-gold hybrid structures are controlled diffusion across a cellular membrane through optical heating of the gold nanoparticles and localized photochemistry facilitated through enhanced electrical fields [152,171,172].

5.3 Optical Heating of Gold Nanoparticles Attached to Phospholipid Membranes

In the last two sections we demonstrated how to attach gold nanoparticles to phospholipid vesicles, while controlling the size and density of the attached nanoparticles. The next step towards producing nanoscopic tools for membrane investigations and manipulations is the study of how to optically heat these nanoparticles and their effect on the phospholipid membranes. To do this, we grew DOPC GUVs, doping them with a dye-labeled phospholipid in order to see the membrane more clearly. CTAB-coated $40\,\mathrm{nm}$ large gold nanoparticles were attached to the GUVs and the sample, deposited onto a normal glass coverslip, was inserted into the dark

field microscope. Illumination occurred with a laser at $532\,\text{nm}$ wavelength. The laser spot was focused down to approximately $1.5\,\mu\text{m}$ in diameter and the power density of the laser set to $300\,\text{kW/cm}^2$. The laser beam was then focused onto one of the gold nanoparticles, which diffuse freely over the surface of the GUV. The GUVs were destroyed almost instantaneously. Depending on the position of the GUV with respect to the glass surface, two processes could be observed. If the GUV was far from the surface of the glass, it collapsed and formed a clump of fluorescent phospholipids and gold nanoparticles (Figure 5.11). Irradiating a GUV
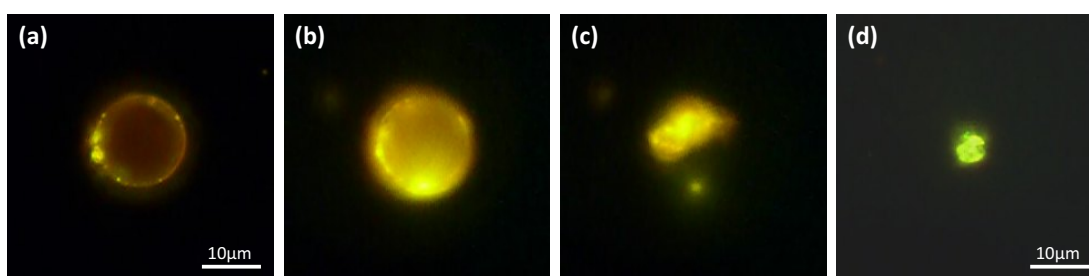
Figure 5.11 | Phospholipid vesicle destroyed through optical heating of gold nanoparticles. Dark field images of (a) a vesicle with attached $40\,\text{nm}$ gold nanoparticles. The membrane is stained with a dye in order for the membrane to be more clearly seen . (b) The same vesicle during heating, (c) shortly after destruction and (d) the residual clump of fluorescent phospholipids and gold nanoparticles. The entire rupture process happens within two frames, that is in under $67\,\text{ms}$.

in the proximity of the glass surface resulted in a different behavior. While the GUVs were also destroyed, the membranes in this case spread out over the surface of the coverslip with the gold nanoparticles still attached (Figure 5.12). The radius of the membrane on the glass surface is twice that of the GUV before rupturing, confirming that the entire phospholipid membrane was spread out as a single bilayer over the surface. This behavior can also be observed when the laser is switched off, as GUVs can spontaneously adhere to the glass surface[173,174]. However, the vesicles that were irradiated with laser light tended to adhere within a few tens of seconds, whereas without the laser light this process took much longer. Illuminating the gold nanoparticles on the GUV surface thus facilitates the adhesion process. Whether this is due to an optical force exerted on the system, or through destabilization of the membrane, is not known.
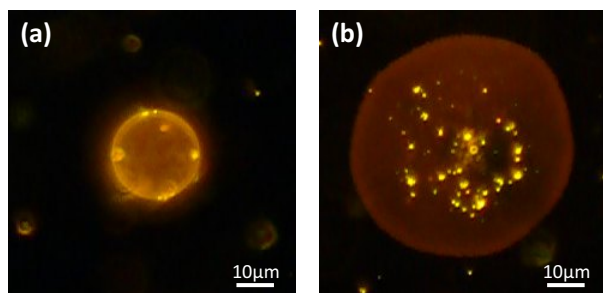
Figure 5.12 | Phospholipid vesicle destroyed through optical heating of gold nanoparticles. (a) In the vicinity of the glass coverslip a GUV is destroyed. (b) Its membrane spreads out over the glass surface, forming a single phospholipid bilayer with attached gold nanoparticles.

GUVs consisting of phospholipids with a main transition temperature above room temperature, e.g. DMPC or *DPPC (1,2-dipalmitoyl-sn-glycero-3-phosphocholine)*, showed a different behavior than DOPC vesicles, which were in the fluid phase at room temperature. At identical heating conditions, smaller vesicles started to bud off DMPC and DPPC vesicles and attach to the main membrane. Some of them split off and spread through the surrounding solution. The vesicles shrunk considerably in size, which means that a large fraction of the solution inside the vesicles was released into the surrounding solution. This process occurred over a matter of minutes, much longer than the rapid destruction of the DOPC vesicles. The reason for the different behavior lies in the mechanical properties of the two membrane phases. The fluid phase vesicle is very flexible and collapses almost instantly. The gel phase vesicle is much more rigid and only those parts that are directly heated are affected and bend, forming satellite vesicles. The rest of the vesicle bends slowly and reattaches, closing created pores.

To clarify the role of the gold nanoparticles, several control experiments were conducted. DOPC vesicles without attached gold nanoparticles were illuminated. The vesicles neither changed shape nor were they destroyed even for much higher laser power densities (up to $10\,\text{MW/cm}^2$). The gold nanoparticle coated GUVs were also illuminated at a wavelength far from the plasmon resonance of the gold nanoparticles. Using the same laser power density and a wavelength of $633\,\text{nm}$, no change of the GUV could be observed either. These results suggest that the destruction of the DOPC vesicles is a result of temperature increase produced by the gold nanoparticle. Calculations were performed to estimate the temperature increase in the system for the control experiments. The temperature increase in the membranes is negligible in both cases due to the weak absorption of the

membrane and of the gold nanoparticles at off-resonant wavelengths. On the other hand, gold nanoparticles illuminated at $532\,\mathrm{nm}$ with $P = 300\,\mathrm{kW/cm^2}$ heat up to $175\,^\circ\mathrm{C}$. At these temperatures formation of bubbles of water vapor has already been observed[175] (threshold value approximately $136\,^\circ\mathrm{C}$). These bubbles could easily disrupt the membrane and cause the collapse of a GUV in the fluid phase.

While the ability to destroy phospholipid vesicles carries great promise for applications in drug delivery, several interesting uses for gold nanoparticles could be explored by heating gold nanoparticles in a controlled manner to more moderate temperatures. The gel phase vesicles showed interesting shape changes upon localized heating of gold nanoparticles and were therefore chosen for the next set of experiments. We attached $80\,\mathrm{nm}$ CTAB-coated gold nanoparticles to DPPC vesicles, having a melting temperature of $T_m = 41\,^\circ\mathrm{C}$. The GUVs were prepared in a $300\,\mathrm{mM}$ sucrose solution and diluted 1:1 with a $300\,\mathrm{mM}$ glucose solution. Due to the different densities of the two sugars ($\rho_{suc} = 1.59\,\mathrm{g\,cm^{-3}}$ and $\rho_{gluc} = 1.54\,\mathrm{g\,cm^{-3}}$) the vesicles sank to the surface of the glass coverslip. These were coated with a layer of PDADMAC (section 3.2.3) to prevent the vesicles from being destroyed on the glass surface and also to immobilize the vesicles. Each vesicle had between three and ten gold nanoparticles attached to the membrane. The DPPC vesicles were generally highly faceted and the gold nanoparticles were immobile on the surface of the GUVs. The laser beam was expanded to a spot size of $10\,\mathrm{\mu m}$ *full width at half maximum (FWHM)* enabling the illumination of an entire GUV. At a laser power density of $120\,\mathrm{kW/cm^2}$ the gold nanoparticles began to diffuse along the vesicle membrane and the vesicle itself changed its shape rapidly, becoming spherical within several seconds (Figure 5.13). After the beam was switched off, the vesicle remained in the same spherical shape and the gold nanoparticles once again became immobile.

In order to understand the light-induced heat deposition and the behavior of the system, we simulated the heat transfer by finite-element calculations, as explained in section 2.1.2.2. These calculations require the absorption cross section of the gold nanoparticles, the laser power density, the geometry of the vesicle-nanoparticle system, as well as the thermal capacity and thermal conductivity of all components. Because the gold nanoparticles are coated with CTAB, which charges the surface
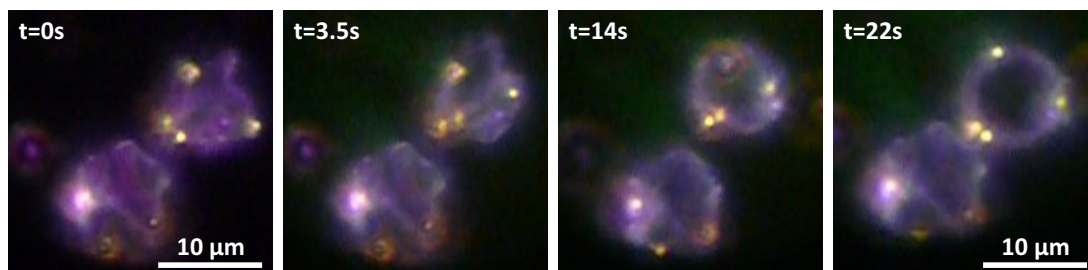
Figure 5.13 | Shape change of a DPPC vesicle upon laser illumination. The GUVs are coated with $80\,\text{nm}$ gold nanoparticles. The vesicle on the top right is illuminated at $532\,\text{nm}$ with a power density of $120\,\text{kW/cm}^2$. The vesicle changes its shape rapidly upon illumination and retains its spherical shape after the laser is turned off.

and changes the optical properties, it is not possible to calculate the absorption cross section of the gold nanoparticles directly. To obtain values as accurately as possible, we first measured the scattering spectrum of the gold nanoparticles in the dark field microscope. These were used as a reference to compare with the calculated scattering spectrum. The parameters in the simulation were varied to obtain the optimal fit between the measured and calculated scattering spectra (Figure 5.14a). With these parameters the absorption spectrum was calculated and
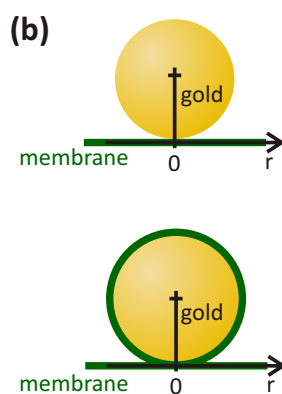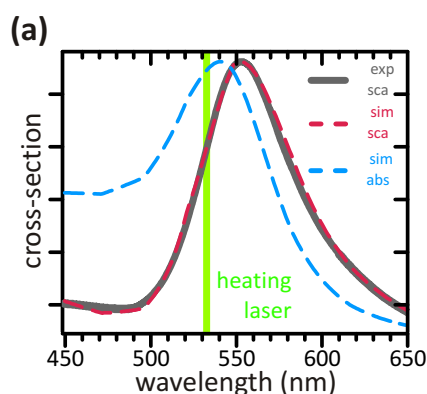
Figure 5.14 | Temperature simulations for optically heated gold nanoparticles on GUVs. (a) The absorption cross section (σ_{abs}^{sim}) of the gold nanoparticles is determined by fitting measured scattering spectra (σ_{sca}^{exp}) to calculations (σ_{sca}^{sim}). (b) Whether the gold nanoparticle is fully wrapped by the membrane or not is not known.

should then be a very good approximation of the actual absorption spectrum. The laser power was measured on the sample and, together with the spot size measured vai images of the laser spot reflection at the glass surface, yields the power density of the laser. The thermal constants of gold and the surrounding solution are well

known, but not of phospholipids. Estimates were taken from the literature, using the molecular weight and space requirements for phospholipid molecules to obtain a density of $0.775\,\mathrm{g\,cm^{-3}}$. Calorimeter measurements [176,177] give values for the thermal conductivity, $\kappa = 0.17\,\mathrm{W\,m^{-1}K^{-1}}$, and heat capacity, $c_p = 2115.95\,\mathrm{J\,kg^{-1}K^{-1}}$. The parameters were varied by an order of magnitude, showing that the thermal properties of the membrane have only little effect on the temperature distribution and temporal development. The maximum difference in the temperatures occurs in the proximity of the nanoparticle and never exceeds 8%. Thus, even though the precise values are not known, any errors will have only a negligible influence on the simulations. Establishing the precise geometry of the system is slightly more complicated. As stated in section 5.1, it is unclear to what extent the membrane bends around the CTAB-coated gold nanoparticle. For this reason, we simulated both extremes: a gold nanoparticle on a flat membrane and a fully wrapped gold nanoparticle (Figure 5.14b). The degree of wrapping around the membrane was found to have only a minuscule influence on the system, affecting only the kinetics of the heating process. A fully wrapped membrane increases the time for the nanoparticle to reach thermal equilibrium, due to the low thermal conductivity of the phospholipids. However, as this also occurs on the nanosecond scale for a fully wrapped gold nanoparticle, the geometry is insignificant for the simulations. Illumination with the heating laser results in highly localized temperatures that can easily reach over $100\,°\mathrm{C}$. This does not lead to problems, as, in nanosized regions, water can be heated above this temperature without boiling [178]. The temperature maximum is directly below the gold nanoparticle and falls off sharply with increasing distance from the nanoparticle (Figure 5.15). The temperature in a gel phase membrane can easily be raised above the main transition temperature, melting the membrane, by increasing the laser power density. The resulting fluid phase is centered around the gold nanoparticle with the radius (R_f in Figure 5.15b) reaching a few hundred nanometers. The size of the fluid phase increases with increasing laser power density.

In the experiment described previously, where the DPPC vesicles underwent a significant shape change, the maximum temperature in the membrane was $71\,°\mathrm{C}$. Because this is above the melting temperature of DPPC, parts of the vesicle
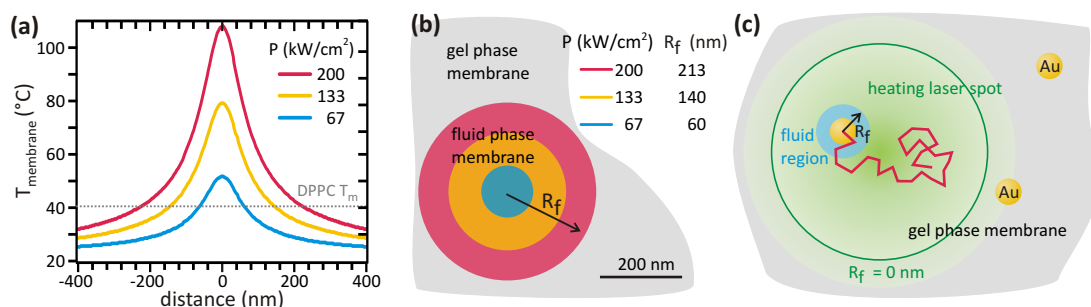
Figure 5.15 | Temperature profiles in phospholipid membranes underneath optically heated gold nanoparticles. (a) Depending on the laser power density, the temperature in the phospholipid membrane can be raised above the main transition temperature. (b) A fluid phase underneath the nanoparticle is confined to a nanosized region that increases in size with higher laser power densities. (c) The heated nanoparticle can diffuse through the fluid phase around it and, as it does so, it melts new regions of the membrane.

membrane are heated above the transition temperature and enter the fluid phase. In this phase, the membrane is more flexible and can bend to assume the energetically most favorable state. The fluid phase is confined to regions around the nanoparticle approximately $122\,\text{nm}$ in radius, not large enough to extend through the entire vesicle. To induce the observed shape change, energy must be transported through the lateral diffusion of phospholipids within the membrane, which occurs up to a factor of 10^3 faster in the fluid phase than in the gel phase. The increased lateral mobility of the phospholipids also enables the gold nanoparticles to diffuse along the membrane. The gold nanoparticles bind strongly to the membrane because of the CTAB-coating and are immobile due to the low phospholipid mobility in the gel phase. The illuminated gold nanoparticles can melt a membrane region of radius R_f around them. Within this fluid phase the gold nanoparticle can diffuse; and as it does so, it melts its new surroundings. As soon as the laser is switched off, the membrane cools back to a temperature below the main transition temperature. The lipids lose their mobility and the gold nanoparticles become immobile again.

These experiments prove it is possible to heat single GUVs in a controlled manner without destroying them and to induce a localized melting of the phospholipid membrane. The next important step is to examine single nanoparticles and determine how they interact individually with the phospholipid membranes when

heated optically. To accomplish this, CTAB-modified gold nanoparticles were again attached to DPPC vesicles. The concentration of the nanoparticles was reduced, so that only between one and five nanoparticles were on a vesicle at a time. By further reducing the spot size of the laser to about $9\,\mu$m, one can ensure that only a single nanoparticle is heated . Illuminating the gold nanoparticles at low laser power densities produced no effect; the nanoparticles remained immobile on the vesicle surface. At a certain laser power the nanoparticles started to diffuse through the membrane. When the laser was turned off, the diffusion stopped instantly and started again as soon as the laser was switched on. Increasing the laser power density even further led to a faster nanoparticle diffusion.

The nanoparticle motion was not homogeneous within the confines of the laser spot. In the center of the beam the nanoparticles diffused faster than further from the center. This is due to the Gaussian beam profile of the laser. The laser spot has its maximum intensity in the center and the intensity decreases outwards. Thus, the maximum temperature that the membrane reaches is dependent on the position of the gold nanoparticle within the laser spot (Figure 5.15c). Far enough from the center, the maximum temperature is below the main transition temperature. From this point outwards, the gold nanoparticle is no longer able to melt the membrane. The distance at which $R_f = 0$ is indicated by the green circle. The other nanoparticles on the membrane remain immobile during the entire experiment.

To analyze the mobility of gold nanoparticles on phospholipid membranes upon illumination with laser light, we recorded the diffusion on video. Analyzing the position of the nanoparticle as it moves over the membrane can yield the diffusion coefficient, D, of the nanoparticle, a measure of the mobility. The motion itself is studied by *single particle tracking (SPT)*. With this technique it is not necessary to observe a large number of nanoparticles and record their movement in order to obtain high statistical accuracy. Instead, a single nanoparticle track can be used to obtain accurate values of the diffusion coefficient, D. This track typically consists of between 20 and 2000 position measurements[179]. The length of the track depends on the definition of the diffusion coefficient. There are short- and long-range diffusion coefficients that are distinct, except in the case of unobstructed

diffusion. SPT measurements typically determine a short-range D over distances of tens of nanometers. This helps to obtain a value that is independent from directed motion, obstacles or corral boundaries. However, SPT also has the ability to resolve modes of motion of individual molecules. Several modes of motion can be observed: immobile, directed, confined, tethered, normal diffusion and anomalous diffusion. In order to reduce the noise in an experimental trajectory, the data points from a single trajectory are averaged, yielding the *mean-square displacement* ($MSD = \langle r^2 \rangle$) for this trajectory. In an average of an ensemble the time dependence of the MSD for these modes of motion is very different, so that the motion can be classified easily [180]. The MSD is directly related to the diffusion coefficient and is given for the different modes of n-dimensional motion:

$$\text{normal diffusion: } : \langle r^2 \rangle = 2nDt \tag{5.1a}$$

$$\text{anomalous diffusion: } : \langle r^2 \rangle = 2nDt^{\alpha} \tag{5.1b}$$

$$\text{directed motion with diffusion: } : \langle r^2 \rangle = 2nDt + (vt)^2 \tag{5.1c}$$

$$\text{corraled diffusion: } : \langle r^2 \rangle \cong \langle r_c^2 \rangle \left[1 - A_1 e^{\left(-2nA_2 Dt / \langle r_c^2 \rangle \right)} \right] \tag{5.1d}$$

with the dimension of the system, n, the diffusion coefficient, D, a critical exponent, $\alpha < 1$, the velocity of the guided motion, v, the corral size, $\langle r_c^2 \rangle$, and constants, A_1 and A_2, determined by the corral geometry. In general, there are two ways to calculate the MSD for a given time delay, Δt. One either averages over all pairs of points Δt time steps apart (Figure 5.16a) or over independent pairs of points Δt time steps apart (Figure 5.16b). The average over all pairs has a slightly better signal-to-noise ratio and was used in this thesis. The MSD can consequently be calculated
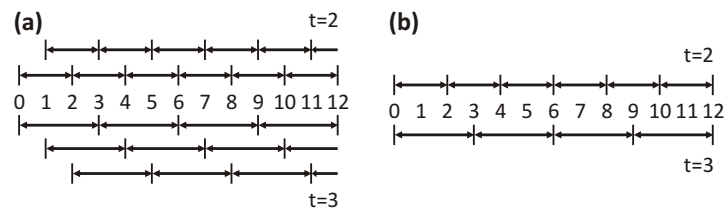
Figure 5.16 | Calculation of the mean-square displacement (MSD). Patterns of sampling for (a) averages over all pairs and (b) averages over independent pairs of trajectory points for a time delay Δt.

from the positions of the nanoparticle, $\vec{r}(t)$, and the number of points in the track, N_A, via:

$$MSD(\Delta t) = \left\langle r^2(\Delta t) \right\rangle_A = \frac{1}{N_A} \sum_{i=0}^{N_A-1} [\vec{r}(t+\Delta t) - \vec{r}(t)]^2 \qquad (5.2)$$

The camera used for recording the movement has a frame rate of 30 frames per second. An analysis program was written with the software Igor Pro to automatically load the individual frames of the video, and find and record the positions of the nanoparticles. These traces were then used to calculate the MSD, which in turn was used to determine the diffusion coefficient of the nanoparticles. In order to minimize the noise in the measurements, only immobile vesicles, having at least three nanoparticles attached to the membrane, were used for the measurements. This way one nanoparticle can be heated and diffuses, while the two immobile nanoparticles are used as a reference to remove background noise resulting from jitter of the experimental setup and errors in the image acquisition. The average of their movement is taken after every frame and this movement is subtracted from the movement of the heated nanoparticle.

A highly faceted DPPC vesicle with three attached gold nanoparticles used for measurements is shown in Figure 5.17a. Overlaying the image are traces from the heated (red trace) and reference (light blue traces) nanoparticles. The green circles show the radius of the fluid phase, R_f, below the nanoparticle, which, due to the Gaussian profile of the laser beam, is dependent on the nanoparticle position within the laser spot. R_f decreases outwards from the beam center until, when $R_f = 0$, the laser power density is insufficient to induce a phase change in the membrane. As can be seen in Figure 5.17b, the MSD is linear in time, characteristic for free random diffusion within the corral imposed by the heating spot. Because this movement occurs in two dimensions, the diffusion coefficient is given by: $D = \frac{MSD(t)}{4t}$. Increasing the power density of the laser leads to an increased diffusion of the nanoparticles. This can be seen as an increase in the slope of MSD. However, for longer measurement times, the gold nanoparticles sometimes exhibit a sub-diffusive behavior. At higher laser power densities ($P_{max} > 265\,\text{kW/cm}^2$ - the maximum power density at the center of the Gaussian beam) the nanoparticles diffuse so fast

that they reach the limits of the diffusion corral within the observation time. Here the gold nanoparticle movement is reduced due to the low laser power density.
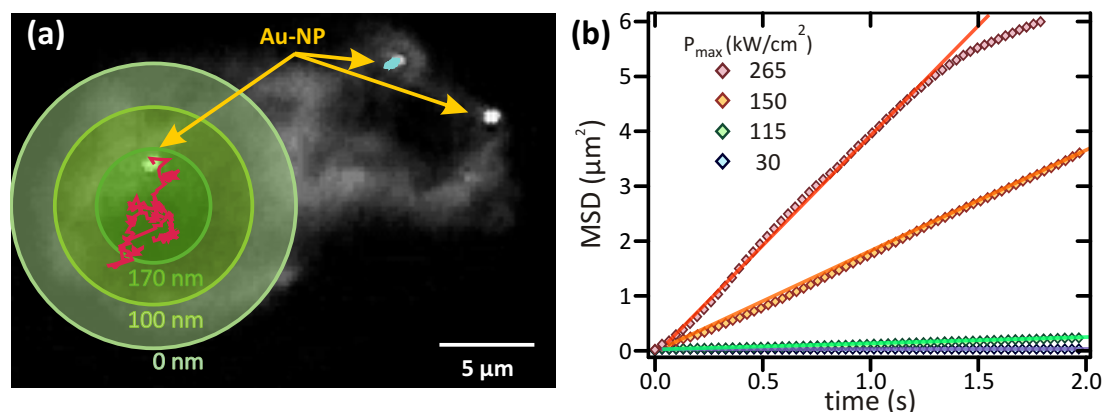
Figure 5.17 | Measurements of a heated gold nanoparticle's *MSD*. (a) Dark field image of a DPPC vesicle with three attached gold nanoparticles. The red trajectory is that of the heated nanoparticle, while the reference trajectory is shown in light blue. The green circles denote the maximum radius of the fluid phase underneath the gold nanoparticle, when it is at that distance from the center of the laser spot. (b) Plots of the MSD for gold nanoparticles illuminated at increasing power densities. The MSD is linear, denoting free random diffusion, except for the highest power densities (red curve). Here, the nanoparticle moved further away from the beam center, where it slowed down due to the reduced laser power.

The measurements conducted here lead to a diffusion coefficient, which is dependent on laser power density. To investigate the validity of the experiments, we designed a Monte-Carlo simulation, reproducing the experimental setup (Figure 5.18). The program simulates a random walk in two dimensions. There are several parameters determining the random walk, all of which have a distinct effect on the simulation. The *average step size* and the *time between steps* directly affect the diffusion coefficient and were set to reproduce the measured values of D. The *sample period*, i.e. the time interval between measurements is the $33\,\mathrm{ms}$ frame rate of the digital camera. Even though the diffusion occurs on a much shorter time scale (probably on the nanosecond time scale, as the lipids exchange places at this rate), for long traces the sample period does not have a large effect on the measured diffusion. The simulation helps to explain one phenomenon seen in measurements for gold nanoparticles with very small diffusion coefficients. In these measurements, the MSD shows a deviation from a purely linear dependence. The values are linear in

all but in the first point, and a fit of the data leads to an axis intercept that does not coincide with the origin (Figure 5.18c). This is caused by the limited resolution of the camera, leading to a fixed error, which depends on the magnification. For small values of the MSD this error can be clearly seen, but not for gold nanoparticles diffusing rapidly. We also simulated this in the Monte-Carlo simulations, by adding a large noise component to the sampling trace (Figure 5.18a). Comparing the resulting MSD with the one obtained without the resolution error, we find the slopes are the same, if one omits the first point. In summary, the Monte-Carlo simulation show that the values we obtained from the experiments were valid and accurately describe the physical situation.
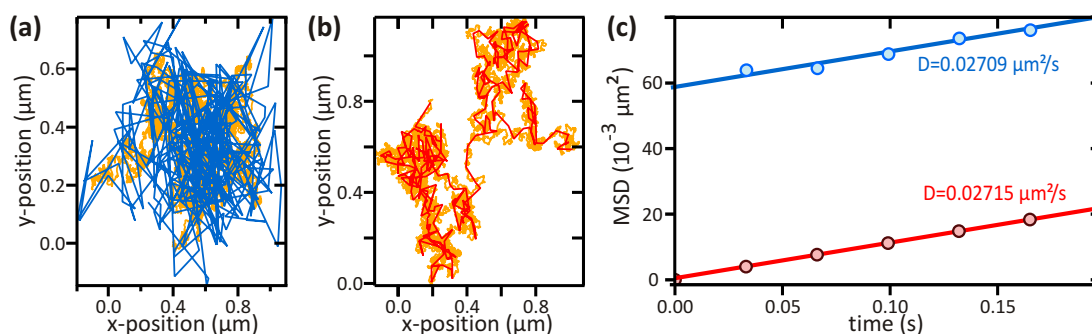
Figure 5.18 | Monte Carlo simulations of a 2-D random walk. (a,b) The nanoparticle diffusion is simulated and displayed as a trajectory (yellow). The sampling by the camera every $33\,\mathrm{ms}$ is then accounted for, both with a large resolution error (a, blue trajectory) and with a small resolution error (b, red trajectory). (c) The MSD is calculated and in both cases results in the same diffusion constant D.

The next experiments were designed to study in detail the diffusion of optically heated gold nanoparticles on phospholipid membranes. We began with measurements on GUVs consisting of DOPC phospholipids, which are in the fluid phase at room temperature. These vesicles serve as a control measurement, so that the influence of temperature on the diffusion of gold nanoparticles in the fluid phase can be investigated. For the experiments, CTAB-coated gold nanoparticles were attached as described previously to DOPC vesicles. Because the nanoparticles were in constant motion, there was no possibility of measuring reference particles simultaneously. Instead, as a reference, the gold nanoparticle diffusion is measured

without the laser. We measured the diffusion of more than ten nanoparticles, with observation times between 30 seconds and several minutes per nanoparticle. For gold nanoparticles affixed to DOPC vesicles at a temperature of $20\,°C$ we determine a value of $D = 0.23\,\mu m^2/s$. This corresponds well to values reported previously, both in measurements of lipid tagged gold nanoparticles in artificial bilayers[181] and in biological membranes[182]. The GUVs were illuminated with the laser at $532\,nm$ wavelength, using a spot size of around $9\,\mu m$ (FWHM) and varying the power density up to $200\,kW/cm^2$ (Figure 5.19b). The diffusion coefficient increases exponentially with increasing laser power density P_{max}. This behavior is easy to
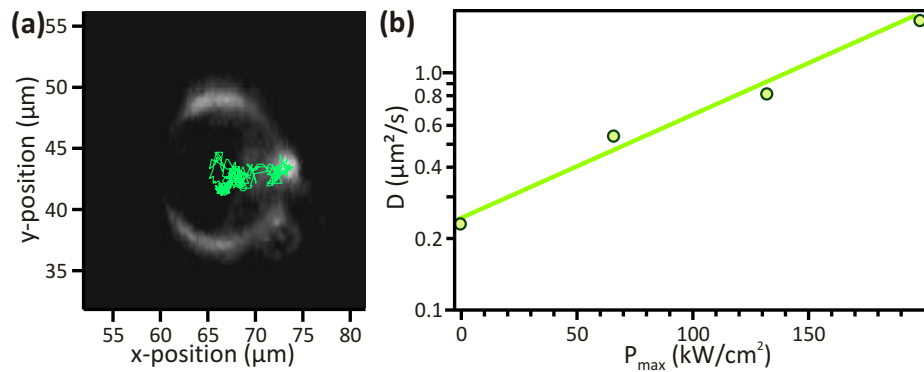
Figure 5.19 | Diffusion of optically heated gold nanoparticles on DOPC vesicles. (a) Dark field image of a DOPC vesicle with attached gold nanoparticle, whose 16 second long trajectory is superimposed in green. (b) Dependence of the gold nanoparticles diffusion coefficients on laser power density.

explain. In three dimensions the diffusion coefficient of a particle in a solution is given by the *Einstein-Stokes equation*:

$$D(T) = \frac{k_B T}{6\pi\eta(T)r} \tag{5.3}$$

with the Boltzmann constant, k_B, the temperature, T, the viscosity of the surrounding medium, $\eta(T)$, and the radius of the particle, r. The DOPC membrane can be seen as a two-dimensional fluid and, as such, its viscosity is temperature-dependent according to:

$$\eta(T) = \eta_0 e^{-bT} \tag{5.4}$$

As shown in equation 2.27 the maximum temperature of the gold nanoparticles increases linearly with P_{max}. Thus, T can be replaced in the equations with P_{max}, resulting in a dependence of the diffusion coefficient on the laser power density according to: $D \propto P_{max}e^{P_{max}}$. This behavior is seen in the measurements (Figure 5.19b) and validates the model of a the fluid phase membrane as a viscous liquid.

The next measurements focused on the diffusion of gold nanoparticle attached to gel phase GUVs. For this we grew vesicles consisting of DPPC and attached $80\,\text{nm}$ CTAB-coated gold nanoparticles to them. All analyzed vesicles had at least three gold nanoparticles attached to them, enabling reference measurements. For low laser power densities ($P_{max} < 71\,\text{kW/cm}^2$) no movement of the irradiated gold nanoparticles was detectable, just as for the reference nanoparticles (Figure 5.20).
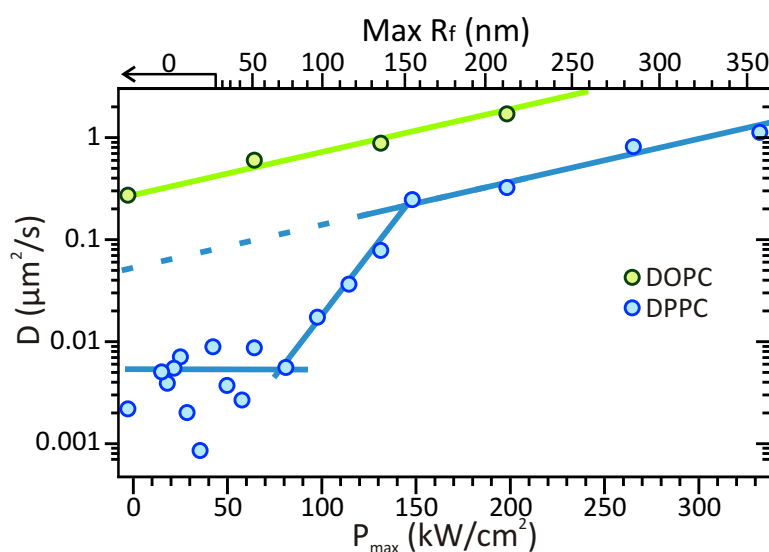
Figure 5.20 | Diffusion of optically heated gold nanoparticles on DPPC vesicles. Dependence of the gold nanoparticles diffusion coefficients on laser power density. In contrast to the simple exponential dependence of D on the power density for DOPC vesicles, the diffusion shows three distinct regions for DPPC vesicles.

The large scatter in the data is exaggerated by the logarithmic plot of the values of the diffusion coefficient and is due to the experimental error of $150\,\text{nm}$ in the localization of the nanoparticles. When the power density was increased above

$71\,\mathrm{kW/cm}^2$, the nanoparticles started to diffuse along the membrane. The diffusion increased with increasing laser power density. However the increase is split into two distinct regions. For P_{max} between $71\,\mathrm{kW/cm}^2$ and $148\,\mathrm{kW/cm}^2$, there is an exponential increase with a very large slope. For $P_{max} > 148\,\mathrm{kW/cm}^2$, the increase still occurs exponentially, although at a much reduced rate. Extrapolating the slope for the high laser power density region towards lower values, it becomes clear that the slope here is the same as that of the nanoparticle diffusion on DOPC membranes.

As shown in Figure 5.15, the laser power density can be used to calculate the radius of the fluid phase, R_f, beneath the nanoparticle. The corresponding values of R_f for DPPC vesicles are given in the top horizontal axis in Figure 5.20. Clearly, the phase transition from the gel phase to the fluid phase determines the diffusion behavior of the gold nanoparticles. No diffusion occurs until R_f reaches a certain size (here: $R_f = 58\,\mathrm{nm}$). This value is only 1.5 times the size of the gold nanoparticle itself. Whether this is actually the size of the fluid phase that the gold nanoparticles require for diffusion or, more likely, that this is the value at which the motion can be first detected, cannot be determined clearly. To clarify this point, both a higher spatial as well as a higher temporal resolution would be required. The diffusion is similar to that on the DOPC membranes when the fluid phase reaches $R_f = 151\,\mathrm{nm}$.

To understand the diffusion process in better detail, we repeated the measurements for a third phospholipid that is identical in structure to DPPC, except that it has one more methylene group in the aliphatic chains, *1,2-diheptadecanoyl-sn-glycero-3-phosphocholine* ($DC_{17}PC$). It has a main transition temperature of $T_m = 48\,°\mathrm{C}$, slightly above that of DPPC. Conducting the measurements with the same parameters as for DPPC, the results were very similar (Figure 5.21a). The gold nanoparticles did not diffuse for low laser power densities, and began to diffuse at a slightly higher laser power density ($P > 92\,\mathrm{kW/cm}^2$) than the gold nanoparticles on the DPPC vesicles. The sharp bend in the increasing diffusion also occurred later for the $DC_{17}PC$ affixed gold nanoparticles, i.e. at $P = 177\,\mathrm{kW/cm}^2$. However, the slope in this intermediate regime is clearly less steep than that of the same regime in the DPPC vesicle measurements. The slope of the highest laser power regime is again the same as for the gold nanoparticles affixed either to the DPPC membrane

or to DOPC membranes. That the diffusion behavior is probably due to the gel-fluid phase transition in the phospholipid membranes is further confirmed by calculating the associated value of R_f at each of the bends in the two diffusion graphs. Using the values of the laser power densities for these four points (Figure 5.21a) allows the temperature profiles in the membranes below the gold nanoparticles to be calculated. The intersection of the membrane temperature profiles with the main transition temperatures gives the radius of the fluid phase. The intersections reveal that both for DPPC and $DC_{17}PC$ the diffusion begins for $R_f = 58$ nm (Figure 5.21b). This suggests that the gold nanoparticle must melt a certain region of the membrane in order to begin diffusing through the membrane.
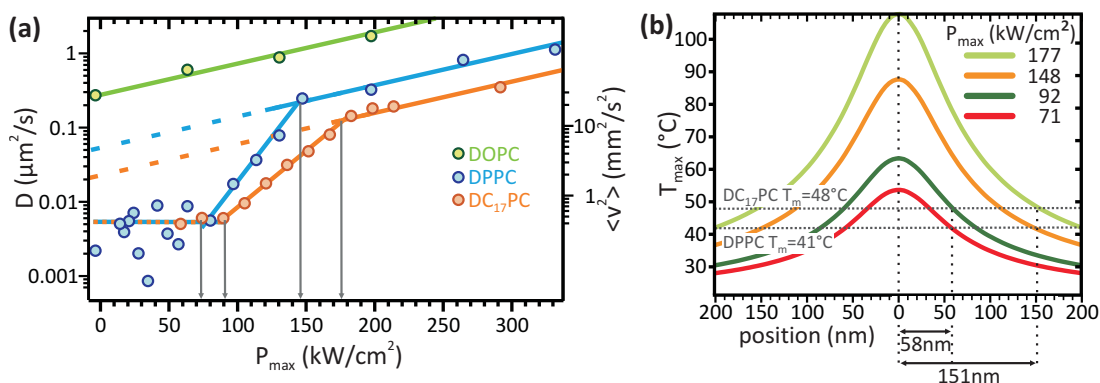
Figure 5.21 | Diffusion of optically heated gold nanoparticles on gel phase GUVs. (a) The diffusion of gold nanoparticles on gel phase membranes can be divided into three regions. A low power region, in which the nanoparticles do not diffuse, an intermediate power region, in which the nanoparticles melt the membrane around them and begin to diffuse and a high-power region in which the nanoparticles diffuse as in a normal fluid phase membrane. (b) The positions of the bends in the diffusion graphs (a, gray arrows) are determined by the size of the fluid phase below the gold nanoparticles, which are shown in (b).

Understanding the second break in the diffusion curve is slightly more difficult. Here, we must take the dynamics of the melting process into account. Even though the nanoparticle heats up the region of radius R_f on a sub-microsecond timescale, the actual phase transition may take considerably longer. Thus, a gold nanoparticle that melts its surrounding can diffuse within this region. Because of its temperature the nanoparticle's diffusion is very large, and the gold nanoparticle will come to the boundary of the fluid phase before the new region can also be melted. A

gold nanoparticles diffusion is restricted by the speed with which the fluid phase progresses through the gel phase membrane. This speed is directly obtained from the relationship: $\langle v^2 \rangle = D/\Delta t$ [183] and is shown as the right axis in Figure 5.21 for the gold nanoparticles on DPPC vesicles. From the measurements we determine velocities of the fluid phase front ranging between $0.9\,\mu$m/s and $4.5\,\mu$m/s. For P_{max} between $71\,$kW/cm^2 and $148\,$kW/cm^2 the gold nanoparticles diffusion is restricted due to the fluid phase front traversing the gel-phase. The much steeper slope here is due to the increase of the gold nanoparticles' motion and the simultaneous increase in the fluid phase front velocity. At a certain point, the fluid phase around the nanoparticles is generated so rapidly that they diffuse freely, just as the gold nanoparticles in the completely fluid membranes of the DOPC vesicles do. Thus the slopes for the diffusion curves on all three phospholipids reach the same value for the highest P_{max} intensities. The vertical offset of the curves in the laser power regime for a given value of P_{max} is due to the lower relative temperatures ($T_{rel} = T - T_m$) of DPPC and DC$_{17}$PC membranes. The relative temperature determines the viscosity of the phospholipid membrane. Therefore, at the same laser power density the DPPC membrane has a higher viscosity than the DOPC membrane, and the DC$_{17}$PC membrane has a higher viscosity still. The velocity with which the fluid phase propagates through the gel phase membrane could also explain why no nanoparticle diffusion is observed until the radius of the fluid phase reaches a value 1.5 times the size of the nanoparticle itself. For values of P_{max} that are just enough to melt the membrane the gold nanoparticle motion is probably restricted so much that the actual diffusion is not visible, until R$_f$ becomes larger than $58\,$nm.

With this knowledge of how the gold nanoparticles diffuse on phospholipid membranes as well as how this diffusion can be controlled, the potential of the nanoparticles can be enhanced further. An important first step is the positioning of the gold nanoparticles at specific locations on the membranes. This can be accomplished by harnessing the optical control of the local phase transition. As explained previously, the optically heated gold nanoparticles undergo a corralled diffusion. The corral is determined by the Gaussian shaped intensity profile of the laser beam. By reducing the laser spot in size, the corral within which the gold nanoparticle undergoes diffusion is also reduced in size. If the heating spot is

then displaced with a rate comparable to the time needed by the gold nanoparticle to explore the diffusion corral, the nanoparticle can be guided over the vesicle membrane (Figure 5.22). In the experiments, we again used DPPC vesicles with
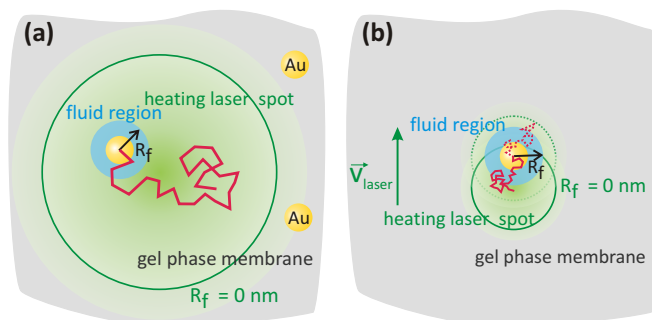
Figure 5.22 | Guiding gold nanoparticles on vesicle membranes. (a) Gold nanoparticles diffuse within the corral imposed by the Gaussian shaped heating laser. (b) By reducing the size of the laser spot, the corral within which the gold nanoparticles can diffuse is also reduced in size. If the heating spot is then displaced with a rate comparable to the time within which the gold nanoparticle explores the corral, the nanoparticle can be guided over the membrane.

at least three $80\,\mathrm{nm}$ gold nanoparticles attached to them. As before, only one nanoparticle at a time was heated, while the other gold nanoparticles were used as reference nanoparticles. The laser spot size was reduced from a FWHM of around $9\,\mu\mathrm{m}$ to only $0.9\,\mu\mathrm{m}$. This confines the lateral motion to a very small region imposed by the heating laser. The laser was displaced at a slow, constant rate in a single direction (Figure 5.23a). The irradiated gold nanoparticle followed the laser spot (Figure 5.23b, red trajectory) while the other nanoparticles remained immobile (blue trajectories). As can be seen from the trajectory, the gold nanoparticle did not move in a straight line; instead the guided motion and the diffusion within the confines of the corral were superimposed. This can be seen clearly when the MSD of the heated gold nanoparticle is calculated and plotted over time (Figure 5.24a). Here, the behavior deviates clearly from the linear behavior of normal diffusion. This is to be expected, as the MSD for purely guided motion is given by: $MSD(t) = v^2t^2$, and therefore is proportional to the square in time. In our case, guided motion and normal diffusion within the laser corral are superimposed and thus can be calculated by $MSD(t) = 4Dt + v^2t^2$. This is plotted in Figure 5.24a and yields values for the diffusion coefficient of the gold nanoparticle ($D = 0.10\mu m^2/s$) and also of the

guiding speed of the laser ($v = 1.18\mu m/s$). This speed must be kept below the fluid phase front velocity; otherwise the gold nanoparticle cannot melt the gel phase membrane fast enough and will be left behind.
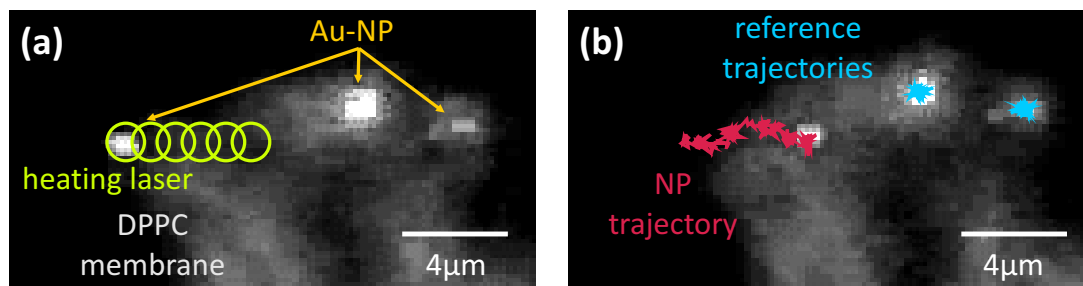
Figure 5.23 | A gold nanoparticle is guided over the membrane of a DPPC vesicle. (a) Three gold nanoparticles are attached to this DPPC vesicle. The lower one is illuminated with the laser, which is displaced at a constant rate upwards along the vesicle membrane. (b) The gold nanoparticle follows this path and moves upwards, while the reference nanoparticles do not move at all.

To understand exactly how the gold nanoparticles move in the fluid phase, we plotted the positions of the gold nanoparticle with respect to the laser spot for each frame of the recorded video (Figure 5.24b). The gold nanoparticle stayed mainly in the front half of the laser spot. It was expelled from the center of the heating spot by the optical forces[140] by the laser acting on it. The best results for optical guiding were achieved when focusing the laser slightly behind the gold nanoparticle and driving it from behind in the desired direction. As shown in chapter 4 (Figure 4.5), the sign of the radial force depends strongly upon the position along the axis of the beam for resonant excitation. A shift of only $170\,\text{nm}$ is sufficient to go from an attractive radial force to a repulsive force. The attractive force is not strong enough to overcome the thermally activated diffusion and enable guiding of the nanoparticles. The repulsive force on the other hand can drive the nanoparticles from behind through the vesicle membrane. Even though the gold nanoparticle diffused laterally within the limits imposed by the heating spot it was possible to position the nanoparticles on the membrane with a high precision. Reaching the desired position, the laser beam was widened to reduce the optical forces on the nanoparticle. By subsequently reducing

the laser power gradually the nanoparticle was progressively confined to a smaller region near the laser spot center.
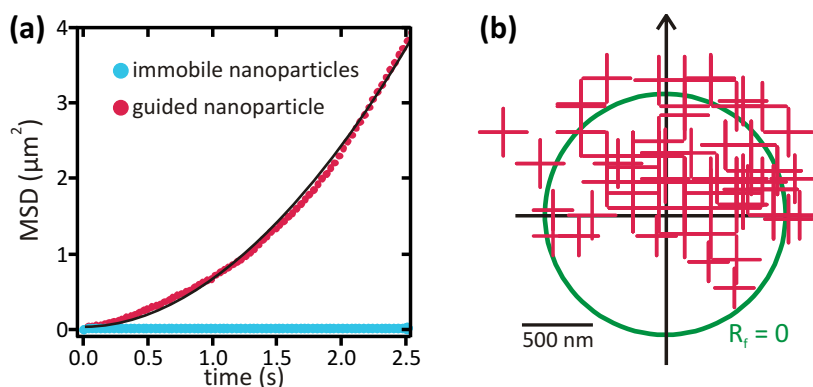
Figure 5.24 | Analysis of the guided diffusion of gold nanoparticles on DPPC membranes. (a) The mean-squared displacement of the guided nanoparticles shows a dependence on the square of time, characteristic of true guiding. (b) The gold nanoparticle (red crosses) mainly stays in front of the laser (axis origin) and is driven from behind by the optical forces exerted by the laser over the vesicle membrane.

5.4 Optical Injection of Gold Nanoparticles into Phospholipid Vesicles

Introducing substances into cells that are impermeable to the membrane, also known as *transfection*, is a big problem in cell biology. Most transfection techniques available are only capable of treating entire populations of cells simultaneously, and not single cells [184]. Since the first presentation of a so-called "gene-gun" [185], there have been a number of studies investigating possible mechanisms for single cell transfection, e.g. electroporation and optical-injection [186,187]. In the most recent work done by McDougall and colleagues, a technique was established using two lasers to optically inject gold nanoparticles into mammalian cells. One laser, used as an optical tweezer, brings the gold nanoparticle into position above the cell surface, and the second one illuminates the gold nanoparticle with femtosecond pulses, creating a transient pore in the membrane and pushing the nanoparticle through the pore. The details of this mechanism have not been characterized yet. We developed a

novel approach for perforating phospholipid membranes. The main goal of our approach is to use only one laser to accomplish all the steps required to inject single nanoparticles into cells.

Before using mammalian cells, we decided to work with giant unilamellar vesicles to study how it is possible to inject gold nanoparticles through a phospholipid membrane and how the process can be controlled. As explained in the previous chapter, a laser beam exerts a force on a nanoparticle, resulting from a scattering and a gradient force. The nanoparticles can be propelled at high speeds to specific locations with a high precision. To show this, we used $80\,nm$ gold nanoparticles, coated with a CTAB bilayer and DPPC vesicles, grown in a $300\,mM$ sucrose solution. These were mixed 1:1 with a glucose solution of identical concentration. The gold nanoparticles were then added to this solution and a drop placed onto a PDADMAC coated glass coverslip. The vesicles being more dense than the outside solution, sink to the surface and attach to the polyelectrolyte surface. We used the Millennia V laser focused to a spot size of $380\,nm$ (FWHM). The laser focus and optical focus planes lie close together. The laser can thus easily be focused on the vesicle membrane by bringing the vesicle membrane into focus in the microscope. A diagram of the setup is shown in Figure 5.25a.
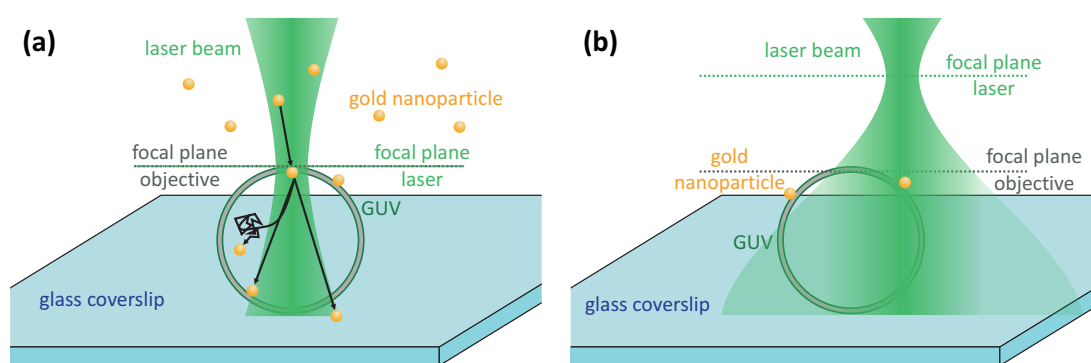
Figure 5.25 | Injecting gold nanoparticles into GUVs. (a) Diagram of the setup for printing gold nanoparticles selectively on phospholipid membranes. The laser is focused at the same plane as the microscope objective. (b) Diagram for the setup used to optically inject gold nanoparticles into phospholipid vesicles. The laser beam passes through a focusing lens before it enters the microscope objective, shifting the focal plane. This effectively widens the laser spot to a considerable extent.

At low laser powers the gold nanoparticles were accelerated by the laser towards the vesicle, but neither bound nor penetrated the membrane and diffused away through the solution. Increasing the laser power to a value around $60\,\mathrm{mW}$, the nanoparticles began to attach to the surface of the vesicle (Figure 5.26). This value is certainly far above the value necessary for gold nanoparticles to be printed onto the membranes. However, the low gold concentration in the solution which is needed to prevent the vesicles from being destroyed also significantly increases the time between printing events. Thus, one needs to increase the laser power and with it the capture volume for gold nanoparticles. Because of this, the nanoparticles not only bound to the membrane exactly at the center of the beam, as in the experiments in chapter 4, but also further away and at different heights along the membrane. Sometimes the gold nanoparticles could be seen to bind to the membrane and then diffuse along it, driven by the heating through the laser. This method is an interesting alternative for attaching gold nanoparticles to the surface of phospholipid vesicles.
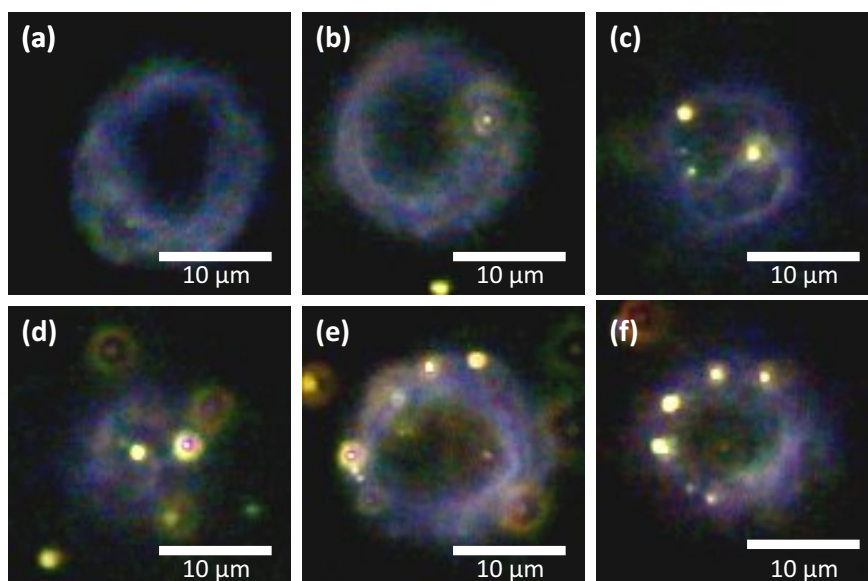
Figure 5.26 | Printing gold nanoparticles on phospholipid vesicles. (a) A DPPC vesicle without gold nanoparticles attached to the membrane is placed in the focus of a laser beam. (b-f) One after another gold nanoparticles are propelled towards the vesicle membrane, where they adhere to the surface of the membrane. The positions of the gold nanoparticles vary due to the high laser power.

Increasing the laser power even further ($P \approx 90\,\text{mW}$), nanoparticles not only attached to the membrane, but also began to perforate the vesicles. Perforation occurred for nanoparticles close to the beam center, while further away from the beam axis, nanoparticles were printed onto the vesicle membranes. Three different effects could be seen for perforating nanoparticles (Figure 5.25a). Most of the time, the nanoparticles were shot through the membrane and either stuck to the surface of the glass or to the side of the vesicle. In the latter case it is not clear, whether they remained on the inside of the vesicle or passed through it twice and stuck to the outside. It was also sometimes not possible to find the gold nanoparticles again after shooting them. This could have several reasons, e.g. the gold nanoparticles could be shot straight through the vesicles and escape into the solution again. The last effect that could be observed occurred less often than the others; the gold nanoparticles perforated the membrane and began to diffuse inside the vesicles. It was even possible to inject several nanoparticles into one vesicle. These diffused through the vesicle separately (Figure 5.27a) and sometimes escaped out of the vesicle again.
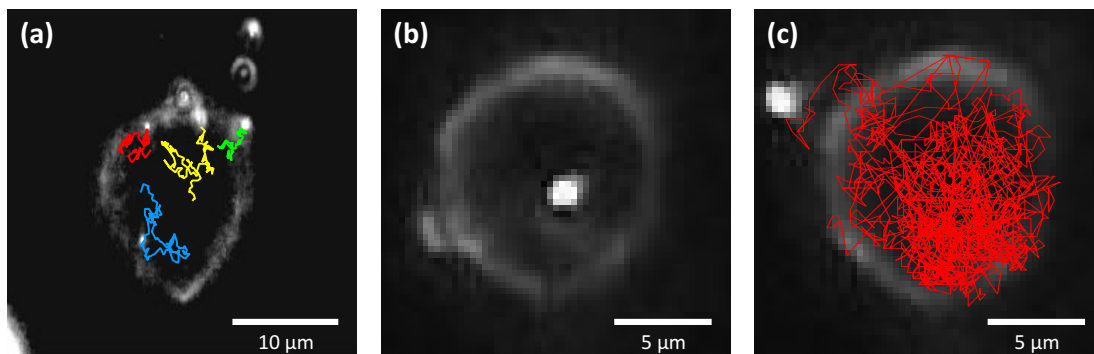
Figure 5.27 | Injecting gold nanoparticles into GUVs. (a) Multiple nanoparticles can be shot into one vesicle; and they diffuse around separately, as shown for these $4\,\text{sec}$ tracks. (b) A gold nanoparticle is attached to a DPPC vesicle. The nanoparticle is illuminated with the laser, penetrates the membrane and (c) begins to diffuse inside the vesicle. The nanoparticle remains inside the vesicle as can be seen by this $40\,\text{sec}$ track of the diffusing nanoparticle.

The laser powers used here were extremely high and it was nearly impossible to investigate the process happening during injection in detail. In order to do this, we decided to attach gold nanoparticles directly to the vesicle membranes and then analyze optical injection of these into the vesicles. The gold nanoparticles were

attached to the membrane, using the laser to catch the nanoparticles from the solution and induce binding to the membrane. We made sure that there were only a few, well separated gold nanoparticles on a vesicle to prevent them interacting with each other and also to reduce the stress on the phospholipid membrane. When focusing the laser on the gold nanoparticles attached to the membranes, the nanoparticles hardly ever perforated the membrane. The problem was that most often the nanoparticles rapidly diffused out of the laser focus. This was also seen in the experiments in section 5.3. To deal with this problem, we placed a focusing lens in the laser beam path in front of the microscope. The previously collimated beam hits the microscope at an angle and is thus focused at a point in front of the normal focal plane. At the optical focal plane of the objective, the beam is already diverging again. This trick effectively increases the spot size of the laser beam, which can be regulated by changing the focal length of the focusing lens and also its position in front of the microscope objective. The best results were achieved for a focal length $f = 200\,\mathrm{mm}$, resulting in a spot size of $6\,\mu\mathrm{m}$ in the focal plane of the objective. The experimental setup is shown in Figure 5.25b. The experiments were conducted by illuminating the gold nanoparticles with a low laser power and increasing this until injection occurred. At low laser powers nothing happened. Increasing the laser power the gold nanoparticles began to diffuse on the membranes as described before. At even higher laser powers, the diffusing nanoparticles sometimes penetrated the membrane and began diffusing within the vesicle. The diffusion was much faster than for the nanoparticles on the vesicle membranes. To prove that the nanoparticles are actually inside the vesicles, we performed single particle tracking for the injected nanoparticles.

An exemplifying $40\,\mathrm{sec}$ track of a gold nanoparticle diffusing inside a phospholipid vesicle is shown in Figure 5.27c. The nanoparticle, which was observed for five minutes, was clearly inside the vesicle and did not escape. This behavior was seen for many gold nanoparticles on DPPC vesicles. To study the injection mechanism, we repeated the measurement with vesicles made out of DOPC ($T_m = -21\,^{\circ}\mathrm{C}$), DC$_{15}$PC ($T_m = 33\,^{\circ}\mathrm{C}$), and DC$_{17}$PC ($T_m = 48\,^{\circ}\mathrm{C}$). For DC$_{15}$PC and DC$_{17}$PC we observed the same as for the DPPC vesicles. For DOPC vesicles the situation is completely different. Only once were we able to inject a nanoparticle attached to a DOPC membrane into the vesicle. Another observation is that, upon illumination

with the laser, the entire DOPC vesicle moves around. This is in contrast to the vesicles with a main transition temperature above room temperature, which do not move at all. Taking the laser power at which each event occurred in order to calculate the temperatures present in the membrane, we obtain the following values: $T_{DC_{15}PC} = 54 \pm 9\,°\text{C}$, $T_{DPPC} = 60 \pm 11\,°\text{C}$, $T_{DC_{17}PC} = 61 \pm 14\,°\text{C}$. These all have a large standard deviation, but show a clear trend. More importantly however, we never observed an injection event at a temperature below the main transition temperature of the respective phospholipid. Consequently, it seems as if the main transition temperature plays an important role for the mechanism.
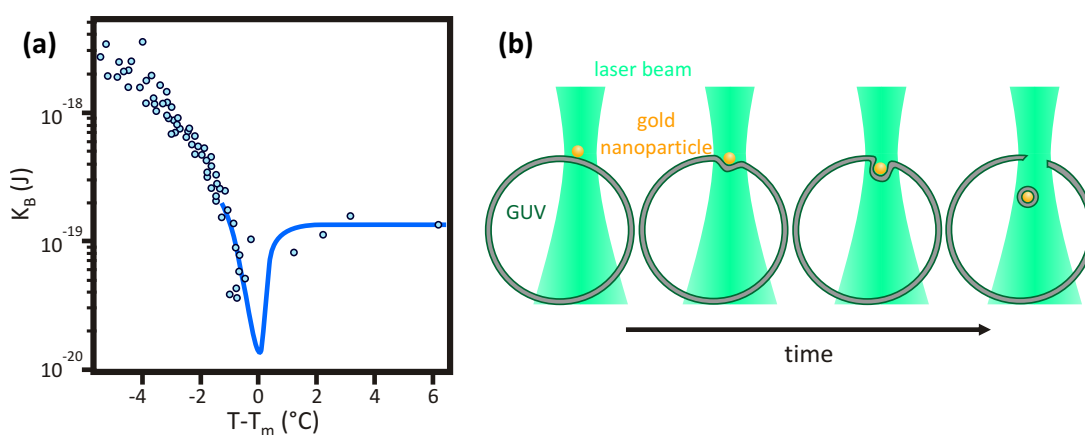
Figure 5.28 | Membrane elasticity enables injection. (a) The elastic bending modulus K_B of a phospholipid membrane is strongly temperature dependent, especially around the main transition temperature (from Heimburg 2007[89]). (b) A gold nanoparticle attached to a phospholipid vesicle is illuminated by a laser, heating up the surrounding membrane. Because of the stark contrast between the bending moduli of the fluid and gel phases, the gold nanoparticle, pushed by the optical forces of the laser, bends the membrane inwards until it breaks and wraps itself around the nanoparticle. This leaves a hole in the vesicle membrane and the gold nanoparticle diffuses through the vesicle.

At the main transition temperature several membrane properties change considerably. One of these parameters is the *elastic bending modulus*, K_B, which is a measure for the rigidity of the membrane. Between the gel and fluid phases K_B changes by more than an order of magnitude (Figure 5.28a), which is one of the reasons for the different shapes of gel phase and fluid phase vesicles. The bending modulus can be used to explain the injection of gold nanoparticles attached to the

membrane into the vesicles (Figure 5.28b). The gold nanoparticle, illuminated by the laser, heats up the membrane in its vicinity, inducing a phase change from the gel to the fluid phase. The laser exerts a strong axial force on the nanoparticles and because the fluid phase is much less stiff, the membrane bends inwards around the gold nanoparticle. At the same time the gel phase does not move, being very rigid. This leads to the membrane bending around the gold nanoparticle until it pinches off at the boundary between gel and fluid phases, completely surrounding the nanoparticle. The nanoparticle diffuses through the vesicle, leaving behind a hole in the vesicle membrane. Depending on the actual temperature of the gold nanoparticle, the fluid phase region has a diameter larger than $170\,\mathrm{nm}$. With a hole this size, the nanoparticle should be able to diffuse out of the nanoparticle after a certain time. This is actually seen experimentally, with the gold nanoparticles diffusing out of the vesicle at exactly the same position where they were previously attached to the membrane. This generally takes between $20\,\mathrm{sec}$ and $3\,\mathrm{min}$. We did not, however, check to see whether this is the case for every nanoparticle. Further studies are being carried out, investigating the dwelling time of the gold nanoparticles inside the vesicles and relating this to the hole size. A detailed study of the phenomena described in this chapter can be found elsewhere[188].

5.5 Discussion

In this chapter many experiments were presented analyzing interactions between gold nanoparticles and phospholipid membranes. Firstly, several methods were investigated, concerning attaching gold nanoparticles to the membranes. Commercially obtainable gold nanospheres are usually covered with citrate molecules and bound lightly via electrostatic interactions to pre-formed giant unilamellar vesicles. Much more stable was the binding of gold nanoparticles coated with a layer of CTAB. We developed a method with which the citrate molecules can be replaced with a cationic surfactant, CTAB, which arranges in a bilayer around the gold nanoparticle. Upon coming into contact with the vesicles, the CTAB probably formed an interdigitated bilayer with phospholipid molecules of the vesicle membrane. The binding both of the citrate- and the CTAB-coated gold nanoparticles was random and occurred upon combination of a vesicle solution and a gold nanoparticle

solution. Controlling the concentration of the gold nanoparticles was extremely important, as too high concentrations led to the destruction of the vesicles.

Two additional methods were presented, enabling a better control over the adhesion of gold nanoparticles to phospholipid vesicles. The first involved growing gold nanoparticles on vesicle membranes directly. The gold precursor $HAuCl_4^-$ was reduced by ascorbic acid in a solution containing DOPC vesicles. Gold nanoparticles grew predominantly on the phospholipid membranes. The size, shape and density could be controlled by adding small amounts of charged lipids to the DOPC solution when growing the GUVs and by varying the gold precursor concentration. Positively charged vesicles promoted the growth of many nanoparticles, which were smaller in size in comparison with neutral vesicles. Negatively charged vesicles on the other hand promoted the growth of only a few but much larger nanoparticles. At high concentrations of the precursor the gold nanoparticles became so dense on the vesicle surface that they began to couple plasmonically. The presented growth method is biocompatible, using no cytotoxic components and more rapid than many previously reported methods, being completed within $1 - 2\,\mathrm{h}$. This method may be interesting for drug-delivery applications.

The second method providing more control for attaching gold nanoparticles to phospholipid membranes was contrived during studies conducted in chapter 4. In this method the optical forces a laser exerts on metallic nanoparticles were utilized to print them onto phospholipid vesicles. This method is interesting because the nanoparticles could be positioned with a precision of only a few tens of nanometers. The only problem was the concentration of the gold in the external solution. Having it too low led to a long time necessary to induce a printing event. Too high concentrations destroyed the vesicles, because of a too large non-specific binding of the gold nanoparticles to the membrane. One possibility to overcome this problem would be the incorporation of a micro-injection system, with which one can inject a nanoparticle solution via a capillary direct into the vesicle solution, optimally directly into the laser beam. This would vastly improve the speed of the printing process and is being explored in further experiments.

Gold nanoparticles are well known as efficient optothermal energy converters. This capability was demonstrated by inducing reversible gel to fluid phase transitions of nanometric sized regions in phospholipid membranes with $80\,\text{nm}$ large gold nanoparticles. The size of the fluid region increased with the power density of the laser and typically lay in the range of $0-350\,\text{nm}$. The heating process itself was very rapid, with 95% of the temperature increase reached within $100\,\text{ns}$. Upon melting the membrane, the gold nanoparticles began to diffuse in the membrane due to the much higher lipid mobility in the fluid phase and melted new regions of the membrane as they diffused. The diffusion also increased with the power density of the laser and lay between $0.007\,\upmu\text{m}^2/\text{s}$ and $0.9\,\upmu\text{m}^2/\text{s}$. This corresponds well with values reported in both articial bilayers and in biological membranes[181,182]. The nanoparticles can be used as an investigative tool to determine characteristic properties of the membrane. This was shown by analyzing in detail the nanoparticle motion, which could be impeded by the progression the fluid phase front through the membrane as the nanoparticle diffused along the vesicle surface. The ability to control the phase transition enabled a guiding of the nanoparticles to precise positions on the vesicle membrane. This was accomplished by reducing the size of the laser spot, limiting the diffusion region of the gold nanoparticles and then driving the nanoparticles from behind with the optical forces of the laser beam. This positioning is essential for studying certain structures or proteins in real cells or model cells. It could be improved further by using longer wavelengths at which the radial forces are stronger and the guiding could be controlled more easily.

Results from experiments in both chapters were combined to enable the optical injection of gold nanoparticles into phospholipid vesicles. This had been done previously by combining one optical tweezer laser with a fs-pulsed laser, which photoporates the cell membrane. In our case we were able to achieve the same results, albeit on vesicles and not cells, using only one laser. The optical forces exerted on the gold nanoparticle by the laser induced the injection, which was facilitated by a fluid-gel phase transition in the membrane. The gold nanoparticles diffused inside the vesicles, which was confirmed by single-particle tracking. Sometimes the nanoparticles could be observed to leave the vesicle, with the nanoparticle always exiting at exactly the same position at which it entered the

vesicle. This suggests that the method was able to produce holes in the vesicle membrane. The size of the hole was determined by the fluid phase induced by the gold nanoparticle and was probably around $180\,\mathrm{nm}$ in size. This is much smaller than the holes created through photoporation, which are generally between $0.5\,\mu\mathrm{m}$ and $1\,\mu\mathrm{m}$[189] and might thus be less damaging to cells. Additional experiments are being carried to determine whether the gold nanoparticles can be used to increase drug-delivery efficiency into cells. The gold nanoparticles are used to either increase the permeability of the phospholipid membrane through controllable phase transitions or to destroy vesicles inside the cells, enabling drug molecules to enter the cytoplasm. These studies are still at the beginning stage, but are very promising, due to the capabilities of gold nanoparticles and the control one has over them.

6 Conclusions and Outlook

The main aim of this thesis was to use gold nanoparticles for the investigation and manipulation of molecular processes occurring in phospholipid membranes. We successfully established different methods for binding gold nanoparticles to phospholipid vesicles. Random binding was achieved by mixing commercially available gold nanoparticles, which we coated with a layer of CTAB, with a solution of pre-formed giant unilamellar vesicles. As an alternative method we developed a procedure for growing gold nanoparticles in the same solution directly on the membranes of such vesicles. We were able to somewhat control the size, shape and density of the nanoparticles by adding charged lipids to the vesicles and varying the concentration of the gold precursor. This method is useful not only for producing a platform to study gold nanoparticles on phospholipid vesicles but also for producing potential targeted drug-delivery vessels. A method providing more control over the adhesion of gold nanoparticles to the phospholipid vesicles was explored, using the optical forces acting on a gold nanoparticle in a laser beam to print them on to the vesicle membranes. In this manner the position and quantity of the gold nanoparticles could be controlled with great precision.

Gold nanoparticles attached to phospholipid vesicles were optically illuminated, thereby heating them and their surroundings. Several relevant observations were made: at high laser powers, the heating led to a rapid destruction of the vesicles. At lower laser powers, multiple simultaneously heated gold nanoparticles caused changes in shape of entire vesicles as they induced a phase transition in the membrane from the gel to the fluid phase. Single gold nanoparticles could also be heated on gel phase membranes; at sufficiently high laser powers they began to diffuse on the membrane. This was due to an induced phase transition; by measuring the motion of the nanoparticles, we were able to determine the speed with which

the fluid phase progressed through the gel phase membrane. Such controlled phase transitions not only enabled us to guide gold nanoparticles to specific positions on the membrane, but also to optically inject gold nanoparticles into the vesicles. The former is important when studying structures on biological membranes and the latter may provide a novel method for optical transfections of cells. Now that we have provided the proof of principle using spherical nanoparticles,the techniques presented here can be refined and developed further. For example, nanorods or nanoshells have plasmon resonances in the near-infrared window, a great advantage when using these devices in cellular systems. The guiding and positioning of the gold nanoparticles can be improved even further by using a laser emitting at longer wavelengths. Enhancing the spatial and temporal resolution of the acquisition system will enable a more detailed investigation of the phase transition in phospholipid membranes. This can be helpful when investigating phase phenomena, such as lipid rafts or protein partitioning in cell membranes.

Beginning as a side project originating from experiments on guiding nanoparticles over vesicle membranes, we established a new method for patterning substrates with single nanoparticles using solely a laser to create nanostructures. Here the laser serves multiple purposes: it collects the nanoparticles from the solution, guides them to the desired position on the substrate, and causes them to bind to the substrates through van der Waals interactions. The precision we achieved was even less than the size of the individual nanoparticles. In addition, the printed structures were very stable. The method could be extended to enable the printing of different nanoparticles present in the same solution, which no other method has achieved yet. Another application of this method is to create plasmonically coupling structures and align non-spherical nanoparticles. The efficiency of the method could be increased by using longer wavelengths which provide a stronger guiding of the nanoparticles. This should lead to higher precision and more rapid printing. Additionally, diffractive optics could be used to print multiple nanoparticles at different positions simultaneously.

References

1. Bhattacharya R, Mukherjee P. Biological properties of "naked" metal nanoparticles. *Advanced Drug Delivery Reviews* **2008**, 60 (11), 1289–1306. [cited on p. 1]
2. Ghosh SK, Nath S, Kundu S, Esumi K, Pal T. Solvent and ligand effects on the localized surface plasmon resonance (lspr) of gold colloids. *Journal of Physical Chemistry B* **2004**, 108 (37), 13963–13971. [cited on p. 1]
3. Hayat M: *Colloidal gold: principles, methods, and applications* Academic Press **1989**. [cited on p. 1]
4. Enustun BV, Turkevich J. Coagulation of colloidal gold. *Journal of the American Chemical Society* **1963**, 85 (21), 3317–3328. [cited on p. 1]
5. Frens G. Controlled nucleation for regulation of particle-size in monodisperse gold suspensions. *Nature-Physical Science* **1973**, 241 (105), 20–22. [cited on p. 1]
6. El-Sayed IH, Huang XH, El-Sayed MA. Selective laser photo-thermal therapy of epithelial carcinoma using anti-egfr antibody conjugated gold nanoparticles. *Cancer Letters* **2006**, 239 (1), 129–135. [cited on p. 1]
7. Hirsch LR, Gobin AM, Lowery AR, Tam F, Drezek RA, Halas NJ, West JL. Metal nanoshells. *Annals of Biomedical Engineering* **2006**, 34 (1), 15–22. [cited on p. 1]
8. Kumar PS, Pastoriza-Santos I, Rodriguez-Gonzalez B, Garcia de Abajo FJ, Liz-Marzan LM. High-yield synthesis and optical response of gold nanostars. *Nanotechnology* **2008**, 19 (1), –. [cited on p. 1]
9. Giljohann DA, Seferos DS, Daniel WL, Massich MD, Patel PC, Mirkin CA. Gold nanoparticles for biology and medicine. *Angewandte Chemie-International Edition* **2010**, 49 (19), 3280–3294. [cited on p. 1]
10. Catchpole KR, Polman A. Plasmonic solar cells. *Optics Express* **2008**, 16 (26), 21793–21800. [cited on p. 1]
11. Atwater HA, Polman A. Plasmonics for improved photovoltaic devices. *Nature Materials* **2010**, 9 (3), 205–213. [cited on p. 1]
12. Kusumi A, Ike H, Nakada C, Murase K, Fujiwara T. Single-molecule tracking of membrane molecules: plasma membrane compartmentalization and dynamic assembly of raft-philic signaling molecules. *Seminars in Immunology* **2005**, 17 (1), 3–21. [cited on p. 1]
13. Wang CC, Liang CP, Lee CH. Three-dimensional nanoparticle tracking and simultaneously membrane profiling during endocytosis of living cells. *Applied Physics Letters* **2009**, 95 (20), –. [cited on p. 1]
14. Raschke G, Kowarik S, Franzl T, Sönnichsen C, Klar T, Feldmann J, Nichtl A, Kürzinger K. Biomolecular recognition based on single gold nanoparticle light scattering. *Nano Letters* **2003**, 3 (7), 935–938. [cited on pp. 1,16]
15. El-Sayed I, Huang X, El-Sayed M. Surface plasmon resonance scattering and absorption of anti-egfr antibody conjugated gold nanoparticles in cancer diagnostics: applications in oral cancer. *Nano Lett* **2005**, 5 (5), 829–834. [cited on p. 1]

References

16. Kneipp K, Wang Y, Kneipp H, Perelman LT, Itzkan I, Dasari R, Feld MS. Single molecule detection using surface-enhanced raman scattering (sers). *Physical Review Letters* **1997**, 78 (9), 1667–1670. [cited on p. 2]

17. Bek A, Jansen R, Ringler M, Mayilo S, Klar TA, Feldmann J. Fluorescence enhancement in hot spots of afm-designed gold nanoparticle sandwiches. *Nano Letters* **2008**, 8 (2), 485–490. [cited on p. 2]

18. Ringler M, Schwemer A, Wunderlich M, Nichtl A, Kurzinger K, Klar TA, Feldmann J. Shaping emission spectra of fluorescent molecules with single plasmonic nanoresonators. *Physical Review Letters* **2008**, 100 (20), –. [cited on p. 2]

19. Dulkeith E, Niedereichholz T, Klar TA, Feldmann J, von Plessen G, Gittins DI, Mayya KS, Caruso F. Plasmon emission in photoexcited gold nanoparticles. *Physical Review B* **2004**, 70 (20), –. [cited on pp. 2, 15,18]

20. Govorov AO, Zhang W, Skeini T, Richardson H, Lee J, Kotov NA. Gold nanoparticle ensembles as heaters and actuators: melting and collective plasmon resonances. *Nanoscale Research Letters* **2006**, 1 (1), 84–90. [cited on p. 2]

21. Govorov AO, Richardson HH. Generating heat with metal nanoparticles. *Nano Today* **2007**, 2 (1), 30–38. [cited on pp. 2, 20,21]

22. Loo C, Lowery A, Halas NJ, West J, Drezek R. Immunotargeted nanoshells for integrated cancer imaging and therapy. *Nano Letters* **2005**, 5 (4), 709–711. [cited on p. 2]

23. Huang X, El-Sayed IH, Qian W, El-Sayed MA. Cancer cell imaging and photothermal therapy in the near-infrared region by using gold nanorods. *J. Am. Chem. Soc* **2006**, 128 (6), 2115–2120. [cited on p. 2]

24. Huang XH, Jain PK, El-Sayed IH, El-Sayed MA. Plasmonic photothermal therapy (pptt) using gold nanoparticles. *Lasers in Medical Science* **2008**, 23 (3), 217–228. [cited on p. 2]

25. Stehr J, Hrelescu C, Sperling RA, Raschke G, Wunderlich M, Nichtl A, Heindl D, Kurzinger K, Parak WJ, Klar TA, Feldmann J. Gold nanostoves for microsecond dna melting analysis. *Nano Letters* **2008**, 8 (2), 619–623. [cited on pp. 2,81]

26. Huang HC, Barua S, Kay DB, Rege K. Simultaneous enhancement of photothermal stability and gene delivery efficacy of gold nanorods using polyelectrolytes. *Acs Nano* **2009**, 3 (10), 2941–2952. [cited on p. 2]

27. Ba HJ, Rodriguez-Fernandez J, Stefani FD, Feldmann J. Immobilization of gold nanoparticles on living cell membranes upon controlled lipid binding. *Nano Letters* **2010**, 10 (8), 3006–3012. [cited on p. 2]

28. Zhu T, Vasilev K, Kreiter M, Mittler S, Knoll W. Surface modification of citrate-reduced colloidal gold nanoparticles with 2-mercaptosuccinic acid. *Langmuir* **2003**, 19 (22), 9518–9525. [cited on p. 2]

29. Kraus T, Malaquin L, Schmid H, Riess W, Spencer ND, Wolf H. Nanoparticle printing with single-particle resolution. *Nature Nanotechnology* **2007**, 2 (9), 570–576. [cited on pp. 2, 53,77]

30. Fujiwara T, Ritchie K, Murakoshi H, Jacobson K, Kusumi A. Phospholipids undergo hop diffusion in compartmentalized cell membrane. *Journal of Cell Biology* **2002**, 157 (6), 1071–1081. [cited on p. 2]

31. Bagatolli LA, Gratton E. Two-photon fluorescence microscopy observation of shape changes at the phase transition in phospholipid giant unilamellar vesicles. *Biophysical Journal* **1999**, 77 (4), 2090–2101. [cited on pp. 2,46]

32. Menger FM, Keiper JS. Chemistry and physics of giant vesicles as biomembrane models. *Current Opinion in Chemical Biology* **1998**, 2 (6), 726–732. [cited on pp. 2,5]

33. Bagatolli LA, Parasassi T, Gratton E. Giant phospholipid vesicles: comparison among the whole lipid sample characteristics using different preparation methods a two photon fluorescence microscopy study. *Chemistry and Physics of Lipids* **2000**, 105 (2), 135–147.

[cited on pp. 3, 37, 45,47]

34. Smith G, Gunthorpe M, Kelsell R, Hayes P, Reilly P, Facer P, Wright J, Jerman J, Walhin J, Ooi L. Trpv3 is a temperature-sensitive vanilloid receptor-like protein. *Nature* **2002**, 418 (6894), 186–190. [cited on p. 3]

35. Baumgart T, Hammond AT, Sengupta P, Hess ST, Holowka DA, Baird BA, Webb WW. Large-scale fluid/fluid phase separation of proteins and lipids in giant plasma membrane vesicles. *Proceedings of the National Academy of Sciences of the United States of America* **2007**, 104 (9), 3165–3170. [cited on p. 3]

36. Lasic DD, Papahadjopoulos D. Liposomes revisited. *Science* **1995**, 267 (5202), 1275–1276. [cited on p. 5]

37. Leonhardt U. Optical metamaterials - invisibility cup. *Nature Photonics* **2007**, 1 (4), 207–208. [cited on p. 6]

38. Börnstein L: *Numerical data and functional relationships in science and technology, group iii: crystal and solid state physics* John Wiley & Sons **1982**. [cited on p. 7]

39. Beversluis MR, Bouhelier A, Novotny L. Continuum generation from single gold nanostructures through near-field mediated intraband transitions. *Physical Review B* **2003**, 68 (11), –. [cited on pp. 7,9]

40. Kreibig U, Vollmer M: *Optical properties of metal clusters* Springer **1995**. [cited on pp. 7, 9, 13,16]

41. Ashcroft N, Mermin N: *Solid State Physics* Brooks/Cole **1976**. [cited on p. 7]

42. Hache F, Ricard D, Flytzanis C, Kreibig U. The optical kerr effect in small metal particles and metal colloids - the case of gold. *Applied Physics a-Materials Science & Processing* **1988**, 47 (4), 347–357. [cited on p. 9]

43. Kreibig U, VonfragsC. Limitation of electron mean free path in small silver particles. *Zeitschrift Fur Physik* **1969**, 224 (4), 307. [cited on p. 9]

44. Link S, El-Sayed MA. Size and temperature dependence of the plasmon absorption of colloidal gold nanoparticles. *Journal of Physical Chemistry B* **1999**, 103 (21), 4212–4217. [cited on p. 9]

45. Kopitzki K, Herzog P: *Einführung in die Festkörperphysik* Springer **2007**. [cited on p. 10]

46. Bassani G, Parravicini G: *Electronic states and optical transitions in solids* Pergamon, London **1975**. [cited on p. 10]

47. Johnson PB, Christy RW. Optical-constants of noble-metals. *Physical Review B* **1972**, 6 (12), 4370–4379. [cited on p. 10]

48. Quinten M: *MQMie 2.4* Aldenhoven **2004**. [cited on p. 11]

49. Bohren C, Huffman D: *Absorption and scattering of light by small particles* New York: John Wiley & Sons **1983**. [cited on p. 12]

50. Hovel H, Fritz S, Hilger A, Kreibig U, Vollmer M. Width of cluster plasmon resonances - bulk dielectric functions and chemical interface damping. *Physical Review B* **1993**, 48 (24), 18178–18188. [cited on p. 13]

51. Jackson J: *Classical Electrodynamics* Berlin-New York: Walter de Gruyter **1983**. [cited on p. 15]

52. Klar T, Perner M, Grosse S, von Plessen G, Spirkl W, Feldmann J. Surface-plasmon resonances in single metallic nanoparticles. *Physical Review Letters* **1998**, 80 (19), 4249–4252. [cited on pp. 15,19]

53. Sonnichsen C, Geier S, Hecker NE, von Plessen G, Feldmann J, Ditlbacher H, Lamprecht B, Krenn JR, Aussenegg FR, Chan VZH, Spatz JP, Moller M. Spectroscopy of single metallic nanoparticles using total internal reflection microscopy. *Applied Physics Letters* **2000**, 77 (19), 2949–2951. [cited on p. 15]

54. Sonnichsen C, Franzl T, Wilk T, von Plessen G, Feldmann J. Plasmon resonances in large noble-metal clusters. *New Journal of Physics* **2002**, 4, –. [cited on p. 16]

55. Raschke G, Brogl S, Susha AS, Rogach AL, Klar TA, Feldmann J, Fieres B, Petkov N, Bein T, Nichtl A. Gold nanoshells improve single nanoparticle molecular sensors. *Nano Letters* **2004**, 4 (10),

References

1853–1857. [cited on p. 16]

56. Harris N, Ford MJ, Cortie MB. Optimization of plasmonic heating by gold nanospheres and nanoshells. *Journal of Physical Chemistry B* **2006**, 110, 10701–10707. [cited on p. 18]

57. Schoenlein RW, Lin WZ, Fujimoto JG, Eesley GL. Femtosecond studies of nonequilibrium electronic processes in metals. *Physical Review Letters* **1987**, 58 (16), 1680–1683. [cited on pp. 18,20]

58. Elsayedali HE, Juhasz T, Smith GO, Bron WE. Femtosecond thermoreflectivity and thermotransmissivity of polycrystalline and single-crystalline gold-films. *Physical Review B* **1991**, 43 (5), 4488–4491. [cited on pp. 18,20]

59. Perner M, Bost P, Lemmer U, von Plessen G, Feldmann J, Becker U, Mennig M, Schmitt M, Schmidt H. Optically induced damping of the surface plasmon resonance in gold colloids. *Physical Review Letters* **1997**, 78 (11), 2192. [cited on p. 18]

60. Perner M, Gresillon S, Marz J, von Plessen G, Feldmann J, Porstendorfer J, Berg KJ, Berg G. Observation of hot-electron pressure in the vibration dynamics of metal nanoparticles. *Physical Review Letters* **2000**, 85 (4), 792–795. [cited on pp. 18,81]

61. Hodak J, Martini I, Hartland GV. Ultrafast study of electron-phonon coupling in colloidal gold particles. *Chemical Physics Letters* **1998**, 284 (1-2), 135–141. [cited on pp. 18,20]

62. Puech K, Henari FZ, Blau WJ, Duff D, Schmid G. Investigation of the ultrafast dephasing time of gold nanoparticles using incoherent-light. *Chemical Physics Letters* **1995**, 247 (1-2), 13–17. [cited on p. 18]

63. Fann WS, Storz R, Tom HWK, Bokor J. Electron thermalization in gold. *Physical Review B* **1992**, 46 (20), 13592–13595. [cited on p. 19]

64. Sun CK, Vallee F, Acioli LH, Ippen EP, Fujimoto JG. Femtosecond-tunable measurement of electron thermalization in gold. *Physical Review B* **1994**, 50 (20), 15337–15348. [cited on p. 19]

65. Suarez C, Bron WE, Juhasz T. Dynamics and transport of electronic carriers in thin gold-films. *Physical Review Letters* **1995**, 75 (24), 4536–4539. [cited on p. 20]

66. Hu M, Hartland GV. Heat dissipation for au particles in aqueous solution: Relaxation time versus size. *Journal of Physical Chemistry B* **2002**, 106 (28), 7029–7033. [cited on p. 20]

67. Urban AS, Fedoruk M, Horton MR, Radler J, Stefani FD, Feldmann J. Controlled nanometric phase transitions of phospholipid membranes by plasmonic heating of single gold nanoparticles. *Nano Letters* **2009**, 9 (8), 2903–2908. [cited on p. 20]

68. Pitsillides CM, Joe EK, Wei X, Anderson RR, Lin CP. Selective cell targeting with light-absorbing microparticles and nanoparticles. *Biophysical Journal* **2003**, 84 (6), 4023–4032. [cited on p. 21]

69. Bohren C, Moretti M, Levitt M, Kales D: *Selected papers on scattering in the atmosphere* Society of Photo Optical **1989**. [cited on p. 24]

70. Nishita T, Dobashi Y, Nakamae E. Display of clouds taking into account multiple anisotropic scattering and sky light. **1996**, page 386. [cited on p. 24]

71. Ashkin A. Acceleration and trapping of particles by radiation pressure. *Physical Review Letters* **1970**, 24 (4), 156. [cited on p. 24]

72. Ashkin A, Dziedzic JM, Bjorkholm JE, Chu S. Observation of a single-beam gradient force optical trap for dielectric particles. *Optics Letters* **1986**, 11 (5), 288–290. [cited on p. 24]

73. Chu S. Laser trapping of neutral particles. *Scientific American* **1992**, 266 (2), 70–76. [cited on p. 24]

74. Ashkin A, Dziedzic JM. Optical trapping and manipulation of viruses and bacteria. *Science* **1987**, 235 (4795), 1517–1520. [cited on p. 24]

75. Svoboda K, Schmidt CF, Schnapp BJ, Block SM. Direct observation of kinesin stepping by optical trapping interferometry. *Nature* **1993**, 365 (6448), 721–727. [cited on p. 24]

76. Gordon JP. Radiation forces and momenta in dielectric media. *Physical Review A* **1973**, 8 (1), 14–21. [cited on p. 25]

77. Ise N, Sogami I: *Structure formation in solution: ionic polymers and colloidal particles* Springer **2005**. [cited on p. 26]

78. Derjaguin B, Landau L. A theory of the stability of strongly charged lyophobic sols and the coalescence of strongly charged particles in electrolytic solution. *Acta Phys.-Chim. USSR* **1941**, 14, 633–662. [cited on p. 26]

79. Verwey E, Overbeek J: *Theory of the stability of lyotropic colloids* Elsevier, Amsterdam **1948**. [cited on p. 26]

80. Zeta Potential of Colloids in Water and Waste Water. *ASTM Standard D 4187-82, American Society for Testing and Materials* **1985**, . [cited on p. 27]

81. Freitas C, Muller RH. Effect of light and temperature on zeta potential and physical stability in solid lipid nanoparticle (sln (tm)) dispersions. *International Journal of Pharmaceutics* **1998**, 168 (2), 221–229. [cited on p. 27]

82. Hamaker HC. The london - van der waals attraction between spherical particles. *Physica* **1937**, 4, 1058–1072. [cited on p. 28]

83. Israelachvili J, Tabor D. Van der Waals forces: theory and experiment. *Progress in Surface and Membrane Science* **1973**, 7, 1–55. [cited on p. 28]

84. Israelachvili J: *Intermolecular and Surface Forces.* Academic, London **1992**. [cited on pp. 28, 30,71]

85. Mahanty J, Ninham B: *Dispersion forces forces* Academic Press Inc. **1977**. [cited on p. 29]

86. Israelachvili JN. Calculation of vanderwaals dispersion forces between macroscopic bodies. *Proceedings of the Royal Society of London Series a-Mathematical and Physical Sciences* **1972**, 331 (1584), 39–55. [cited on p. 29]

87. Tyurina YY, Shvedova AA, Kawai K, Tyurin VA, Kommineni C, Quinn PJ, Schor NF, Fabisiak JP, Kagan VE. Phospholipid signaling in apoptosis: peroxidation and externalization of phosphatidylserine. *Toxicology* **2000**, 148 (2-3), 93–101. [cited on p. 32]

88. Israelachvili JN, Marcelja S, Horn RG. Physical principles of membrane organization. *Quarterly Reviews of Biophysics* **1980**, 13 (2), 121–200. [cited on p. 32]

89. Heimburg T: *Thermal biophysics of membranes* Vch Verlagsgesellschaft Mbh **2007**. [cited on pp. 34, 36,117]

90. Cevc G: *Phospholipids handbook* Marcel Dekker Inc **1993**. [cited on pp. 34,36]

91. Heimburg T. A model for the lipid pretransition: Coupling of ripple formation with the chain-melting transition. *Biophysical Journal* **2000**, 78 (3), 1154–1165. [cited on p. 35]

92. Janiak MJ, Small DM, Shipley GG. Temperature and compositional dependence of the structure of hydrated dimyristoyl lecithin. *Journal of Biological Chemistry* **1979**, 254 (13), 6068–6078. [cited on p. 35]

93. Lipowsky R, Sackmann E: *Structure and dynamics of membranes* Elsevier **1995**. [cited on p. 35]

94. Xie AF, Yamada R, Gewirth AA, Granick S. Materials science of the gel to fluid phase transition in a supported phospholipid bilayer. *Physical Review Letters* **2002**, 89 (24), –. [cited on p. 35]

95. Dietrich C, Volovyk ZN, Levi M, Thompson NL, Jacobson K. Partitioning of thy-1, gm1, and cross-linked phospholipid analogs into lipid rafts reconstituted in supported model membrane monolayers. *Proceedings of the National Academy of Sciences of the United States of America* **2001**, 98 (19), 10642–10647. [cited on p. 36]

96. Homan R, Pownall HJ. Transbilayer diffusion of phospholipids - dependence on headgroup structure and acyl chain-length. *Biochimica et Biophysica Acta* **1988**, 938 (2), 155–166. [cited on p. 36]

97. Alberts B, Johnson A, Lewis J, Raff M, Roberts K, Walter P: *Molecular Biology of the Cell, Fourth Edition* Garland **2002**. [cited on p. 36]

98. McNeil PL. Repairing a torn cell surface: make way, lysosomes to the rescue. *Journal of Cell Science* **2002**, 115 (5), 873–879. [cited on p. 36]

References

99. Riske KA, Amaral LQ, Lamy MT. Extensive bilayer perforation coupled with the phase transition region of an anionic phospholipid. *Langmuir* **2009**, 25 (17), 10083–10091. [cited on p. 36]

100. Kwik J, Boyle S, Fooksman D, Margolis L, Sheetz MP, Edidin M. Membrane cholesterol, lateral mobility, and the phosphatidylinositol 4,5-bisphosphate-dependent organization of cell actin. *Proceedings of the National Academy of Sciences of the United States of America* **2003**, 100 (24), 13964–13969. [cited on p. 36]

101. Lodish H, Berk A: *Molecular cell biology* WH Freeman **2008**. [cited on p. 37]

102. Bangham AD. Surrogate cells or trojan horses - the discovery of liposomes. *Bioessays* **1995**, 17 (12), 1081–1088. [cited on p. 37]

103. Olbrich K, Rawicz W, Needham D, Evans E. Water permeability and mechanical strength of polyunsaturated lipid bilayers. *Biophysical Journal* **2000**, 79 (1), 321–327. [cited on p. 37]

104. Singer M. Permeability of phosphatidylcholine and phosphatidylethanolamine bilayers. *Chemistry and Physics of Lipids* **1981**, 28 (3), 253–267. [cited on p. 37]

105. Xiang TX, Anderson BD. Phase structures of binary lipid bilayers as revealed by permeability of small molecules. *Biochimica Et Biophysica Acta-Biomembranes* **1998**, 1370 (1), 64–76. [cited on p. 37]

106. Disalvo EA, Campos AM, Abuin E, Chaimovich H, Lissi EA. Kinetics of surface changes of large unilamellar vesicles induced by osmotic shrinkage. *Biophysical Journal* **1994**, 66 (2), A349–A349. [cited on p. 37]

107. Lentz BR, Carpenter TJ, Alford DR. Spontaneous fusion of phosphatidylcholine small unilamellar vesicles in the fluid phase. *Biochemistry* **1987**, 26 (17), 5389–5397. [cited on p. 37]

108. Baumgart T, Das S, Webb WW, Jenkins JT. Membrane elasticity in giant vesicles with fluid phase coexistence. *Biophysical Journal* **2005**, 89 (2), 1067–1080. [cited on p. 38]

109. Lyklema J. Electrokinetics after smoluchowski. *Colloids and Surfaces a-Physicochemical and Engineering Aspects* **2003**, 222 (1-3), 5–14. [cited on p. 43]

110. Reeves JP, Dowben RM. Formation and properties of thin-walled phospholipid vesicles. *Journal of Cellular Physiology* **1969**, 73 (1), 49–60. [cited on p. 45]

111. Moscho A, Orwar O, Chiu DT, Modi BP, Zare RN. Rapid preparation of giant unilamellar vesicles. *Proceedings of the National Academy of Sciences of the United States of America* **1996**, 93 (21), 11443–11447. [cited on p. 45]

112. Angelova MI, Dimitrov DS. Liposome electroformation. *Faraday Discussions of the Chemical Society* **1986**, 81, 303–311. [cited on p. 45]

113. Angelova M, Soléau S, Méléard P, Faucon F, Bothorel P. Preparation of giant vesicles by external ac electric fields. kinetics and applications. *Trends in Colloid and Interface Science VI* **1992**, pages 127–131. [cited on p. 45]

114. Pott T, Bouvrais H, Meleard P. Giant unilamellar vesicle formation under physiologically relevant conditions. *Chemistry and Physics of Lipids* **2008**, 154 (2), 115–119. [cited on pp. 47,48]

115. Lee Z, Jeon KJ, Dato A, Erni R, Richardson TJ, Frenklach M, Radmilovic V. Direct imaging of soft-hard interfaces enabled by graphene. *Nano Letters* **2009**, 9 (9), 3365–3369. [cited on p. 49]

116. Turkevich J, Stevenson PC, Hillier J. A study of the nucleation and growth processes in the synthesis of colloidal gold. *Discussions of the Faraday Society* **1951**, 11, 55–75. [cited on pp. 49,85]

117. Murphy CJ, Jana NR. Controlling the aspect ratio of inorganic nanorods and nanowires. *Advanced Materials* **2002**, 14 (1), 80–82. [cited on p. 49]

118. Gao JX, Bender CM, Murphy CJ. Dependence of the gold nanorod aspect ratio on the nature of the directing surfactant in aqueous solution. *Langmuir* **2003**, 19 (21), 9065–9070. [cited on p. 49]

119. Pashley RM, Mcguiggan PM, Horn RG, Ninham BW. Forces between bilayers of cetyltrimethy-lammonium bromide in micellar solutions. *Journal of Colloid and Interface Science* **1988**, 126 (2), 569–578. [cited on p. 50]

120. Sambrook J, Fritsch E, Maniatis T, et al.: *Molecular cloning* Cold Spring Harbor Laboratory Press Cold Spring Harbor, NY **1989**. [cited on p. 50]

121. Caruso F, Lichtenfeld H, Donath E, Mohwald H. Investigation of electrostatic interactions in polyelectrolyte multilayer films: Binding of anionic fluorescent probes to layers assembled onto colloids. *Macromolecules* **1999**, 32 (7), 2317–2328. [cited on p. 51]

122. Hung AM, Micheel CM, Bozano LD, Osterbur LW, Wallraff GM, Cha JN. Large-area spatially ordered arrays of gold nanoparticles directed by lithographically confined dna origami. *Nature Nanotechnology* **2010**, 5 (2), 121–126. [cited on p. 53]

123. Su GX, Yan B. Nano-combinatorial chemistry strategy for nanotechnology research. *Journal of Combinatorial Chemistry* **2010**, 12 (2), 215–221. [cited on p. 53]

124. Chan EM, Xu CX, Mao AW, Han G, Owen JS, Cohen BE, Milliron DJ. Reproducible, high-throughput synthesis of colloidal nanocrystals for optimization in multidimensional parameter space. *Nano Letters* **2010**, 10 (5), 1874–1885. [cited on p. 53]

125. Saavedra HM, Mullen TJ, Zhang PP, Dewey DC, Claridge SA, Weiss PS. Hybrid strategies in nanolithography. *Reports on Progress in Physics* **2010**, 73 (3), –. [cited on p. 53]

126. Il Lee T, Choi WJ, Moon KJ, Choi JH, Kar JP, Das SN, Kim YS, Baik HK, Myoung JM. Programmable direct-printing nanowire electronic components. *Nano Letters* **2010**, 10 (3), 1016–1021. [cited on p. 53]

127. Hoogenboom JP, Vossen DLJ, Faivre-Moskalenko C, Dogterom M, van Blaaderen A. Patterning surfaces with colloidal particles using optical tweezers. *Applied Physics Letters* **2002**, 80 (25), 4828–4830. [cited on pp. 53, 76,77]

128. Shin C, Jeon I, Jeon S, Khim ZG. Single nanoparticle alignment by atomic force microscopy indentation. *Applied Physics Letters* **2009**, 94 (16), –. [cited on p. 53]

129. Ashkin A. Optical trapping and manipulation of neutral particles using lasers. *Proceedings of the National Academy of Sciences of the United States of America* **1997**, 94 (10), 4853–4860. [cited on p. 54]

130. Svoboda K, Block SM. Optical trapping of metallic rayleigh particles. *Optics Letters* **1994**, 19 (13), 930–932. [cited on p. 54]

131. Hansen PM, Bhatia VK, Harrit N, Oddershede L. Expanding the optical trapping range of gold nanoparticles. *Nano Letters* **2005**, 5 (10), 1937–1942. [cited on p. 54]

132. Arias-Gonzalez JR, Nieto-Vesperinas M. Optical forces on small particles: attractive and repulsive nature and plasmon-resonance conditions. *Journal of the Optical Society of America a-Optics Image Science and Vision* **2003**, 20 (7), 1201–1209. [cited on p. 54]

133. Toussaint KC, Liu M, Pelton M, Pesic J, Guffey MJ, Guyot-Sionnest P, Scherer NF. Plasmon resonance-based optical trapping of single and multiple au nanoparticles. *Optics Express* **2007**, 15 (19), 12017–12029. [cited on p. 54]

134. Dienerowitz M, Mazilu M, Reece PJ, Krauss TF, Dholakia K. Optical vortex trap for resonant confinement of metal nanoparticles. *Optics Express* **2008**, 16 (7), 4991–4999. [cited on p. 54]

135. Bos R, van der Mei HC, Busscher HJ. Physico-chemistry of initial microbial adhesive interactions - its mechanisms and methods for study. *Fems Microbiology Reviews* **1999**, 23 (2), 179–230. [cited on p. 56]

136. Walldal C. Flocculation studied with the esa technique. *Journal of Colloid and Interface Science* **1999**, 217 (1), 49–59. [cited on p. 56]

137. Biggs S, Mulvaney P. Measurement of the forces between gold surfaces in water by atomic-force microscopy. *Journal of Chemical Physics* **1994**, 100 (11), 8501–8505. [cited on p. 56]

138. Ahmadi G: Particle transport, deposition and removal ii online curriculum **2005**. [cited on p. 56]

139. Barton JP, Alexander DR. 5th-order corrected electromagnetic-field components for a fundamental gaussian-beam. *Journal of Applied Physics* **1989**, 66 (7), 2800–2802. [cited on p. 58]

References

140. Agayan RR, Gittes F, Kopelman R, Schmidt CF. Optical trapping near resonance absorption. *Applied Optics* **2002**, 41 (12), 2318–2327. [cited on pp. 59,111]

141. Ringler M: *Plasmonische Nahfeldresonatoren aus zwei biokonjugierten Goldnanopartikeln*. Ph.D. thesis: Ludwig-Maximilians-Universität München. **2008**. [cited on p. 70]

142. Tong L, Miljkovic´ VD, Kä¨ll M. Alignment, rotation, and spinning of single plasmonic nanoparticles and nanowires using polarization dependent optical forces. *Nano Letters* **2009**, . [cited on pp. 74,75]

143. Jiang L, Wang W, Fuchs H, Chi L. One-dimensional arrangement of gold nanoparticles with tunable interparticle distance. *Small* **2009**, 5 (24), 2819–2822. [cited on p. 77]

144. Maier SA, Brongersma ML, Kik PG, Meltzer S, Requicha AAG, Atwater HA. Plasmonics - a route to nanoscale optical devices. *Advanced Materials* **2001**, 13 (19), 1501–. [cited on p. 79]

145. Huang B, Wang WQ, Bates M, Zhuang XW. Three-dimensional super-resolution imaging by stochastic optical reconstruction microscopy. *Science* **2008**, 319 (5864), 810–813. [cited on p. 81]

146. Nagerl UV, Willig KI, Hein B, Hell SW, Bonhoeffer T. Live-cell imaging of dendritic spines by sted microscopy. *Proceedings of the National Academy of Sciences of the United States of America* **2008**, 105 (48), 18982–18987. [cited on p. 81]

147. Yildiz A, Forkey JN, McKinney SA, Ha T, Goldman YE, Selvin PR. Myosin v walks hand-over-hand: Single fluorophore imaging with 1.5-nm localization. *Science* **2003**, 300 (5628), 2061–2065. [cited on p. 81]

148. Lidke DS, Nagy P, Heintzmann R, Arndt-Jovin DJ, Post JN, Grecco HE, Jares-Erijman EA, Jovin TM. Quantum dot ligands provide new insights into erbb/her receptor-mediated signal transduction. *Nature Biotechnology* **2004**, 22 (2), 198–203. [cited on p. 81]

149. Richardson HH, Carlson MT, Tandler PJ, Hernandez P, Govorov AO. Experimental and theoretical studies of light-to-heat conversion and collective heating effects in metal nanoparticle solutions. *Nano Letters* **2009**, 9 (3), 1139–1146. [cited on p. 81]

150. Cognet L, Tardin C, Boyer D, Choquet D, Tamarat P, Lounis B. Single metallic nanoparticle imaging for protein detection in cells. *Proceedings of the National Academy of Sciences of the United States of America* **2003**, 100 (20), 11350–11355. [cited on p. 81]

151. Sershen SR, Westcott SL, Halas NJ, West JL. Temperature-sensitive polymer-nanoshell composites for photothermally modulated drug delivery. *Journal of Biomedical Materials Research* **2000**, 51 (3), 293–298. [cited on p. 81]

152. Skirtach AG, Dejugnat C, Braun D, Susha AS, Rogach AL, Parak WJ, Mohwald H, Sukhorukov GB. The role of metal nanoparticles in remote release of encapsulated materials. *Nano Letters* **2005**, 5 (7), 1371–1377. [cited on pp. 81,93]

153. Hirsch LR, Stafford RJ, Bankson JA, Sershen SR, Rivera B, Price RE, Hazle JD, Halas NJ, West JL. Nanoshell-mediated near-infrared thermal therapy of tumors under magnetic resonance guidance. *Proceedings of the National Academy of Sciences of the United States of America* **2003**, 100 (23), 13549–13554. [cited on p. 81]

154. Egawa H, Furusawa K. Liposome adhesion on mica surface studied by atomic force microscopy. *Langmuir* **1999**, 15 (5), 1660–1666. [cited on p. 84]

155. Pincet F, Cribier S, Perez E. Bilayers of neutral lipids bear a small but significant charge. *European Physical Journal B* **1999**, 11 (1), 127–130. [cited on p. 84]

156. Dietrich C, Angelova M, Pouligny B. Adhesion of latex spheres to giant phospholipid vesicles: Statics and dynamics. *Journal De Physique Ii* **1997**, 7 (11), 1651–1682. [cited on p. 84]

157. Deserno M, Bickel T. Wrapping of a spherical colloid by a fluid membrane. *Europhysics Letters* **2003**, 62 (5), 767–773. [cited on p. 84]

158. Fery A, Moya S, Puech PH, Brochard-Wyart F, Mohwald H. Interaction of polyelectrolyte coated beads with phospholipid vesicles. *Comptes Rendus Physique* **2003**, 4 (2), 259–264. [cited on p. 84]

159. Hong K, Friend DS, Glabe CG, Papahadjopoulos D. Liposomes containing colloidal gold are a useful probe of liposome-cell interactions. *Biochimica et Biophysica Acta* **1983**, 732 (1), 320–323. [cited on p. 85]

160. Chiu DT, Wilson CF, Ryttsen F, Stromberg A, Farre C, Karlsson A, Nordholm S, Gaggar A, Modi BP, Moscho A, Garza-Lopez RA, Orwar O, Zare RN. Chemical transformations in individual ultrasmall biomimetic containers. *Science* **1999**, 283 (5409), 1892–1895. [cited on p. 85]

161. Paasonen L, Laaksonen T, Johans C, Yliperttula M, Kontturi K, Urtti A. Gold nanoparticles enable selective light-induced contents release from liposomes. *Journal of Controlled Release* **2007**, 122 (1), 86–93. [cited on p. 85]

162. Wu G, Mikhailovsky A, Khant HA, Fu C, Chiu W, Zasadzinski JA. Remotely triggered liposome release by near-infrared light absorption via hollow gold nanoshells. *Journal of the American Chemical Society* **2008**, 130 (26), 8175–8177. [cited on p. 85]

163. Faure C, Derre A, Neri W. Spontaneous formation of silver nanoparticles in multilamellar vesicles. *Journal of Physical Chemistry B* **2003**, 107 (20), 4738–4746. [cited on p. 85]

164. He P, Urban MW. Phospholipid-stabilized au-nanoparticles. *Biomacromolecules* **2005**, 6 (3), 1224–1225. [cited on p. 85]

165. Robertson D, Tiersch B, Kosmella S, Koetz J. Preparation of crystalline gold nanoparticles at the surface of mixed phosphatidylcholine-ionic surfactant vesicles. *Journal of Colloid and Interface Science* **2007**, 305 (2), 345–351. [cited on p. 85]

166. Jana NR, Gearheart L, Murphy CJ. Seed-mediated growth approach for shape-controlled synthesis of spheroidal and rod-like gold nanoparticles using a surfactant template. *Advanced Materials* **2001**, 13 (18), 1389–1393. [cited on p. 85]

167. Galla HJ, Sackmann E. Chemically-induced lipid phase separation in model membranes containing charged lipids - spin label study. *Biochimica et Biophysica Acta* **1975**, 401 (3), 509–529. [cited on p. 87]

168. Shoemaker SD, Vanderlick TK. Intramembrane electrostatic interactions destabilize lipid vesicles. *Biophysical Journal* **2002**, 83 (4), 2007–2014. [cited on p. 87]

169. Andreescu D, Sau TK, Goia DV. Stabilizer-free nanosized gold sols. *Journal of Colloid and Interface Science* **2006**, 298 (2), 742–751. [cited on p. 90]

170. Koltover I, Rädler JO, Safinya CR. Membrane mediated attraction and ordered aggregation of colloidal particles bound to giant phospholipid vesicles. *Physical Review Letters* **1999**, 82 (9), 1991–1994. [cited on p. 93]

171. Uechi I, Yamada S. Photochemical and analytical applications of gold nanoparticles and nanorods utilizing surface plasmon resonance. *Analytical and Bioanalytical Chemistry* **2008**, 391 (7), 2411–2421. [cited on p. 93]

172. Biesso A, Qian W, Huang XH, El-Sayed MA. Gold nanoparticles surface plasmon field effects on the proton pump process of the bacteriorhodopsin photosynthesis. *Journal of the American Chemical Society* **2009**, 131 (7), 2442–2443. [cited on p. 93]

173. Nollert P, Kiefer H, Jahnig F. Lipid vesicle adsorption versus formation of planar bilayers on solid-surfaces. *Biophysical Journal* **1995**, 69 (4), 1447–1455. [cited on p. 94]

174. Schonherr H, Johnson JM, Lenz P, Frank CW, Boxer SG. Vesicle adsorption and lipid bilayer formation on glass studied by atomic force microscopy. *Langmuir* **2004**, 20 (26), 11600–11606. [cited on p. 94]

175. Neumann J, Brinkmann R. Nucleation dynamics around single microabsorbers in water heated by nanosecond laser irradiation. *Journal of Applied Physics* **2007**, 101 (11), –. [cited on p. 96]

176. Blume A. Apparent molar heat-capacities of phospholipids in aqueous dispersion - effects of chain-length and head group-structure. *Biochemistry* **1983**, 22 (23), 5436–5442. [cited on p. 98]

177. Feller SE, Venable RM, Pastor RW. Computer simulation of a dppc phospholipid bilayer: Structural changes as a function of molecular surface area. *Langmuir* **1997**, 13 (24), 6555–6561.

[cited on p. 98]

178. Skripov V, Sinitsyn E, Pavlov P, Ermakov G, Muratov G, Bulanov N, Baidakov V: *Thermophysical properties of liquids in the metastable (superheated) state* New York, NY (US); Gordon and Breach Science Publishers **1988**. [cited on p. 98]

179. Saxton MJ. Single-particle tracking: The distribution of diffusion coefficients. *Biophysical Journal* **1997**, 72 (4), 1744–1753. [cited on p. 100]

180. Saxton MJ, Jacobson K. Single-particle tracking: applications to membrane dynamics. *Annual Review of Biophysics and Biomolecular Structure* **1997**, 26, 373–99. [cited on p. 101]

181. Lee GM, Ishihara A, Jacobson KA. Direct observation of brownian-motion of lipids in a membrane. *Proceedings of the National Academy of Sciences of the United States of America* **1991**, 88 (14), 6274–6278. [cited on pp. 105,120]

182. Lee GM, Zhang F, Ishihara A, Mcneil CL, Jacobson KA. Unconfined lateral diffusion and an estimate of pericellular matrix viscosity revealed by measuring the mobility of gold-tagged lipids. *Journal of Cell Biology* **1993**, 120 (1), 25–35. [cited on pp. 105,120]

183. Hong QA, Sheetz MP, Elson EL. Single-particle tracking - analysis of diffusion and flow in 2-dimensional systems. *Biophysical Journal* **1991**, 60 (4), 910–921. [cited on p. 109]

184. Mehier-Humbert S, Guy RH. Physical methods for gene transfer: Improving the kinetics of gene delivery into cells. *Advanced Drug Delivery Reviews* **2005**, 57 (5), 733–753. [cited on p. 112]

185. Klein TM, Wolf ED, Wu R, Sanford JC. High-velocity microprojectiles for delivering nucleic-acids into living cells. *Nature* **1987**, 327 (6117), 70–73. [cited on p. 112]

186. Stevenson D, Agate B, Tsampoula X, Fischer P, Brown CTA, Sibbett W, Riches A, Gunn-Moore F, Dholakia K. Femtosecond optical transfection of cells: viability and efficiency. *Optics Express* **2006**, 14 (16), 7125–7133. [cited on p. 112]

187. McDougall C, Stevenson DJ, Brown CTA, Gunn-Moore F, Dholakia K. Targeted optical injection of gold nanoparticles into single mammalian cells. *Journal of Biophotonics* **2009**, 2 (12), 736–743. [cited on p. 112]

188. Pfeiffer T: Optische Injektion von Goldnanopartikeln in Phospholipid Vesikel **2010**. [cited on p. 118]

189. Stevenson DJ, Gunn-Moore FJ, Campbell P, Dholakia K. Single cell optical transfection. *Journal of the Royal Society Interface* **2010**, 7 (47), 863–871. [cited on p. 121]

Acknowledgments

The last three and a half years have been a wonderful time for me, both scientifically and personally. Many people were involved in this and I would like to thank every one of them for their friendship, help, time, guidance and understanding.

Professor Jochen Feldman, my doctoral thesis supervisor and group leader, I would like to thank for giving me the opportunity to conduct my research here in this group. I have greatly benefited from the support he provided, the highly productive discussions we had and the chances he gave me to present my work and meet other scientists at many different conferences. During my time here, he has helped me to become an independent scientist, giving me the opportunity to realize my own ideas. I am very grateful for the excellent scientific environment I encountered during my time here.

Many thanks to my three advisors for the excellent support I received during their time here. **Professor Thomas Klar** helped me to start my work here, and to understand the basics of conducting scientific research. His Monday meetings were always highly productive and fun. **Professor Fernando Stefani** really showed me how much fun doing science can really be. His enthusiasm for new experiments, his creativity and knowledge of diverse scientific fields all helped me to see science with a completely new perspective. Of course, the many beers we had during discussions helped as well. **Dr. Andrey Lutich** guided me during my last stages of my work here and helped me to hone my skills in microscopy and mathematical calculations. Both Fernando and Andrey helped me considerably during the preparation of this thesis.

Thanks also to **Professor Joachim Rädler**, **Professor Christian Plank** and **Professor Don Lamb** for the opportunity to collaborate on very interesting, interdisciplinary

topics and for providing me with productive suggestions for my experimental studies.

Express thanks go to **Michael Fedoruk**, **Stefan Wimmer** and **Tom Pfeiffer** for the excellent teamwork and great fun we had in the lab together. They have contributed significantly to the thesis.

Christian Mauser deserves special thanks as a great friend (already in Karlsruhe days) and for providing me lodging during my first week in München. Thanks also to all my other room mates **Raphael Tautz**, **Ilka Kriegel**, **Dieter Groß** and **Sergiy Mayilo** as well as our adopted room-mate **Calin Hrelescu** for the pleasant atmosphere and good times we had in the bars around the university after a hard days work.

Thanks also to **Silke Kirchner** for being a really good friend, to **Margaret Horton**, who helped me to get a foothold in biophysics, to **Alexander Ohlinger** for all his help with computer questions and to my fellow members of the computer administrators team. I would further like to thank **Werner Stadler**, **Stefan Niedermaier** and **Christian Holopirek** for their support with technical questions and the designing and realization of many devices and **Anna Helfrich** for her assistance in the chemistry lab. Thanks to all assistants, PhD and Diploma students in the group for providing a very friendly and pleasant atmosphere and for any help they provided me.

Extra special thanks to my girlfriend, **Cordu** for the pleasant times in the chemistry lab, the motivation she provided me during somewhat difficult times, for the corrections of this thesis and for generally being there for me.

Last and most certainly not least I wish to thank my **family** for their endless support. I especially wish to thank my **grandmother** for always believing in me and for her magic crossing fingers and toes. My **parents** deserve the greatest thanks of all, for providing me with the skills and interests to be able to finish my studies and conduct all this work. They spent innumerable hours correcting and suggesting improvements for abstracts, posters, papers and of course this thesis. I love you very much!